2020-11-15

Late quaternary sea-ice and sedimentary redox conditions in the eastern Bering Sea Implications for ventilation of the mid-depth North Pacific and an Atlantic-Pacific seesaw mechanism

Detlef, H

10.1016/j.quascirev.2020.106549
Quaternary Science Reviews
Elsevier BV

Late Quaternary sea-ice and sedimentary redox conditions in the eastern Bering Sea – implications for ventilation of the mid-depth North Pacific and an Atlantic-Pacific seesaw mechanism

Henrieka Detlef[a,b,c*], Sindia M. Sosdian[c], Simon T. Belt[d], Lukas Smik[d], Caroline H. Lear[c], Sev Kender[e], Christof Pearce[a,b], Ian R. Hall[c]

[a]Department of Geoscience, Aarhus University, Høegh-Guldbergs Gade 2, 8000 Aarhus C, Denmark

[b]Arctic Research Centre, Aarhus University, Ny Munkegade 114, 8000 Aarhus C, Denmark

[c]School of Earth and Ocean Sciences Cardiff University, Main Building, Park Place, Cardiff, CF10 3AT, UK

[d]School of Geography, Earth and Environmental Sciences, Plymouth University, Plymouth PL4 8AA, UK

[e]University of Exeter, Camborne School of Mines, Penryn, Cornwall, TR10 9FE, UK

Highlights:

- Extended to seasonal sea ice in the eastern Bering Sea during late MIS 3 and MIS 2
- Millennial sea-ice variability across the deglaciation
- Glacial sea-ice dynamics respond to atmospheric temperature and circulation changes
- During early Heinrich Stadial 1 brine rejection aided to initiate deep convection
- Terrestrial carbon input might have caused OMZ expansion during the early Holocene

*corresponding author: henrieka.detlef@geo.au.dk

Keywords: Late Quaternary, paleoceanography, northern Pacific, marine biomarkers, foraminiferal geochemistry, Bering Sea, NPIW, U/Mn, foraminiferal assemblages

Abstract

On glacial-interglacial and millennial timescales, sea ice is an important player in the circulation and primary productivity of high latitude oceans, affecting regional and global biogeochemical cycling. In the modern North Pacific, brine rejection during sea-ice freezing in the Sea of Okhotsk drives the formation of North Pacific Intermediate Water (NPIW) that ventilates the North Pacific Ocean at 300 m to 1000 m water depth. Glacial intervals of the late Quaternary, however, experienced a deepening of glacial NPIW to at least 2000 m, with the strongest ventilation observed during cold stadial conditions of the last deglaciation. However, the origin of the shifts in NPIW ventilation is poorly understood. Numerical simulations suggest an atmospheric teleconnection between the North Atlantic and the North Pacific, in response to a slowdown or shutdown of the Atlantic meridional overturning circulation. This leads to a build-up of salinity in the North Pacific surface ocean, triggering deep ventilation. Alternatively, increased sea-ice formation in the North Pacific and its marginal seas may have caused strengthened overturning in response to enhanced brine rejection.

Here we use a multi-proxy approach to explore sea-ice dynamics, sedimentary redox chemistry, and benthic ecology at Integrated Ocean Drilling Program Site U1343 in the eastern Bering Sea across the last 40 ka. Our results suggest that brine rejection from enhanced sea-ice formation during early Heinrich Stadial 1 locally weakened the halocline, aiding in the initiation of deep overturning. Additionally, deglacial sea-ice retreat likely contributed to increased primary productivity and expansion of mid-depth hypoxia at Site U1343 during interstadials, confirming a vital role of sea ice in the deglacial North Pacific carbon cycle.

1. Introduction

High latitude oceans play a pivotal role in global biogeochemical cycling. Depending on the mode of oceanic circulation and the efficiency of the biological pump, carbon, oxygen, and nutrients are redistributed in these regions, both within the ocean and between the ocean and the atmosphere (Knox and McElroy, 1984; Levitus et al., 1993; Sarmiento et al., 2004, 1988; Sigman et al., 2010; Toggweiler, 1999; Weber et al., 2016). The formation of deep and intermediate water masses at high latitudes ventilates the ocean’s interior, replenishing its O_2 reservoir (Shcherbina et al., 2003; Talley, 1993; Toggweiler, 1999). Conversely, Ekman suction (Gargett, 1991; Talley and Talley, 1985) and, in the case of the eastern Bering Sea, eddy formation (Ladd, 2014; Mizobata et al., 2002; Mizobata and Saitoh, 2004), cause upwelling of old, low-O_2, high-nutrient, and CO_2-rich deep waters to the surface ocean. Here the exchange of CO_2 between the ocean and the atmosphere hinges on net primary productivity, fueled by the supply of macronutrients from below and dependent on light and micronutrient availability, and the efficiency of the biological pump. On glacial/interglacial (G/IG) and millennial timescales, the dynamics of the ocean circulation and the biological pump are thus fundamental for the distribution of carbon and oxygen in the ocean interior and the atmosphere. In the Bering Sea, the northernmost marginal sea of the Pacific Ocean, sea-ice dynamics strongly influence the regional circulation and primary productivity, modifying the biogeochemical cycling and influencing sedimentary redox conditions.

Large areas of the modern North Pacific surface ocean are characterized as high nutrient low chlorophyll (HNLC) regions with iron representing the limiting micronutrient (Lam and Bishop, 2008; Moore et al., 2001). As such, the North Pacific currently represents a net source of CO_2 to the atmosphere and excess nutrients are re-circulated to lower latitudes (Takahashi et al., 2009, 1997). However, a pronounced spring bloom with high rates of primary productivity is observed along the eastern Bering Sea slope and near the retreating

sea-ice edge (Niebauer et al., 1995; Springer et al., 1996). This is due to nutrient upwelling as well as nutrient release and increased stratification of the water column during spring sea-ice melting (Wang et al., 2014). On longer timescales, sea ice also influences primary productivity by affecting light availability in the surface ocean. While extended sea-ice cover, especially during glacial intervals, may reduce light transmission (Frey et al., 2011; Perovich, 2016), sea-ice melting, on the other hand, leads to stratification in the upper water column, shoaling the mixed layer and increasing light availability (Niebauer et al., 1990; Smith, 1987).

Sea ice is also a critical control of the regional circulation regime of the North Pacific due to brine rejection during sea-ice freezing. At present, no deep water convection takes place in the North Pacific, where excess precipitation and runoff over evaporation result in low surface salinities and a permanent halocline (Emile-Geay et al., 2003; Warren, 1983). Nevertheless, North Pacific Intermediate Water (NPIW) forms in the mixed water region between the Kuroshio and Oyashio Current east of Japan (Talley, 1993). The Oyashio water obtains its characteristic density from Okhotsk Sea Mode Water, which forms via brine rejection during sea ice freezing over the shelves of the Sea of Okhotsk (Shcherbina et al., 2003; Talley, 1993). Characterized as a salinity minimum and an oxygen maximum following the 26.8 σ_θ isopycnal surface (Talley, 1993), NPIW can be traced throughout the North Pacific Ocean between approximately 300 m and 1000 m water depth (Fujii et al., 2013) and can be recognized as far south as 20°N in the eastern subtropical Pacific and even further south in the west (Talley, 1993).

Proxy reconstructions of past oxygenation, nutrient, temperature, and salinity variability of the intermediate and deep North Pacific suggest a deeper and better ventilated intermediate water mass during the Last Glacial Maximum (LGM, 19-26.5 ka) and stadial periods of the last deglaciation (Heinrich Stadial 1 (HS1, 14.7-18 ka) and Younger Dryas (YD, 11.8-12.8

ka)) (Ahagon et al., 2003; Cook et al., 2016; Duplessy et al., 1989; Gong et al., 2019; Jang et al., 2017; Matsumoto et al., 2002; Max et al., 2014; Okazaki et al., 2010, 2012; Rae et al., 2014; Rella et al., 2012; Saenko et al., 2004; Sagawa and Ikehara, 2008). The division between well-ventilated glacial NPIW (GNPIW) and poorly ventilated North Pacific Deep Water (NPDW) has been placed at around 2000 m depth in the North Pacific during the LGM and the early deglaciation (Jaccard and Galbraith, 2013). Studies from the Bering Sea suggest a maximum GNPIW depth of 1000 m to 2000 m during marine isotope stage (MIS) 2 (Cook et al., 2016; Worne et al., 2019), while sediment cores from the Gulf of Alaska indicate potential mixing of well-ventilated waters down to ~3500 m during HS1 (Rae et al., 2014). A vertically expanded intermediate water mass during glacial intervals has the potential to fundamentally alter the North Pacific carbon cycle by reducing the amount of NPDW that is mixed to the surface, thus preventing the release of deeply sequestered carbon (Gong et al., 2019; Gray et al., 2018; Kender et al., 2018; Max et al., 2014). Breakdown of enhanced GNPIW formation and shoaling of NPDW across the last deglaciation, on the other hand, would have increased the upwelling of carbon and nutrients into the photic zone (Gray et al., 2018). The enhanced supply of macronutrients due to shoaling of NPDW likely contributed to peaks in primary productivity observed during warm interstadial periods across the last deglaciation, such as the Bølling-Allerød (BA, 12.8-14.7 ka) and the earliest Holocene, coinciding with widespread mid-depth hypoxia in the North Pacific as seen from laminated sediments (Aiello and Ravelo, 2012; Cook et al., 2005; Expedition 323 Scientists, 2010; Kuehn et al., 2014; Ohkushi et al., 2013; Praetorius et al., 2015; Schlung et al., 2013; Zheng et al., 2000).

The LGM and stadial periods of the last deglaciation were marked by a reduced Atlantic meridional overturning circulation (AMOC), while the BA and early Holocene likely experienced a strengthened AMOC (McManus et al., 2004), suggesting an Atlantic-Pacific

overturning seesaw. The dynamics of the seesaw and specifically the trigger mechanism for deep convection in the North Pacific, however, remain equivocal. Numerical simulations suggest an atmospheric teleconnection between the North Atlantic and the North Pacific via lower latitudes, affecting the oceanic and atmospheric circulation in the Pacific and leading to a salinity build up in the North Pacific, driving enhanced regional overturning (Chikamoto et al., 2012; Gong et al., 2019; Menviel et al., 2012; Okazaki et al., 2010; Okumura et al., 2009; Wu et al., 2008). Proxy reconstructions, on the other hand, indicate a pivotal role of brine rejection from increased sea-ice formation in the Bering Sea and/or the Sea of Okhotsk, as a mechanism driving enhanced GNPIW ventilation (Cook et al., 2016; Horikawa et al., 2010; Knudson and Ravelo, 2015; Max et al., 2014; Rella et al., 2012). Alternatively, some combination of both the sea ice and atmospheric teleconnection mechanisms might drive the suggested overturning seesaw (Gong et al., 2019).

Although there are only a few LGM sea-ice reconstructions in the Bering Sea, previous investigations demonstrate that sea-ice extent in the Bering Sea responds sensitively to climate change on millennial and G/IG timescales (Caissie et al., 2010; Itaki et al., 2012; Méheust et al., 2016, 2018), in line with a potential role of sea ice for GNPIW formation. As of yet, however, no studies have co-investigated the sea-ice history of the Bering Sea in combination with local changes in the biogeochemical cycling, to decipher the mechanisms driving sea-ice variability, the potential of sea ice to trigger enhanced overturning, and its role in the deglacial North Pacific carbon cycle.

This study, thus, uses a multi-proxy approach to simultaneously investigate past changes in eastern Bering Sea sea-ice cover and changes in the biogeochemical cycling at Integrated Ocean Drilling Program (IODP) Site U1343 (57°33.4′N, 176°49.0′W; 1953 m) (Figure 1) (Expedition 323 Scientists, 2010) across the last ~40 ka. Sea-ice reconstructions are based on source-specific biomarkers, while past changes in sedimentary redox chemistry are inferred

from authigenic foraminiferal U/Ca and U/Mn, in combination with the benthic foraminiferal assemblage. This provides a more complete picture of the late Quaternary sea-ice evolution in the North Pacific and its role for GNPIW formation and primary productivity.

2. Regional oceanography

The modern Bering Sea is characterized by a subarctic water column structure. Above the permanent halocline (100-200 m) a warm surface layer (0-50 m) forms during summer underlain by a cold dichothermal layer (50-200 m), a remnant of winter mixing (Miura et al., 2002; Tanaka and Takahashi, 2005). Cooling and deepening of the thermocline during winter promotes the formation of a winter mixed layer, restricted by the halocline depth (Miura et al., 2002; Tanaka and Takahashi, 2005). While only little is known about the water masses in the mid-depth Bering Sea today, the deep Bering Sea is characterized by NPDW (Coachman et al., 1999; Stabeno et al., 1999), entering through Kamchatka Strait at depth below 2500 m (Coachman et al., 1999; Stabeno et al., 1999) and modified by small amounts of deep water that are formed in situ in the Bering Sea today (Warner and Roden, 1995).

The surface circulation in the Bering Sea forms a cyclonic gyre, fed by the inflow of relatively warm and nutrient-rich Alaskan Stream waters through several passes in the Aleutian Arc (Stabeno et al., 1999) (Figure 1). Within the Bering Sea, the cyclonic gyre is composed of the eastward flowing Aleutian North Slope Current (ANSC), the Bering Slope Current (BSC), and the southward flowing East Kamchatka Current (EKC). Main surface outflow occurs through Kamchatka Strait, while some surface water (0.85 Sverdrup) (Coachman, 1993) flows northward on the eastern Bering Sea shelf and into the Arctic Ocean through the 50 m deep Bering Strait. Along the eastern Bering Sea slope, mesoscale eddies form within the BSC, causing upwelling of nutrient-rich deep waters (Ladd et al., 2012; Mizobata et al., 2008, 2002; Mizobata and Saitoh, 2004). Together with the mixing of shelf

and basin waters (Hurst et al., 2010; Springer et al., 1996; Tanaka et al., 2012) and nutrient release during spring sea-ice melting (Wang et al., 2014), this fuels one of the most productive ecosystems in the world’s ocean, often termed the ‘Green Belt’ (Springer et al., 1996). High rates of primary productivity (175-275 g C m^{-2} yr^{-1}, (Springer et al., 1996)) and demineralization of sinking organic matter lead to depleted oxygen concentrations in mid-depth waters, forming a pronounced oxygen minimum zone (OMZ) between 600-1000 m (Figure 1) (Expedition 323 Scientists, 2010; Whitledge and Luchin, 1999). Within the core of the OMZ, oxygen concentrations range from 0.43-1.57 mg L^{-1} (0.3-1.1 ml L^{-1}) (Whitledge and Luchin, 1999). Beyond the Green Belt, the Bering Sea is largely characterized as a HNLC region, with iron representing the limiting micronutrient (Aguilar-Islas et al., 2007; Leblanc et al., 2005; Springer et al., 1996). However, a pronounced spring phytoplankton bloom can be observed on the eastern shelf, tightly coupled to the northward retreat of sea ice from March/April onwards (Brown and Arrigo, 2013; Niebauer et al., 1995).

Seasonal sea ice in the eastern Bering Sea originates in the Chukchi Sea and in polynyas on the southward facing coastlines (Niebauer et al., 1999), with an average winter sea ice and brine formation in Bering Sea polynyas of 10-12 cm day^{-1} and 0.006-0.042 Sv, respectively (Niebauer et al., 1999). Based on observational data and modelling studies, Cavalieri and Martin (1994) concluded that brines formed on the eastern Bering shelf flow northward across the shelf and into the Arctic Ocean. The maximum extent of sea ice in the eastern Bering Sea is closely coupled to atmospheric and oceanic temperatures together with the predominant direction of winter storm tracks (Rodionov et al., 2007). Typically, the maximum sea-ice extent is reached near the eastern Bering Sea slope during March/April (Figure 1). Recent years, however, have seen a pronounced retreat of the winter sea-ice edge with important implications for the marine ecosystem (Brown et al., 2011; Brown and Arrigo, 2013; Grebmeier et al., 2006).

3. Materials and methods

3.1 IODP Site U1343

IODP Site U1343 (57°33.4′N, 176°49.0′W, water depth 1953 m) (Figure 1) was recovered from a topographic high off the eastern Bering Sea slope. In total, five holes were cored (A-E) and a composite depth scale was constructed between 0-270 m core composite depth using cores from holes A, C, and E (Expedition 323 Scientists, 2010). Under modern conditions, the core site is bathed in NPDW, characterized by local bottom water temperatures of 1.9°C, salinities of 34.6, and [O_2] of 1.2 ml L^{-1} (Garcia et al., 2014; Locarnini et al., 2013; Zweng et al., 2013).

The age model is based on benthic foraminifera oxygen isotope ($\delta^{18}O_b$) stratigraphy (Asahi et al., 2016; Kender et al., 2018; Worne et al., 2019) and correlation to the LR04 stack (Lisiecki and Raymo, 2005). As the $\delta^{18}O_b$ record at Site U1343 is of relatively low resolution and correlation to the LR04 stack has been performed over multiple G/IG cycles, uncertainty in the chronology, especially when interpreting millennial-scale climate events, needs to be considered. Across the last deglaciation a prominent reduction in mid-depth oxygen concentrations in the North Pacific, related to increased productivity during interstadial conditions, led to the expansion of the mid-depth OMZ in the Bering Sea and preservation of laminated sediments, formed under anoxic conditions between ~800 m and 2100 m (Caissie et al., 2010; Cook et al., 2005; Expedition 323 Scientists, 2010; Gersonde, 2012; Kuehn et al., 2014; Max et al., 2012; Schlung et al., 2013). Previous studies on the north-eastern Bering Sea slope (SO202-18-3/6, HLY02-02-3JPC (Figure 1)) at ~1000 m water depth have dated the base of laminated sediment section to 14.4-14.6 ka and ~11.7 ka, corresponding to the onset of the BA and the early Holocene, respectively (Cook et al., 2005; Kuehn et al., 2014). At Site U1343 the base of the laminated intervals are found at 1.07 m CCSF-A and 2.69 m

CCSF-A (Supplementary Figure 1) (Expedition 323 Scientists, 2010). Using the $\delta^{18}O_b$ stratigraphy for Site U1343 recently updated by Worne et al. (2019) this yields ages of 10.5 ka and 16.3 ka for the base of the laminations, respectively. Considering that the present day core of the OMZ lies at 800 m water depth (Expedition 323 Scientists, 2010; Whitledge and Luchin, 1999), it seems unlikely that the onset of the laminations at 2000 m water depth would predate those occurring at ~1000 m by ~2 kyr. Using the original $\delta^{18}O_b$ stratigraphy by Asahi et al. (2016), the base of the laminated intervals at Site U1343 are dated to 10.5 ka and 14.7 ka, suggesting that this age model provides a better fit for the LGM-Holocene transition. Thus, we use those age-depth tie points as the base for our chronology (Supplementary Figure 2) (Table 1). Further, we added the bases of the laminations at 1.07 and 2.69 m CCSF-A as additional age-depth tie points using ages of 11.7 ka and 14.5 ka, respectively, based on previous studies from the north-eastern Bering Sea slope (Cook et al., 2005; Kuehn et al., 2014) (Supplementary Figure 2). This approach assumes vertically synchronous expansion of the OMZ between 1000 m and 2000 m at the onset of the BA and the early Holocene. The expansion of the OMZ was most likely caused by the high rates of primary productivity during interstadial phases and subsequent demineralization of organic matter in the water column (Kuehn et al., 2014). This suggests that anoxic conditions associated with the OMZ expansion might have occurred somewhat earlier at the shallower sites. Considering the average sample resolution of our highest resolved dataset (0.5 kyr temporal spacing), however, we assume this temporal discrepancy to be negligible. Further, by applying this chronology, the mass accumulation rate of opal (MAR_{opal}) (Kim et al., 2014) peaks at ~13.5 ka at Site U1343 (Supplementary Figure 2) within the BA interval, consistent with similar productivity peaks between ~13 ka and 14.5 ka from numerous other sites in the subarctic North Pacific (Addison et al., 2012; Brunelle et al., 2007, 2010; Caissie et al., 2010; Cook et

al., 2005; Gebhardt et al., 2008; Jaccard et al., 2009; Kuehn et al., 2014; Ren et al., 2015; Schlung et al., 2013).

Our chronology thus allows us to identify general millennial-scale trends at Site U1343 across the last deglaciation, while short-term events (e.g. the YD) and the exact timing of stadial/interstadial boundaries should be considered with more caution.

3.2 Sea-ice biomarker analyses

3.2.1 Methodology

Reconstructions of past sea-ice extent are based primarily on selected source-specific highly branched isoprenoid (HBI) biomarkers. IP_{25} (Ice Proxy with 25 carbon atoms) is a mono-unsaturated HBI produced by certain Arctic diatoms living in brine channels at the bottom surface of seasonal sea ice (Belt, 2018; Belt et al., 2007; Brown et al., 2014). Thus, its sedimentary presence provides binary evidence of past seasonal sea ice (Belt, 2018). To complement IP_{25} data, we co-measured a tri-unsaturated HBI (HBI III), produced by diatoms characteristic of the spring sea-ice edge bloom within the open waters of the marginal ice zone (MIZ) (Belt et al., 2017, 2015; Smik et al., 2016), and used the MAR_{opal} (Kim et al., 2014), as an indicator of primary productivity. We also measured a di-unsaturated HBI (HBI II), which typically co-varies with IP_{25} in the Arctic (Belt et al., 2007; Brown et al., 2014; Vare et al., 2009), and a range of sterol biomarkers. Sterols are common lipids in cell membranes of eukaryotic organisms, occurring in a range of marine primary producers and in higher plants, which can complicate their use as environmental tracers (Belt and Müller, 2013; Volkman, 1986). Nonetheless, diatoms are a common source of brassicasterol and dinosterol in the marine realm (Volkman, 1986; Volkman et al., 1998; Volkmanm, 2006) and they are routinely applied as indicators of open water productivity (e.g. Berben et al., 2017; Méheust et al., 2013; Müller et al., 2009; Navarro-Rodriguez et al., 2013). Other sterols, such

as campesterol and β-sitosterol, on the other hand, are more common in higher plants and are often considered to reflect terrestrial organic matter (Volkman, 1986; Volkmanm, 2006).

3.2.2 Lipid extraction and analysis

Biomarkers were extracted from ~3 g of freeze-dried homogenized sediments. The samples were freeze dried (-45°C; 0.2 mbar; 48 h) using an Edwards K4 Modulyo freeze drier and a Christ Alpha 1-4 LSC freeze drier at Cardiff and Aarhus University, respectively. Dried samples were homogenized using an agate pestle and mortar. 9-octylheptadec-8-ene (9-OHD) and 5α-androstan-3βol (0.1 µg each) were used as internal standards for HBI and sterol quantification, respectively. Lipid biomarkers were extracted using two different extraction techniques. A relatively small number of samples (n = 15) were extracted using Dichloromethane (DCM):Methanol (2:1, v/v) as outlined in Belt et al. (2012). Elemental Sulphur was removed from extracts using tetrabutylammonium sulphite (Cabedo-Sanz and Belt, 2015) and lipid classes were separated using silica column chromatography. Apolar lipids (e.g. HBIs) were eluted with hexane, while more polar lipids, including sterols, were eluted using hexane/methyl acetate (1:4; v/v). All other samples (n = 28) were extracted by a saponification-based method (5% Potassium hydroxide (KOH) solution in Methanol:H_2O (9:1, v/v); 70°C; 1 h). After cooling to room temperature, the non-saponifiable lipids were extracted (hexane; 3 x 2 mL), transferred into glass vials, and dried (N_2; 25°C). HBI fractions were further purified using silver-ion chromatography (5:95 $AgNO_3$:SiO_2). Saturated hydrocarbons were eluted with hexane (1 mL) and HBI fractions then eluted with acetone (2 mL). Sterol fractions were derivatised using N,O- Bis(trimethylsilyl)trifluoroacetamide (50 µL, 70 °C, 1 h) and diluted with 0.5 mL DCM immediately prior to analysis by gas chromatography-mass spectrometry (GC-MS). To check for consistency between the two extraction procedures, five samples (between ~8 ka and ~24 ka) were extracted using both methods and the HBI fractions purified using silver-ion chromatography. The IP_{25} and HBI

III concentrations were comparable between the two methods with an average relative standard deviation (r.s.d.) of 11% and 16% and a significant correlation between the two methods for both IP_{25} (R^2 = 0.99 [0.98; 1], n = 5) and HBI III (R^2 = 0.99 [0.99; 1], n = 5) (Supplementary Figure 3 and 4). As such, we consider the HBI data from both methods to be mutually consistent. In contrast, brassicasterol concentrations were significantly lower with the DCM:Methanol extraction method, likely due to a (variable) percentage of the total extracted sterols remaining in a bound format and thus not readily derivatised using BSTFA. As such, we only report brassicasterol concentrations for samples obtained using the KOH extraction method.

All biomarker samples were analyzed at Plymouth University using an Agilent 7890A GC coupled to a 5975 series mass selective detector fitted with an Agilent HP-5ms column. The operating conditions are specified in Belt et al. (2012). The identification of individual lipids was based on their characteristic retention indices and mass spectra (Belt, 2018), while quantification was achieved through comparison of the integrated peak area (PA) of the selected ions (*m*/*z* 350 (IP_{25}); 348 (HBI II); 346 (HBI III); 470 (brassicasterol); 458 (cholesterol); 382 (campesterol); 396 (β-sitosterol)) with the PA of the respective internal standards (Belt et al., 2012), together with individual instrumental response factors and the mass of sediment extracted (Belt et al., 2012).

Semi-quantitative measures of sea-ice extent were determined via the so-called PIP_{25} index (Müller et al., 2011) and classification tree (CT) methods (Köseoğlu et al., 2018b, 2018a). The latter is based on distributions of a suite of HBIs in surface sediments from the Barents Sea, which has a similar modern sea-ice cycle to the Bering Sea (Köseoğlu et al., 2018a, 2018b). CT analysis categorizes sea-ice conditions into marginal (0-10%), intermediate (10-50%), and extensive (>50%) spring sea-ice concentration. PIP_{25} indices (Equation 1) were calculated for both HBI III ($P_{III}IP_{25}$) (Smik et al., 2016) and brassicasterol (P_BIP_{25}) (Müller et

al., 2011) as counterparts to IP_{25}, with the c-factor (Equation 2) based on the average biomarker concentrations in the analyzed interval.

$$PIP_{25} = \frac{[IP_{25}]}{([IP_{25}]+([phytoplankton\ marker]*c))} \quad (1)$$

$$c = \frac{mean\ [IP_{25}]}{mean\ [phytoplankton\ marker]} \quad (2)$$

3.3 Geochemical and taxonomic foraminiferal analyses

In total, 27 samples (10 cc) between ~8 ka and ~42 ka with an average resolution of ~1.4 ka were processed for foraminiferal geochemistry and taxonomy. The samples were washed over a 63 µm sieve and dried over night at 30°C. Benthic and planktonic foraminifera were counted and picked from the 150-250 µm size fraction.

3.3.1 Authigenic foraminiferal U/Ca and U/Mn

The authigenic U/Ca (aU/Ca) and U/Mn (aU/Mn) of planktonic and benthic foraminifera are sensitive to sedimentary redox conditions, via post-depositional diagenetic processes, and have recently been proposed as proxies for sedimentary redox chemistry (Boiteau et al., 2012; Chen et al., 2017; Gottschalk et al., 2016). At Site U1343 scanning electron microscope images and geochemical analyses of discolored foraminiferal specimens clearly demonstrate authigenic carbonate formation, related to organoclastic sulphate reduction (> 8 meters below seafloor (mbsf)) and anaerobic oxidation of methane (~8 mbsf) (Detlef et al., 2020). Compared to primary foraminiferal carbonate, foraminifera-bound authigenic carbonates are enriched in both U and Mn (Detlef et al., 2020), suggesting that U/Ca and U/Mn may be valuable proxies to determine past changes in sedimentary redox chemistry at Site U1343. In the modern ocean uranium behaves conservatively in seawater but is removed from pore waters as U^{4+} under anoxic conditions (Boiteau et al., 2012). Both planktonic and benthic foraminiferal tests act as a low uranium substrate (3-23 nmol/mol) (Boiteau et al.,

2012; Chen et al., 2017; Raitzsch et al., 2011; Russell et al., 2004) and can accumulate authigenic uranium. As the ionic radius of U^{4+} is similar to that of Ca^{2+}, U^{4+} can be readily incorporated into authigenic carbonates forming in the sediment during early diagenesis (Sturchio et al., 1998; Zhao et al., 2016). Sedimentation rates of 34 ± 11 cm ka^{-1} (Asahi et al., 2016) at Site U1343 suggest that authigenic U accumulation is unlikely to be affected by re-oxidation processes. Manganese, on the other hand, precipitates as Mn^{4+} in sediments under oxic conditions in the form of Mn-oxides or Mn-carbonates and is re-dissolved into pore waters as Mn^{2+} under reducing conditions (Froelich et al., 1979). The dissolved Mn^{2+} either migrates upwards until it reaches the depth of oxygen penetration where it re-precipitates or is removed from pore waters by the formation of diagenetic carbonates (Froelich et al., 1979; Pedersen and Price, 1982). Thus, Gottschalk et al. (2016) proposed to normalize authigenic foraminiferal uranium to manganese (U/Mn) rather than calcium (U/Ca), to avoid species-specific differences resulting from changes in the surface-to-mass ratio. Recently, however, Skinner et al. (2019) showed that U and Mn might be incorporated into foraminiferal authigenic coatings in different ways and caution should be taken when interpreting aU/Mn alone.

As the abundance of different benthic foraminiferal species varies across the analyzed time interval, the record of authigenic trace metals is based on multiple species. Authigenic foraminiferal trace metals were analyzed for the benthic foraminiferal species *Islandiella norcrossi* (n = 7) and *Uvigerina* spp. (n = 3), and the planktonic foraminiferal species *Neogloboquadrina pachyderma* (n = 6), for all samples with sufficient specimens (>80 µg). We were unable to determine planktonic aU/Mn ratios, as *N. pachyderma* samples were too small to yield reliable Mn/Ca results (signal-to-noise-ratio < 5). Previous studies suggest that foraminiferal aU/Ca may be susceptible to changes in the surface-to-mass-ratio of foraminiferal tests, indicating that aU/Ca is likely species-specific and sensitive to the

foraminiferal test size (Gottschalk et al., 2016). To circumvent the effect of test size on authigenic mineral precipitation, both planktonic and benthic foraminifera were picked from a narrow size fraction (150-250 µm). Planktonic aU/Ca was measured exclusively on *N. pachyderma*, avoiding any effects of species-specific surface-to-mass ratio on aU/Ca.

Analyses of authigenic foraminiferal trace metals typically only require weak chemical cleaning (Gottschalk et al., 2016) to preserve the authigenic geochemical signal. Benthic foraminiferal samples at Site U1343, however, were also analyzed for primary foraminiferal trace metal ratios, such as Mg/Ca, a faithful proxy of bottom water temperatures (e.g. Lea et al., 1999; Nürnberg et al., 1996; Rosenthal et al., 1997). Thus, benthic foraminiferal samples were cleaned according to the Cd-cleaning protocol (Boyle, 1983; Boyle and Keigwin, 1985), consisting of: (i) A clay removal step with repeated rinses in UHQ water and methanol with intervals of ultrasonication, to remove adhered clay particles. (ii) A reductive step in a hot solution of 1200 µl hydrous hydrazine in a citric acid (10 mL)/ammonia (10 mL) buffer for 30 minutes, including several intervals of short (~5 seconds) ultrasonication followed by extensive rinsing with UHQ water and a sample transfer to fresh acid-cleaned micro-centrifuge tubes, targeting the removal of oxide coatings. (iii) An oxidative step in a hot solution of alkali (0.1 M NaOH) buffered 1% H_2O_2 to remove remnant organic material. (iiii) A dilute acid leach in 0.001 M HNO_3 to remove remaining contaminants adsorbed to the surface of the foraminifera fragments. Planktonic foraminifera, on the other hand, were cleaned according to the Mg-cleaning protocol (Barker et al., 2003), which omits the reductive step compared to the Cd-cleaning protocol. As, Cd-cleaning is more effective in the removal of authigenic mineral phases compared to Mg-cleaning (Hasenfratz et al., 2017; Pena et al., 2005), Cd-cleaned benthic foraminiferal trace metal ratios can be compared to Mg-cleaned planktonic foraminiferal trace metal ratios to ensure a signal of authigenic origin.

Following the chemical cleaning, foraminiferal samples were dissolved in 120 µL 0.065M HNO_3. All samples were analyzed using a Thermo Element XR High Resolution Inductively Coupled Plasma Mass Spectrometer (ICP-MS) at Cardiff University. Trace metal ratios were quantified using matrix-matched standards and two consistency standards were run at the beginning and end of every sequence. The two consistency standards have U/Ca concentrations of 4.49 nmol/mol and 27.21 nmol/mol, respectively and U/Mn concentrations of 0.16 mmol/mol and 0.14 mmol/mol, respectively. The long-term reproducibility between 2015 and 2018 (n = 25) was ±3.03% (relative standard deviation, r.s.d.), ±2.63% (r.s.d.), ±3.11% (r.s.d.), and ±2.26% (r.s.d.) for U/Ca and U/Mn, respectively.

3.3.2 Benthic foraminiferal assemblages

Benthic foraminiferal assemblages in the mid-depth Bering Sea is dominated by calcareous infaunal species, controlled primarily by the supply of organic matter to the sediments (Kender et al., 2019; Kender and Kaminski, 2017; Okazaki et al., 2005; Setoyama and Kaminski, 2015). The dominant species are typically tolerant of high-productivity-low-oxygen conditions, related to the pronounced mid-depth OMZ and export of organic carbon to the sediments, particularly within the Green Belt along the eastern Bering Sea slope (Expedition 323 Scientists, 2010; Kender et al., 2019; Khusid et al., 2006; Setoyama and Kaminski, 2015).

Typically, foraminiferal census counts rely on a representative subset of the sample with >300 specimens. However, at Site U1343 the foraminiferal abundance is generally low (Expedition 323 Scientists, 2010) with 0-309 specimens in the 150-250 µm fraction per sample for the studied interval. We consider all samples with >50 specimens for environmental inferences, which has previously been shown to yield reliable diversity at the Bowers Ridge in the southern Bering Sea (Kender et al., 2019).

In addition to the relative abundance of species with strong environmental preferences (e.g. *Bulimina exilis*), we use correspondence analysis (CA) to gain insights into the overall changes in benthic foraminiferal assemblages at Site U1343. CA (using the software PAST (Hammer et al., 2001)) was performed on all samples with >50 specimens. Species that only occurred in very low numbers (<10 specimens for the entire dataset) were grouped and excluded from the CA. CA uses reciprocal averaging to compare the species within a given dataset (Greenacre, 1983), with CA scores characterizing similar faunal traits (e.g. Hammer and Harper, 2006; Kender et al., 2019). The CA axes describe the variance in the dataset, corresponding to the ecological parameter predominantly controlling the abundance of species within the assemblage.

3.4 Statistical analyses

Correlation analyses of time-series data ($n > 10$) was performed in PearsonT3 (Mudelsee, 2003), which automatically performs mean detrending and estimates the persistence time of both variables. The reported confidence intervals (CI) for these correlations are students t CIs based on nonparametric bootstrapping (Mudelsee, 2003). For all time-series data with $n < 10$ and non-time-series data, correlation analyses were performed in R Studio (R Studio Team, 2015) with a 95% significance level. We further calculated a 10-pt moving window correlation for IP_{25} and HBI III, as well as IP_{25} from Site U1343 and IP_{25} from SO202-27-6, in R Studio (R Studio Team, 2015) with CIs based on Monte Carlo simulations ($n = 10{,}000$) of random variables with the same amount of observations and window width as for the data set.

4. Results

4.1 Sea ice related biomarkers

4.1.2 HBI biomarker concentrations in sediments from MIS 3 to MIS 1 at IODP Site U1343

HBIs were measured on 43 samples with an average temporal resolution of 0.5 ka between 7.8 ka and 25 ka and 2.5 ka between 25 ka and 42.5 ka. IP_{25} concentrations vary from 0-6.2 ng/g sed with the highest concentrations occurring during early MIS 2 at ~25 ka (Figure 2). In general, IP_{25} is relatively high during MIS 3 and MIS 2 (mean concentration = 3.2 ng/g sed.) and much lower during early MIS 1 (mean concentration = 0.2 ng/g sed.) (Figure 2). HBI II varies between 0 ng/g sed and 29.9 ng/g sed. It follows the IP_{25} trend with a significant correlation between the two biomarkers (R^2 = 0.90 [0.49; 0.98], n = 43), as expected given their co-production (Brown et al., 2014). Since HBI II concentrations are higher than those for IP_{25}, its detection in some samples where IP_{25} could not be quantified (BA and early Holocene) suggests that the latter was likely present, but below the limit of detection and thus in very low concentration.

HBI III concentrations vary between 0.4 ng/g sed and 43.5 ng/g sed. and are generally low during MIS 3 and MIS 2 (<3.2 ng/g sed) with local maxima around 16 ka and 21 ka (Figure 2). MIS 1 is characterized by an increase in HBI III concentrations at the BA/YD transition up to ~4.5 ng/g sed., followed by a sharp decrease. Starting at ~11 ka HBI III concentrations increase to values of up to 43.5 ng/g sed., an order of magnitude higher than values during MIS 3 and MIS 2 (Figure 2). HBI III and IP_{25} show a weak negative correlation (R^2 = -0.35 [-0.58; -0.06], n = 43) for the entire dataset, which is likely influenced by the extreme increase of HBI III during the early Holocene. We thus calculated a 10-pt moving window correlation with 95% and 99% confidence intervals based on Monte Carlo simulations (n = 10,000) of random variables with 43 data points and a window width of 10. The running correlation reveals no significant correlation of IP_{25} and HBI III throughout the analyzed interval

(Supplementary Figure 5), consistent with a pronounced seasonal sea-ice cycle in the eastern Bering Sea from late MIS 3 to the early Holocene (Detlef et al., 2018).

All HBIs exhibit millennial-scale variability across the last deglaciation (Figure 2). HS1 is marked by an increase in IP_{25}, HBI II, and HBI III. Both IP_{25} and HBI II demonstrate an early (~17.5 ka) and mid-HS1 peak (~16 ka). HBI III, on the other hand, is characterized by one broad peak during mid-HS1 (~15.3-16.4 ka) (Figure 2), which coincides with the second peak in IP_{25} and HBI II. Late HS1 (<15.3 ka) sees a rapid decrease in the concentrations of all three HBIs towards the BA. IP_{25} and HBI II are low throughout the BA, with IP_{25} below the level of detection. During the YD, both biomarkers increase again, although with lower concentrations compared to the early deglaciation (Figure 2). HBI III is low during the early BA and increases again towards the end, peaking around the BA/YD transition followed by another decrease (Figure 2). The early Holocene is marked by a sharp increase in HBI III yet low IP_{25} and HBI II concentrations (Figure 2).

4.1.3 Sterol biomarker concentrations in sediments from MIS 3 to MIS 1 at IODP Site U1343

We analyzed 28 samples from 7.8 ka to 25 ka with an average temporal resolution of 0.63 ka for their brassicasterol, campesterol, cholesterol, and β-sitosterol content. Sterol concentrations vary between 3.1-23.6 µg/g sed., 2.0-12.3 µg/g sed., 3.2-18.0 µg/g sed., and 3.8-19.8 µg/g sed. for brassicasterol, campesterol, cholesterol, and β-sitosterol, respectively (Figure 2). The temporal trend in sterol biomarker concentrations is relatively uniform with small differences between sterols classified as being predominantly marine (brassicasterol and cholesterol) and predominantly terrestrial (campesterol and β-sitosterol). In general, sterol concentrations are low during the LGM, followed by an increase during HS1. The increase in campesterol and β-sitosterol across HS1 is more continuous compared to

brassicasterol and cholesterol, suggesting a two-stepped increase (Figure 2). Maximum sterol concentrations occur during the early BA, followed by a decrease into the early Holocene (Figure 2). Across the YD, sterol concentrations were only measured for one sample, thus we cannot draw reliable conclusions for this period. Across the early Holocene, brassicasterol and cholesterol are consistently low, while campesterol and β-sitosterol have a local maximum at the onset of the Holocene (Figure 2).

4.1.4 Semi-quantitative sea-ice reconstructions based on the PIP_{25} index and classification tree analysis

$P_{III}IP_{25}$ and P_BIP_{25} vary from 0-0.65 and 0-0.61, respectively, indicating reduced/ice free to seasonal sea-ice conditions in the eastern Bering Sea across the last ~45 ka. $P_{III}IP_{25}$ is high throughout most of MIS 3 and MIS 2 (~0.3-0.7) with a decrease observed during late HS1 (Figure 3). This is followed by low values during MIS 1 with the exception of two data points in the YD (Figure 3). There are no P_BIP_{25} data beyond 25 ka (see section 4.1.3), but P_BIP_{25} is generally high during MIS 2 (~0.4-0.6) with a decrease during late HS1 and overall low values throughout MIS 1 apart from one data point that falls into the YD interval (Figure 3). Although P_BIP_{25} and $P_{III}IP_{25}$ are highly correlated (R^2 = 0.94 [0.88; 0.97], n = 28), some differences in the peak values occur during the YD, late HS1, and around 25 ka (Figure 3).

According to the CT approach (Köseoğlu et al., 2018b, 2018a), sea-ice conditions in the eastern Bering Sea were generally extensive (i.e. >50% spring sea-ice concentration) during MIS 3 and early MIS 2 (Figure 3). Intermediate sea-ice conditions (i.e. 10-50%) characterized the mid to late MIS 2 with a sporadic return to extensive sea-ice extent during early HS1 and a decrease to marginal ice conditions (i.e. <10%) at the HS1/BA transition (Figure 3). Early MIS 1 is also characterized by marginal sea-ice conditions with two peaks

of intermediate sea-ice concentrations during the YD (Figure 3). Thus, the overall trend of the two PIP_{25} indices and CT results compare well, especially across the deglaciation (Figure 3).

4.2 Authigenic foraminiferal geochemistry

4.2.1 Authigenic benthic and planktonic foraminiferal U/Ca

Foraminiferal aU/Ca ratios at Site U1343 were determined on 6 *N. pachyderma*, 3 *Uvigerina* spp., and 7 *I. norcrossi* samples between 10.0 ka and 27.2 ka (Figure 4). Planktonic aU/Ca are consistently higher compared to benthic aU/Ca, with an offset of 6.1-12.0 nmol/mol (Figure 4), as a result of more effective removal of authigenic mineral phases during Cd-cleaning.

Planktonic foraminiferal aU/Ca ranges from 10.6-48.8 nmol/mol with highest values during the early Holocene (Figure 4). Benthic foraminiferal aU/Ca varies between 4.4 nmol/mol and 18.2 nmol/mol. Although foraminiferal U/Ca ratios are low and predominantly within the range expected for primary foraminiferal calcite (<23 nmol/mol (Boiteau et al., 2012; Chen et al., 2017; Raitzsch et al., 2011; Russell et al., 2004)), we argue for an authigenic origin. Previous studies propose that primary foraminiferal U/Ca responds to changes in $\Delta[CO_3^{2-}]$ (Keul et al., 2013; Raitzsch et al., 2011), although recent core-top results by Chen et al. (2017) did not find a significant correlation between benthic foraminiferal U/Ca and carbonate system parameters. Parallel benthic and planktonic aU/Ca ratios, available for 4 samples at Site U1343, show a significant positive correlation (R^2 = 0.98 [0.28;1], n = 4). This, together with previous results on the presence of high U and Mn authigenic carbonates at Site U1343 (Detlef et al., 2020), strongly suggests that the aU/Ca signal was acquired post-depositional when co-deposited benthic and planktonic foraminifera tests were exposed to the same sedimentary redox conditions.

The benthic foraminiferal assemblage is characterized by a faunal change associated with the deglaciation. MIS 2 benthic aU/Ca was measured on *I. norcrossi* (4.4-18.2 nmol/mol), while benthic aU/Ca across MIS 1 was measured exclusively on *Uvigerina* spp. (7.1-10.0 nmol/mol) (Figure 4). This suggests, that the benthic aU/Ca change associated with the transition from *I. norcrossi* to *Uvigerina* spp. could reflect changes in the species-specific accumulation of authigenic mineral phases (due to differences in the surface-to-mass ratio and/or shell morphology) rather than sedimentary redox changes. Nonetheless, intra-species benthic aU/Ca changes across MIS 2 and MIS 1, respectively, can be interpreted as reflecting relative changes in the sedimentary redox chemistry at Site U1343.

There are two episodes of decreased *I. norcrossi* aU/Ca at ~24.7 ka and ~17.4 ka suggesting changes in the sedimentary redox chemistry across MIS 2 (Figure 4). While there is no planktonic aU/Ca data available around 24.7 ka, a contemporaneous decrease in planktonic aU/Ca is observed at ~17.4 ka (Figure 4), substantiating the proposed sedimentary redox changes based on benthic aU/Ca. Across the deglaciation benthic aU/Ca remains relatively constant, however this is associated with the faunal change from *I. norcrossi* to *Uvigerina* spp. Planktonic aU/Ca, on the other hand, demonstrates an increase associated with the deglaciation, suggesting more reducing conditions (Figure 4), in line with the preservation of laminated sediments at Site U1343.

4.2.2 Authigenic benthic foraminiferal U/Mn

Benthic aU/Mn varies between 0.1-0.2 mmol/mol and 0.5-1.2 mmol/mol for *Uvigerina* spp. and *I. norcrossi*, respectively (Figure 4). Across MIS 2 benthic aU/Mn, based on *I. norcrossi*, shows two episodes of decreased ratios around 25 ka and 17.5 ka, corresponding to simultaneous decreases in the benthic aU/Ca ratio and the planktonic aU/Ca ratio at ~17.5 ka (Figure 4). Additionally, *Uvigerina* spp. aU/Mn suggest changes in the sedimentary redox

554 chemistry associated with the YD interval. However, it is unclear how this relates to the
555 changes observed during MIS 2 due to the faunal shift in the benthic foraminiferal
556 assemblage.

557 Although previous studies suggested, that aU/Mn is less susceptible to species-specific
558 changes in the surface-to-mass ratio (Gottschalk et al., 2016), benthic foraminiferal aU/Mn
559 decreases across the deglaciation associated with the shift from *I. norcrossi* to *Uvigerina* spp.,
560 while planktonic aU/Ca increases and the preservation of laminated sediments at Site U1343
561 indicate more reducing conditions (Figure 4, Supplementary Figure 1). There are several
562 potential explanations for the observed discrepancy. Firstly, planktonic aU/Ca and benthic
563 aU/Mn were not measured on the same sample material across MIS 1. Thus, it is possible that
564 both reflect actual changes in the sedimentary redox chemistry with large shifts on relatively
565 short timescales of ~1 ka (Figure 4). On the other hand, benthic aU/Mn may be subject to
566 species-specific effects, similar to benthic aU/Ca. Species-specific effects may result from
567 differences in the accumulation of authigenic carbonates due to differences in the surface-to-
568 mass ratio or shell morphology and/or differences in the partitioning of Mn and U into
569 primary foraminiferal calcite. Both U/Ca and Mn/Ca ratios of benthic foraminifera are within
570 the range expected for primary foraminiferal calcite across the analyzed interval (<23
571 nmol/mol and <50 µmol/mol for U/Ca and Mn/Ca, respectively (Chen et al., 2017; Raitzsch
572 et al., 2011; Russell et al., 2004)). Even though the co-variance of benthic and planktonic
573 U/Ca ratios strongly supports a signal of predominantly authigenic origin, relatively low
574 U/Ca and Mn/Ca ratios could result in aU/Mn being more susceptible to species-specific
575 differences in the primary trace metal partitioning. Koho et al. (2017), for example,
576 demonstrate differences in the primary foraminiferal Mn/Ca ratio based on the microhabitat
577 preferences of the living organism, with deep infaunal foraminifera having higher Mn/Ca
578 ratios in response to changes in the dissolved Mn concentrations. If microhabitat preferences

were the determining factor of foraminiferal Mn/Ca ratios, an average Mn/Ca of 40.6 µmol/mol and 11.4 µmol/mol for *Uvigerina* spp. and *I. norcrossi*, respectively would suggest a shallower habitat for *I. norcrossi*. While *Uvigerina* spp. has a proposed habitat depth of 1-2 cm within the sediment (Tachikawa and Elderfield, 2002), *I. norcrossi* may be migrating between shallower and deeper layers in search of a preferred microhabitat (Hunt and Corliss, 1993; Ishimura et al., 2012; Ivanova et al., 2008), potentially in line with the observed differences in Mn/Ca ratios between the two species. Further, results by Skinner et al. (2019) suggest that Mn and U may be incorporated into authigenic foraminiferal coatings in different ways, with Mn tracking the dissolved pore water Mn concentrations, while U appears to record changes in the U-flux to the sediments, complicating a straightforward application of aU/Mn as a proxy for changes in the sedimentary redox chemistry.

Nonetheless, aU/Mn of *I. norcrossi* supports the two intervals of less reducing sedimentary redox conditions across MIS 2 (~17.5 and 25 ka), observed in both benthic and planktonic aU/Ca (Figure 4). Across the deglaciation planktonic aU/Ca seems to provide the most reliable trends in sedimentary redox chemistry changes, as benthic aU/Ca and aU/Mn are likely affected by changes in the assemblage composition and thus subject to species-specific effects (Figure 4).

4.3 Benthic foraminiferal assemblage

At Site U1343 the dominant benthic foraminiferal species are *Elphidium batialis* Saidova (1961), *Uvigerina* spp., *Islandiella norcrossi* (Cushman, 1933), *Bulimina exilis* Brady (1884), *Cassidulinoides parkerianus* (Brady, 1881), *Nonionella labradorica* (Dawson, 1860), *Valvulineria araucana* (D’Orbigny, 1839), and *Globobulimina* spp. (predominantly *G. pacifica* Cushman (1927) and *G. affinis* (D’Orbigny, 1839)). When present, *B. exilis* typically occurs in large abundances and dominates the benthic foraminiferal assemblage. *B. exilis* is

603 tolerant to hypoxic conditions and has previously been reported from environments with very
604 high primary productivity and export of labile organic matter to the seafloor (Caralp, 1989;
605 Caulle et al., 2014; Filipsson et al., 2011; Jannink et al., 1998; McKay et al., 2016). During
606 MIS 2 the abundance of *B. exilis* varies between 30-45 % (Figure 4) with two pronounced
607 decreases to 20 % at ~25 ka and 1.5-3 % between ~16.4-17.4 ka (Figure 4). Following the
608 latter decrease the abundance increases to >80 % and then remains high throughout MIS 1
609 compared to MIS 2 (Figure 4).

610 The CA analysis also reveals clear changes in the benthic foraminiferal assemblage across the
611 last glacial interval and the deglaciation. CA axis 1 describes 45 % of the total variance in the
612 dataset, with negative scores for *B. exilis*, *N. labradorica*, and *Uvigerina* spp. (Assemblage 1)
613 and positive scores for *E. batialis*, *N. digitata*, *Globobulimina* spp., and *I. norcrossi*
614 (Assemblage 2) (Supplementary Figure 6). CA axis 2 explains 24 % of the total variance and
615 shows negative correlation with *C. parkerianus*, *V. araucana*, and *I. norcrossi* (Assemblage
616 3) and positive correlation with *E. batialis*, *N. digitata*, and *Uvigerina* spp. (Supplementary
617 Figure 6). Axes 3 explains 12 % of the variance but does not define another meaningful
618 assemblage.

619 MIS 2 is dominated by Assemblage 3, as seen from the negative scores for CA axis 2. The
620 even lower scores during HS1 and Heinrich Stadial 2 (HS2, 24.3-26.5 ka) are driven by an
621 increase in the abundance of *C. parkerianus* (Figure 4). Simultaneously, CA axis 1 increases
622 during HS1 and HS2, driven by a decrease in the abundance of *B. exilis* (Figure 4). Across
623 the deglaciation, Assemblage 1 becomes dominant, as seen from the decrease in scores for
624 CA axis 1 (Figure 4). The increase in the scores for CA axis 2 during the deglaciation is
625 dominated by the occurrence of *Uvigerina* spp., while all other species positively correlated
626 with CA axis 2 remain low.

5. Discussion

5.1 Sea-ice dynamics in the eastern Bering Sea and the subarctic North Pacific across the last ~40 ka

The seasonal extent of sea ice in the modern Bering Sea is governed by the interplay of atmospheric and oceanic forcings (Zhang et al., 2010). While low atmospheric and sea surface temperatures (SST) initiate sea ice formation during winter, prevailing northerly winds over the Bering Sea cause a south-eastward expansion, with the maximum position of the ice edge determined by the SST-induced melting of sea ice (Zhang et al., 2010). Across the last ~ 40 ka, these boundary conditions changed continuously in response to global climate and the transition from a glacial to an interglacial state, affecting the sea-ice concentration in the Bering Sea and the subarctic North Pacific.

Biomarker-based sea-ice reconstructions at Site U1343 in the eastern Bering Sea reveal dynamic behavior on G/IG timescales, with an overall decrease in the spring sea-ice concentration between the last glacial maximum (LGM) and the early Holocene and millennial-scale variability across the last deglaciation (Figure 2). Late MIS 3 to LGM conditions are characterized by elevated IP_{25} concentrations, with maximum values during early MIS 2 (Figure 2). Contemporaneously, HBI III and sterol concentrations are low, in line with the MAR_{opal} at Site U1343 (Kim et al., 2014) (Figure 2), attributed to low primary productivity and no spring sea ice bloom in the vicinity of the core site. In combination with the $P_{III}IP_{25}$, P_BIP_{25}, and CT results (Figure 3) this suggests extensive seasonal sea ice in the eastern Bering Sea during late MIS 3 and early MIS 2 with a transition towards slightly decreased sea-ice extent around 23 ka (Figure 2, Figure 3). This is corroborated by radiolarian and diatom assemblages in the north-eastern Bering Sea and at the Umnak Plateau (Caissie et al., 2010; Itaki et al., 2012). While the record of diatom assemblages only reaches

back to ~22 ka, the abundance of *Actinomma boreale* and *A. leptodermum*, radiolarian species characteristic of extensive to perennial sea ice environments, is highest during early MIS 2, decreasing towards ~23 ka and again at ~21 ka (Figure 5) (Itaki et al., 2012). Thus, throughout the studied interval, the eastern Bering Sea might have experienced the most severe sea-ice conditions during early MIS 2, coinciding with HS2. Additional support for an expanded sea-ice cover during MIS 2 compared to today, comes from sea-ice biomarker studies in the eastern (SO202-27-6) and western (SO202-07-6) North Pacific (Figure 5), demonstrating extended to marginal sea-ice conditions, respectively (Méheust et al., 2018) and the central Sea of Okhotsk (Lo et al., 2018). In contrast, sea ice related diatoms are absent in LGM sediments at the Bowers Ridge (BOW-12A) (Katsuki and Takahashi, 2005), while IRD occurrence is consistently high (GC-11, GC-13) (Gorbarenko et al., 2010), indicating (at least) the occurrence of drift ice in the central southern Bering Sea.

As previously mentioned, the sea-ice extent in the Bering Sea is sensitive to the interaction of atmospheric and oceanic forcing mechanisms (Zhang et al., 2010). Reconstructions of SST in the subarctic North Pacific and its marginal seas across the LGM reveal large spatial heterogeneity, with some sites documenting warming from the LGM to the Holocene, while others show no change or even cooling (Caissie et al., 2010; Gebhardt et al., 2008; Gray et al., 2020; Harada et al., 2008, 2006, 2004; Hernández-Almeida et al., 2020; Kiefer and Kienast, 2005; Max et al., 2012; Méheust et al., 2018; Meyer et al., 2016; Praetorius et al., 2020; Riethdorf et al., 2013; Taylor et al., 2014) (Supplementary Figure 8, Supplementary Table 1). This discrepancy can partly be attributed to the varying proxy carriers used as paleothermometers, including microfossil assemblages, planktonic foraminiferal Mg/Ca, alkenone unsaturation indices, and the Tetra Ether indeX (TEX_{86}). Such proxies may be biased towards subsurface vs. surface temperatures, and/or temperatures during the respective bloom seasons, which might have changed across G/IG transitions. Nonetheless, a spatially

heterogeneous North Pacific SST development contrasts a region-wide expanded sea-ice cover during the LGM (Supplementary Table 1). A potential mechanism to reconcile this divergence would be an increased sensitivity of sea ice to atmospheric temperatures and circulation, rather than oceanic dynamics.

Numerical simulations and proxy reconstructions suggest a strengthening and expansion of the North Pacific subarctic gyre caused by a southward shift of the mid-latitude westerlies and polar easterlies during the LGM in response to the Laurentide ice sheet and atmospheric CO_2 concentrations (Gray et al., 2020; Nagashima et al., 2007). The strengthened wind stress curl over the subarctic North Pacific might have caused enhanced thermodynamic ice growth, as well as increased export of sea ice away from the nucleation sites, in line with the regional-wide increase of sea-ice extent during MIS 2 (Caissie et al., 2010; Itaki et al., 2012; Lo et al., 2018; Méheust et al., 2018). Further, weakening of the oceanic connection between the subarctic North Pacific gyre and the Bering Sea via the Alaskan Stream due to sea level fall and restriction of several Aleutian passes (Caissie et al., 2010; Meyer et al., 2016; Riethdorf et al., 2013), as well as closure of the Bering Strait may have isolated the glacial Bering Sea making it more sensitive to atmospheric rather than oceanic forcing. A strong sensitivity to atmospheric temperatures is supported by the decrease in sea ice extent around ~23 ka (Figure 5). This is contemporaneous with an increase in atmospheric temperatures over Greenland, as suggested by the North Greenland Ice Core Project (NGRIP) $\delta^{18}O$ curve (Rasmussen et al., 2006; Svensson et al., 2008; Vinther et al., 2006) (Figure 5), indicating close atmospheric coupling between the Bering Sea and the North Atlantic during MIS 2. This decrease, however, is not observed in the eastern and western subarctic Pacific (Méheust et al., 2018) (Figure 5). Although the records are of relatively low resolution, this could indicate that sea-ice extent in the western and eastern North Pacific was additionally modulated by oceanic changes in relation to the subarctic gyre dynamics. Different

sensitivities to oceanic and atmospheric forcing between the eastern Bering Sea and eastern North Pacific are further supported by the lack of correlation between IP_{25} records from these two regions during the LGM, which changes to a significant positive correlation during HS1 (Supplementary Figure 7).

HS1 is marked by a double peak in IP_{25} and HBI II in the eastern Bering Sea, also recognized in the eastern North Pacific (Méheust et al., 2018) (Figure 5, Supplementary Figure 7). In the eastern North Pacific, the double peak is associated with an increase in brassicasterol, suggesting more marginal sea-conditions compared to the LGM. Seasonal sea-ice conditions during HS1 are also evident from biomarker records in the western North Pacific (Méheust et al., 2018, 2016) (Figure 5). In the eastern Bering Sea, on the other hand, the collective biomarker data for the early HS1 peak indicate extended seasonal sea ice in line with the $P_{III}IP_{25}$, P_BIP_{25}, and CT results (Figure 2, Figure 3). This is supported by the re-appearance of the radiolarian species *A. boreale* and *A. leptodermum*, in the north-eastern Bering Sea (Itaki et al., 2012) (Figure 5), characteristic of an extensive sea-ice cover. Further, diatom assemblages at the Umnak Plateau suggest more than 6 months of sea-ice per year during early HS1 (Caissie et al., 2010), in line with biomarker records from the Shirshov Ridge in the western Bering Sea also indicating extensive sea-ice cover (Méheust et al., 2016).

Contemporaneous IP_{25} peaks in the eastern North Pacific and the eastern Bering Sea during HS1 could indicate a more unified forcing in the eastern subarctic Pacific during HS1 compared to the LGM (Supplementary Figure 7), although higher resolution records are needed to confirm the observed similarities. As the oceanic connection between the eastern Bering Sea and the eastern North Pacific was still restricted during the early deglaciation (Supplementary Figure 7), one possibility would be a heightened sensitivity to atmospheric temperatures. While NGRIP $\delta^{18}O$ suggests warming over Greenland during early HS1 (Rasmussen et al., 2006; Svensson et al., 2008; Vinther et al., 2006), North Greenland

Eemian Ice Drilling (NEEM) $\delta^{18}O$ (Buizert et al., 2014) and the northern hemisphere temperature stack (Shakun et al., 2012) both indicate atmospheric cooling (Figure 5). Under glacial boundary conditions, NEEM might be more representative of Pacific climate and moisture fluxes, compared to NGRIP (Buizert et al., 2014). Atmospheric cooling during early HS1 is further supported by pollen records from eastern Beringia (150-180°W) (Viau et al., 2008) (Figure 5). Alternatively, flood events from the retreating Cordilleran Ice Sheet, routed into the eastern North Pacific might have caused surface ocean cooling and freshening during the early deglaciation, causing region-wide synchronous sea-ice patterns (Praetorius et al., 2020). However, while a compilation of SST records from the eastern North Pacific suggests cooling during the early HS1 compared to the LGM (Praetorius et al., 2020), available Bering Sea SST records indicate early warming from ~19 ka (Hernández-Almeida et al., 2020; Meyer et al., 2016; Riethdorf et al., 2013), with only transient cooling events (Supplementary Figure 8). Warming SSTs, especially during the summer season (Meyer et al., 2016), at the same time as an increase in the sea-ice extent, might suggest a larger seasonal contrast in the Bering Sea during early HS1 compared to the LGM.

Following the interval of enhanced sea-ice cover during early HS1 (~17.5 ka), the second HS1 peak in IP_{25} is associated with increased HBI III and brassicasterol, suggesting a shift towards MIZ conditions in the eastern Bering Sea around 16.5 ka (Figure 2). This is supported by a more dynamic sea-ice cover at the Umnak Plateau from ~16.7 ka onwards (Caissie et al., 2010) and the disappearance of *A. boreale* and *A. leptodermum* in the northern Bering Sea (Itaki et al., 2012) (Figure 5). From 16 ka onward, a sharp decline in all three HBI biomarkers is observed at Site U1343, contemporaneous with a decrease of IP_{25} in the eastern North Pacific (Figure 2, Figure 5) (Méheust et al., 2018). At the same time all sterol biomarkers, as well as MAR_{opal}, start to increase rapidly (Figure 2), indicating a northward retreat of the sea-ice margin in the eastern Bering Sea and eastern North Pacific during late

HS1. This sea-ice retreat is synchronous with local and northern hemisphere atmospheric warming (Kurek et al., 2009; Shakun et al., 2012; Viau et al., 2008) and increasing northern hemisphere summer insolation (Figure 5).

In contrast, biomarker records from the western Bering Sea and the western North Pacific, as well as in the central Sea of Okhotsk, document continuously extensive sea ice until ~15 ka (Lo et al., 2018; Méheust et al., 2018, 2016) (Figure 5). This suggests an east-west gradient in the late HS1 sea-ice retreat in the subarctic North Pacific. Recently, using planktonic foraminiferal $\delta^{18}O$ and numerical simulations, Gray et al. (2020) demonstrated an east-west gradient in the deglacial northward migration of the subarctic gyre. From 16.5 ka onwards, northward migration of the gyre boundary is evident in the eastern subarctic Pacific, while the western boundary changes occur between ~12.5-10 ka (Gray et al., 2020). Further, Gong et al. (2019) demonstrate a strengthened Aleutian Low during HS1, which transports cold air masses from East Siberia to the Sea of Okhotsk and the western Bering Sea. Thus, an east-west gradient in deglacial sea-ice dynamics is consistent with atmospheric and oceanic circulation patterns at this time, suggesting colder conditions in the west compared to the east during late HS1. The latter is also observed in a recent compilation of high resolution SST reconstructions, showing colder SSTs in the western North Pacific compared to the east during late HS1 (Praetorius et al., 2020).

From ~15 ka, however, sea-ice biomarker records demonstrate a consistent decrease in the Bering Sea and the subarctic North Pacific sea-ice cover (Figure 5) (Méheust et al., 2018, 2016); while the record from the central Sea of Okhotsk indicates a transition towards marginal sea-ice conditions (Lo et al., 2018). This is in line with substantial hemisphere-wide atmospheric (Shakun et al., 2012) and region-wide SST warming at the onset of the BA (Caissie et al., 2010; Hernández-Almeida et al., 2020; Max et al., 2012; Méheust et al., 2018; Meyer et al., 2016; Praetorius et al., 2020; Riethdorf et al., 2013) (Supplementary Figure 8).

Consistent with warming during the BA, sea-ice biomarker records at Site U1343 suggest predominantly ice-free conditions, with a renewed increase in MIZ sedimentation during the late BA, as indicated by increasing HBI III concentrations (Figure 2). An ice-free environment is further supported by very high sterol concentrations throughout the BA and a peak in MAR_{opal} (Figure 2), attributed to increased primary productivity and increased continental runoff throughout this interval (Supplementary Figure 9). Ice-free conditions in the eastern Bering Sea are consistent with previous biomarker-based sea-ice reconstructions from the western Bering Sea and the subarctic North Pacific (Méheust et al., 2018, 2016), also indicating very low spring sea-ice occurrence during the early and mid-BA (Figure 5). Diatom assemblages at the Umnak Plateau, on the other hand, suggest a shift from near perennial to seasonal sea ice associated with the onset of the BA, while ice-free conditions are not encountered until 11 ka (Caissie et al., 2010). This suggests a discrepancy between biomarker-based and diatom-based sea-ice reconstruction in the deglacial Bering Sea and further research is needed to understand the cause of this disagreement. Nonetheless, diatoms characteristic of high productivity environments seem to dominate the assemblage at the Umnak plateau during the BA (Caissie et al., 2010), indicative of a major environmental shift and reduced ice cover compared to HS1.

Following peak BA northern hemisphere warmth at ~13.5 ka, atmospheric temperatures (Shakun et al., 2012) and Bering Sea SSTs (Hernández-Almeida et al., 2020; Max et al., 2012; Méheust et al., 2018; Meyer et al., 2016) decrease into the YD stadial (Figure 5, Supplementary Figure 8). Simultaneously, sea-ice biomarkers increase in the western and eastern Bering Sea (Méheust et al., 2016) (Figure 5). An increase in IP_{25} is also observed in the western North Pacific off Kamchatka, while the Emperor Seamount further to the east remained ice-free during the YD (Méheust et al., 2018). In the central Sea of Okhotsk IP_{25} is slightly lower compared to the BA. In combination with lowered HBI III concentrations,

however, this also indicates a renewed sea-ice advance compared to the BA interstadial (Lo et al., 2018). The YD stadial is thus characterized by seasonal sea ice in the Bering Sea, off Kamchatka and in the central Sea of Okhotsk (Lo et al., 2018; Méheust et al., 2018, 2016). MIZ conditions with high HBI III concentrations at Site U1343 (Figure 2), however, suggest that, at least in the eastern Bering Sea, sea ice did not extend as far south as during early HS1. This is in line with sea ice not reaching the Bowers Ridge during the YD stadial (Cook et al., 2005).

The early Holocene is characterized by ice-free conditions in the Bering Sea, the subarctic North Pacific, and the central Sea of Okhotsk, with a mid-Holocene increase in IP_{25} accumulation observed in the northern and western Bering Sea after ~10 ka (Figure 5) (Caissie et al., 2010; Itaki et al., 2012; Lo et al., 2018; Méheust et al., 2016, 2018). Diatom assemblages at the Umnak Plateau also suggest ice-free conditions during the early Holocene (Caissie et al., 2010). This is consistent with substantial environmental changes in the Bering Sea during the early Holocene, corresponding to a widespread regional warming (Elias et al., 1996; Kaufman et al., 2004) in response to maximum northern hemisphere summer insolation (Kaufman et al., 2004). Further, deglacial sea level rise resulted in the flooding of the Bering Land Bridge around 11 ka (Jakobsson et al., 2017) and enhanced influence of warm and nutrient-rich Alaskan Stream waters in the eastern Bering Sea (Caissie et al., 2010). While the MAR_{opal}, cholesterol, and brassicasterol are relatively low during the early Holocene, campesterol and β-sitosterol peak following the YD/Holocene transition (Figure 2). Contemporaneously, the abundance of radiolarian species, indicative of melt-water discharge spike in the northern Bering Sea (Itaki et al., 2012), suggesting increased continental runoff and input of terrestrial organic matter (Supplementary Figure 9).

From ~11 ka onwards, HBI III values at Site U1343 increase by orders of magnitude, yet the IP_{25}, HBI II and brassicasterol concentrations remain low, indicating absence of MIZ

sedimentation at Site U1343. Similar biomarker patterns have been observed in sediment cores from the Barents Sea and the Norwegian Sea (Belt et al., 2015; Berben et al., 2017; Xiao et al., 2017), with absent IP_{25} and increased HBI III from 9.9-8.0 ka and 11.2-9.3 ka, respectively (Belt et al., 2015). This was attributed to enhanced warm Atlantic Water inflow resulting in increased productivity. In the eastern Bering Sea, we suggest that the steep increase in HBI III is most likely related to warming and enhanced nutrient concentrations during the early Holocene. At the Umnak Plateau the abundance of *Rhizosolenia hebetata*, a known producer of HBI III (Belt et al., 2017), increases from 9 ka onwards, together with increased occurrence of *Neodenticula seminae*, a species characteristic of the Alaskan Stream (Caissie et al., 2010). Species of the genus *Rhizosolenia* are often associated with oceanic fronts (Oksman et al., 2019), regions of enhanced nutrient supply. Thus, strengthened inflow of warm, nutrient-rich Alaskan Stream waters into the eastern Bering Sea potentially created an environment especially suitable for HBI III producing diatoms.

5.2 Ventilation changes in the eastern Bering Sea over the last ~30 ka and the role of sea ice for glacial NPIW formation

Under modern conditions, deep water masses are formed in the North Atlantic and the Southern Ocean, while in the North Pacific, a permanent halocline (Emile-Geay et al., 2003; Warren, 1983) impedes the formation of deep water masses. Instead, intermediate water forms via brine rejection during sea-ice freezing in the Sea of Okhotsk (Shcherbina et al., 2003; Talley, 1993). Numerous proxy studies and numerical simulations indicate that intermediate depths of the North Pacific experienced enhanced ventilation during the LGM (GNPIW) and especially during stadial periods of the last deglaciation (Ahagon et al., 2003; Cook et al., 2016; Cook and Keigwin, 2015; Duplessy et al., 1989; Gong et al., 2019; Jaccard and Galbraith, 2013; Jang et al., 2017; Keigwin, 1998; Knudson and Ravelo, 2015; Matsumoto et al., 2002; Max et al., 2014; Okazaki et al., 2010, 2012; Ovsepyan et al., 2017;

Rae et al., 2014; Saenko et al., 2004; Sagawa and Ikehara, 2008; Worne et al., 2019; Zou et al., 2020) (Supplementary Table 1). This suggests an Atlantic-Pacific overturning seesaw with increased Pacific meridional overturning circulation (PMOC) at times of a reduced AMOC (McManus et al., 2004). Improved ventilation of the glacial North Pacific from GNPIW is widely recorded to depth of up to ~2000 m, while HS1 might have experienced enhanced ventilation up to >3000 m (Okazaki et al., 2010; Rae et al., 2014). This is in contrast to NPDW, which was characterized by reduced oxygen concentrations during the LGM (Jaccard et al., 2009), likely a result of changes in the preformed to regenerated nutrient ratio, facilitating deep ocean carbon storage (Galbraith et al., 2007; Jaccard et al., 2009). Across the deglaciation, during the BA and the early Holocene, these trends were reversed. NPDW experienced improved ventilation (Galbraith et al., 2007), while the mid-depth North Pacific was marked by widespread anoxia (Aiello and Ravelo, 2012; Cook et al., 2005; Expedition 323 Scientists, 2010; Kuehn et al., 2014; Ovsepyan et al., 2017; Pelto et al., 2018; Rella et al., 2012).

At ~2000 m water depth, Site U1343 is located at the proposed boundary of GNPIW and NPDW, making it ideal to study past changes in North Pacific ventilation. However, the records of benthic foraminiferal assemblages, planktonic and benthic aU/Ca, and benthic aU/Mn are of relatively low resolution due to low foraminiferal abundance in the sediments. The most robust features are two distinct events of less reducing conditions at ~17.5 ka and ~25 ka, marked by decreased aU/Ca, aU/Mn, and a lower abundance of hypoxia-tolerant benthic foraminiferal species from Assemblage 1, including *B. exilis* (Supplementary Figure 6, Figure 4). Further, planktonic aU/Ca and the benthic foraminiferal assemblage suggest more reducing conditions associated with the BA and the early Holocene, characterized by elevated planktonic aU/Ca and a dominance of *B. exilis* in sediments at Site U1343 (Figure 4).

The two events of less reducing conditions at ~17.5 ka and ~25 ka, correspond to early HS1 and late HS2, respectively (Figure 6). As there are no changes in the MAR_{opal}, representing first order changes in primary productivity, during these intervals (Figure 6), the two events are interpreted to reflect increased bottom water oxygenation. Two primary reasons have been identified for enhanced bottom water oxygen concentrations: (i) enhanced ventilation (via lateral or vertical water mass exchange) or (ii) the release of carbon from the deep ocean. Volumetrically, the deep North Pacific represents the largest reservoir of carbon in the world’s deep ocean. Thus, a release of carbon from the North Pacific abyss should result in increased atmospheric CO_2 concentrations and/or increased primary productivity, capturing the released carbon. Atmospheric CO_2, however, does not increase significantly until 17 ka (Bereiter et al., 2015) and subarctic North Pacific primary productivity remains low until ~16 ka (Brunelle et al., 2010, 2007; Cook et al., 2005; Kim et al., 2014; Kohfeld and Chase, 2011; Lam et al., 2013; Max et al., 2012; Okazaki et al., 2005). Further, NPDW ventilation does not increase on a region-wide scale until the onset of the BA (Galbraith et al., 2007; Jaccard et al., 2009; Jaccard and Galbraith, 2012; Lund et al., 2011), suggesting that deep ocean carbon release did not drive the increased sedimentary oxygenation at 25 ka and 17.5 ka in the eastern Bering Sea. Instead, we attribute improved ventilation via expansion of GNPIW as the cause for the enhanced oxygenation of sediments at Site U1343 during late HS2 and early HS1.

As research has primarily focused on the deglacial history of North Pacific ventilation, few records reach as far back as HS2. However, there is evidence for improved ventilation in the Okinawa Trough at 703 m water depth, attributed to enhanced formation and ventilation of GNPIW (Zou et al., 2020). Further, records of oxic benthic foraminiferal abundance peak around 25 ka in a sediment core from 1300 m water depth off Japan (Shibahara et al., 2007) as well as at 500-600 m water depth in the Santa Barbara Basin (Cannariato and Kennett,

1999; Ohkushi et al., 2013). Under modern conditions, these sites are from the distal reaches of NPIW, however records of foraminiferal carbon isotopes ($\delta^{13}C$) suggest that GNPIW extended further south under glacial boundary conditions (Max et al., 2017). In contrast, more proximal records of $\delta^{13}C$ from the mid-depth Bering Sea (600-1000 m) do not show a clear signal of improved ventilation during HS2 (Max et al., 2017; Rella et al., 2012) (Figure 6). As the age model at Site U1343 is more uncertain at the lower end of the record, further research is needed to confirm the exact timing and duration of the proposed deep ventilation event.

The second ventilation event at 17.5 ka during early HS1 coincides with the onset of widespread improved ventilation in the mid-depth Bering Sea and Sea of Okhotsk (Gorbarenko et al., 2010; Max et al., 2014; Rella et al., 2012) (Figure 6), and precedes a deep ventilation event to >3000 m water depth observed in the Gulf of Alaska by ~500 years (Rae et al., 2014). Evidence for improved ventilation at ~17.5 ka is also available from the wider North Pacific region off Japan (978-2700 m) (Ahagon et al., 2003; Ohkouchi et al., 1994; Zou et al., 2020) and off California and Baja California (500-600 m) (Cannariato and Kennett, 1999; Ohkushi et al., 2013; Tetard et al., 2017).

Compared to shallower records from the northern and western Bering Sea (975-1000 m), where improved ventilation is sustained until 16 ka and 15 ka, respectively (Max et al., 2014; Rella et al., 2012), the ventilation event at U1343 seems to be of relatively short duration, indicating a pulse of enhanced GNPIW formation to 2000 m water depth in the eastern Bering Sea during early HS1 (Figure 6). Increased North Pacific overturning during HS1 is further supported by records of carbon cycle dynamics. From 17.5 ka onwards, diatom-bound nitrogen isotopes ($\delta^{15}N$) suggest a decrease in the nutrient utilization in the Bering Sea (Brunelle et al., 2010, 2007) and North Pacific surface ocean CO_2 partial pressure (pCO_2) shows a transient increase during early HS1 (Gray et al., 2018) (Figure 6). This is attributed

to increased mixing of nutrient and CO_2-rich deep water to the surface at the onset of deep overturning during HS1. Subsequently, deepening of the relatively warm and fresh GNPIW intensified the deep ocean stratification, preventing further upwelling of NPDW until the breakdown of GNPIW formation at the HS1/BA transition (Gong et al., 2019; Gray et al., 2018). While nutrient utilization decreases from 17.5 ka (Figure 6), primary productivity in the subarctic North Pacific remains low until 16 ka (Brunelle et al., 2010, 2007; Cook et al., 2005; Kim et al., 2014; Kohfeld and Chase, 2011; Lam et al., 2013; Max et al., 2012; Okazaki et al., 2005; Riethdorf et al., 2016), which can be attributed to light limitation in response to seasonal sea-ice cover and a deepened mixed layer due to enhanced GNPIW formation.

Improved ventilation of the mid-depth North Pacific during HS1, observed in numerous studies from the subarctic to the subtropics (Ahagon et al., 2003; Cannariato and Kennett, 1999; Cook et al., 2016; Duplessy et al., 1989; Gorbarenko et al., 2010; Max et al., 2014; Ohkushi et al., 2013; Rae et al., 2014; Rella et al., 2012; Sagawa and Ikehara, 2008; Shibahara et al., 2007; Tetard et al., 2017; Zou et al., 2020) (Supplementary Table 1), is in line with increased overturning in the North Pacific at times of a reduced AMOC. The reasons for a stronger PMOC, however, are still under debate. Several numerical simulations suggest prominent changes in the atmospheric circulation over the subtropical and subarctic North Pacific in response to reduced northward heat transport in the Atlantic during an AMOC-off mode (Chikamoto et al., 2012; Gong et al., 2019; Menviel et al., 2012; Okazaki et al., 2010; Okumura et al., 2009; Wu et al., 2008). These changes include a southward shift in the Intertropical Convergence Zone (ITCZ) (Chikamoto et al., 2012; Okumura et al., 2009; Wu et al., 2008), stronger midlatitude westerlies (Gong et al., 2019; Okumura et al., 2009), and a strengthened Aleutian Low over the subarctic North Pacific (Chikamoto et al., 2012; Gong et al., 2019; Okumura et al., 2009). A stronger Aleutian Low results in colder, drier

East Siberian air masses over the western Bering Sea and Sea of Okhotsk reducing the net precipitation in this region (Gong et al., 2019). Additionally, strengthened atmospheric circulation would lead to a spin up of the subarctic North Pacific gyre with enhanced Ekman suction and increased meridional transport of saline subtropical waters to the subarctic North Pacific (Chikamoto et al., 2012; Gong et al., 2019; Gray et al., 2020; Menviel et al., 2012; Okazaki et al., 2010; Okumura et al., 2009). In combination, these processes might act to increase the North Pacific surface ocean salinity (SSS), which could weaken the permanent halocline, initiating thermohaline overturning. A positive overturning-salinity feedback might then aid to sustain high SSS in the North Pacific (Chikamoto et al., 2012; Gong et al., 2019; Max et al., 2014). Along with increased meridional transport, several models suggest an enhanced northward heat transport in the Pacific in response to increased overturning (Chikamoto et al., 2012; Gong et al., 2019; Menviel et al., 2012; Okazaki et al., 2010). In contrast, studies of foraminiferal $\delta^{18}O$ and εNd in the Bering Sea suggest a pivotal role of brine rejection during sea-ice freezing for enhanced GNPIW formation (Cook et al., 2016; Horikawa et al., 2010; Knudson and Ravelo, 2015).

Both deep ventilation events, as recognized at Site U1343, correspond to times of increased sea-ice extent in the eastern Bering Sea (Figure 6). Especially during early HS1, warming Bering Sea summer SSTs (Meyer et al., 2016) in combination with increased sea-ice extent suggest a stronger seasonal contrast, likely associated with intensified new ice growth and brine rejection. Brine rejection during early HS1 and late HS2 is also supported by the $\delta^{18}O_b$ at Site U1343 (Asahi et al., 2016). During sea-ice freezing, brine rejection leads to an increase in surface water salinity without significantly fractionating surface water $\delta^{18}O$ (Brennan et al., 2013), transporting the low surface water $\delta^{18}O$ signature to greater depth, resulting in a negative offset of local benthic $\delta^{18}O$ from the global benthic $\delta^{18}O$ stack (LR04) (Knudson and Ravelo, 2015; Lisiecki and Raymo, 2005). Even though $\delta^{18}O_b$ at Site U1343 is

of relatively low resolution, negative offsets from the LR04 stack can be observed across both ventilation events, albeit of lower amplitude compared to IODP Site U1342 at 800 m water depth in the southern Bering Sea (Figure 6) (Knudson and Ravelo, 2015). The difference between $\delta^{18}O_b$ at Site U1343 and the shallower Site U1342 (~800 m), as well as the similarities between U1343 $\delta^{18}O_b$ and the LR04 stack, however, suggest that NPDW remained the predominant water mass at ~2000 m in the eastern Bering Sea during MIS 2, with entrainment of GNPIW restricted to the two deep ventilation events during HS1 and HS2.

This indicates that while the LGM in the Bering Sea, in line with glacial intervals of the last 1.2 Ma, may have experienced enhanced GNPIW ventilation to depth of ~1000 m (Cook et al., 2016; Knudson and Ravelo, 2015; Rella et al., 2012), deep convection to at least 2000 m was restricted to HS1 and potentially also HS2 (Figure 7). We propose that during early HS1 increased brine rejection locally weakened the halocline by promoting downward transport of low salinity surface waters and upward mixing of higher salinity intermediate waters (Figure 7). Thus, enhanced sea-ice formation during early HS1 in the Bering Sea and the subarctic North Pacific might have helped to ‘kick start’ deep convection, in line with the observed pulse of improved ventilation at 2000 m water depth in the eastern Bering Sea (Figure 6). The subsequent northward retreat of the sea-ice margin in the eastern Bering Sea and eastern North Pacific from ~16 ka onwards (Figure 5), however, suggests that while sea ice likely aided in the initiation of deep convection, other mechanisms might have been more important in sustaining increased ventilation until the onset of the BA. These mechanisms might include a positive salinity-circulation feedback, transporting high salinity subtropical waters to the North Pacific, decreased precipitation over the North Pacific, and/or increased upwelling of high salinity surface waters in the subarctic gyre due to intensified Ekman suction (Chikamoto et al., 2012; Gong et al., 2019; Gray et al., 2020; Max et al., 2014; Menviel et al.,

2012; Okazaki et al., 2010; Okumura et al., 2009). Alternatively, sustained brine rejection in the western Bering Sea and Sea of Okhotsk, in line with a later sea-ice demise (~15 ka) in this region (Figure 5) (Lo et al., 2018; Méheust et al., 2018, 2016), might have driven/contributed to enhanced North Pacific overturning during late HS1 (Gong et al., 2019).

An increased sea-ice cover during times of an intensified PMOC conflicts with results suggesting enhanced northward heat transport in response to PMOC strengthening (Chikamoto et al., 2012; Gong et al., 2019; Gray et al., 2020; Menviel et al., 2012; Okazaki et al., 2010). As mentioned in section 5.1, the increase in sea-ice extent during early HS1 is most likely a response to either atmospheric cooling (Kurek et al., 2009; Shakun et al., 2012; Viau et al., 2008) and/or meltwater runoff from the retreating Cordilleran Ice Sheet (Praetorius et al., 2020). If the former was the case, atmospheric cooling might have masked any significant increase in northward heat transport, as suggested in a recent modelling study (Gong et al., 2019). In contrast, a sea-ice increase in response to surface freshening is difficult to reconcile with the enhanced ventilation of the mid-depth North Pacific during HS1, unless brine rejection was able to compensate for the freshwater-induced halocline strengthening. In this case, input of cold freshwater might have compensated for increased northward heat transport, allowing for an extended sea-ice cover. Future modelling studies might be able to explore this relationship further.

From 16 ka onwards primary productivity increases on a North Pacific wide scale (Brunelle et al., 2010, 2007; Cook et al., 2005; Kim et al., 2014; Kohfeld and Chase, 2011; Lam et al., 2013; Max et al., 2012; Okazaki et al., 2005; Riethdorf et al., 2016). At Site U1343, rising primary productivity is recorded by a steep increase in MAR_{opal} (Kim et al., 2014) and sterol biomarkers from 16 ka, peaking during the early BA interstadial (Figure 2). As the timing corresponds to the onset of sea-ice decline (Figure 2), increased primary productivity was

likely a result of alleviation of light limitation due to diminishing sea-ice cover, and a shallower mixed layer, promoted by sea-ice melting inducing surface ocean stratification. At the HS1/BA transition, subarctic North Pacific surface ocean pCO_2 increased rapidly above atmospheric CO_2 concentrations at the time (Figure 6), indicating outgassing of CO_2 from the North Pacific (Gray et al., 2018). Gray et al. (2018) suggest that increased surface ocean pCO_2 resulted from the breakdown of GNPIW formation following the resumption of the AMOC (McManus et al., 2004) resulting in upwelling of NPDW, due to enhanced Ekman suction in the subarctic gyre as a result of the remnant Laurentide Ice Sheet. Enhanced upwelling of NPDW during the BA would have flushed deeply sequestered CO_2 and nutrients from the abyss to the surface, in line with signs of improved NPDW ventilation (Galbraith et al., 2007) and increased primary productivity in the North Pacific (Brunelle et al., 2010, 2007; Cook et al., 2005; Kim et al., 2014; Kohfeld and Chase, 2011; Lam et al., 2013; Max et al., 2012; Riethdorf et al., 2016).

Contemporaneously, planktonic aU/Ca and benthic foraminiferal assemblages at Site U1343 record reduced sedimentary oxygenation across the BA and the early Holocene (Figure 6). While the last glacial interval was dominated by Assemblage 3, predominately composed of phytodetritivore species (Kender et al. 2019), the BA and the early Holocene are dominated by Assemblage 1 (Figure 6). The latter is composed of species adapted to low oxygen conditions and very high export of organic carbon to the seafloor (Kender et al., 2019; Okazaki et al., 2005; Piña-Ochoa et al., 2010; Schumacher et al., 2007; Sen Gupta and Machain-Castillo, 1993), dominated by *B. exilis* (Figure 6). Decreased oxygenation is in line with the preservation of laminations in sediment core U1343 (Expedition 323 Scientists, 2010) (Supplementary Figure 1) and numerous other cores from the mid-depth Bering Sea (Aiello and Ravelo, 2012; Cook et al., 2005; Expedition 323 Scientists, 2010; Kuehn et al., 2014; Pelto et al., 2018; Schlung et al., 2013) and across the North Pacific (Crusius et al.,

2004; Ikehara et al., 2006; Praetorius et al., 2015; Zheng et al., 2000). Laminated sediments during the BA and the early Holocene suggest that waters with [O_2] <5 µmol/kg (Moffitt et al., 2015) intersected the sediment-water interface, bearing witness of a substantial intensification and expansion of the mid-depth OMZ throughout these intervals (Kuehn et al., 2014). During the BA, OMZ expansion was most likely attributed to enhanced respiration of organic carbon in the ocean interior due to increased export productivity (Figure 2), fueled by upwelling of nutrient-rich NPDW and increased mixed layer stratification as a result of warming atmospheric temperatures and enhanced meltwater discharge (Gray et al., 2018; Itaki et al., 2012; Kuehn et al., 2014; Ren et al., 2015) (Figure 7). Additionally, the breakdown of GNPIW formation likely contributed to reduced ventilation of the mid-depth North Pacific (Gray et al., 2018). During the early Holocene, on the other hand, sterol biomarkers and MAR_{opal} at Site U1343 indicate relatively lower in situ primary productivity compared to the BA (Figure 2). Instead, sterol biomarkers suggest enhanced input of terrestrial organic carbon due to sea level rise and increased meltwater discharge (Itaki et al., 2012; Spratt and Lisiecki, 2016) (Supplementary Figure 9) as the primary cause for OMZ expansion in the eastern Bering Sea.

6. Conclusions

1. MIS 3 and MIS 2 were characterized by seasonal to extended seasonal sea-ice concentration in the eastern Bering Sea, with the most severe sea-ice conditions occurring during early MIS 2.
2. Across the deglaciation, sea-ice dynamics in the eastern Bering Sea demonstrate millennial-scale variability. HS1 was marked by an initial intensification of sea-ice conditions around 17.5 ka, followed by a transition to MIZ conditions around 16.5 ka and a rapid northward retreat of the sea ice margin at the HS1/BA transition. The BA

and early Holocene were characterized by primarily ice-free conditions in the eastern Bering Sea, separated by a return of MIZ conditions during the YD.

3. The timing of sea-ice changes in the eastern Bering Sea, as well as its oceanic isolation due to glacial sea-level fall, suggest that sea ice was most sensitive to atmospheric forcing during MIS 3 and MIS 2. Across the deglaciation, the effects of oceanic forcing likely strengthened in response to sea level rise and subarctic gyre dynamics.
4. During late HS2 (~25 ka) and early HS1 (~17.5 ka), foraminiferal assemblages and authigenic trace metals, suggest pulses of improved ventilation at Site U1343, corresponding to times of enhanced sea-ice cover. Especially during early HS1, we propose that enhanced sea-ice formation aided in the initiation of deep overturning by locally weakening the halocline. The subsequent retreat of the sea-ice margin however indicates that other mechanisms, such as a positive circulation salinity feedback, and/or sea ice in the western Bering Sea/Sea of Okhotsk were more important to sustain deep overturning during HS1. As the age model becomes more uncertain towards the lower end of the record, additional research is needed, but the similarities between the events at 17.5 ka and 25 ka, suggest that deep ventilation initiated by sea-ice formation may have been a recurrent feature of Heinrich events in the North Pacific.
5. The dominance of the high productivity, hypoxia-tolerant benthic foraminiferal species *B. exilis* during the BA and the early Holocene, is in line with the preservation of laminations and OMZ expansion in the eastern Bering Sea. During the BA, high concentrations of all sterol biomarkers and MAR_{opal}, indicate that an increase in in situ primary productivity in combination with influx of terrestrial organic carbon drove down mid-depth oxygen concentrations. During the early Holocene, however,

terrestrial sterol biomarkers dominate, suggesting that organic carbon from meltwater runoff and sea level rise might have been the dominant driver of OMZ expansion at this time.

Acknowledgements

We would like to thank the IODP Kochi Core Center for providing the sample material for this study. H.D. would like to acknowledge funding through a Natural Environmental Research Council (NERC) Ph.D. research grant (NE/L002434/1), via the GW4+ Doctoral Training Partnership and funding provided by a BGS University Funding Initiative Ph.D. studentship (S268). Further, C.P. and H.D would like to acknowledge funding from through the Aarhus University Research Foundation.

Research data

Supporting data are can be accessed under the following link https://www.pangaea.de/tok/ba8f0a1a1a09bf6c18c671b20a9d4319b2d11b3b (please note that this is a preliminary link for reviewers only, which will expire after 100 days and will be updated upon acceptance of the manuscript).

References

Addison, J.A., Finney, B.P., Dean, W.E., Davies, M.H., Mix, A.C., Stoner, J.S., Jaeger, J.M., 2012. Productivity and sedimentary δ15N variability for the last 17,000 years along the northern Gulf of Alaska continental slope. Paleoceanography 27. https://doi.org/10.1029/2011PA002161

Aguilar-Islas, A.M., Hurst, M.P., Buck, K.N., Sohst, B., Smith, G.J., Lohan, M.C., Bruland, K.W., 2007. Micro- and macronutrients in the southeastern Bering Sea: Insight into iron-replete and iron-depleted regimes. Prog. Oceanogr. 73, 99–126. https://doi.org/10.1016/J.POCEAN.2006.12.002

Ahagon, N., Ohkushi, K., Uchida, M., Mishima, T., 2003. Mid-depth circulation in the northwest Pacific during the last deglaciation: Evidence from foraminiferal radiocarbon ages. Geophys. Res. Lett. 30, 2097. https://doi.org/10.1029/2003GL018287

Aiello, I.W., Ravelo, A.C., 2012. Evolution of marine sedimentation in the Bering Sea since the Pliocene. Geosphere 8, 1231–1253. https://doi.org/10.1130/GES00710.1

Asahi, H., Kender, S., Ikehara, M., Sakamoto, T., Takahashi, K., Ravelo, A.C., Alvarez Zarikian, C.A., Khim, B.K., Leng, M.J., 2016. Orbital-scale benthic foraminiferal oxygen isotope stratigraphy at the northern Bering Sea Slope Site U1343 (IODP Expedition 323) and its Pleistocene paleoceanographic significance. Deep Sea Res. Part II Top. Stud. Oceanogr. 125–126, 66–83. https://doi.org/10.1016/J.DSR2.2014.01.004

Barker, S., Greaves, M., Elderfield, H., 2003. A study of cleaning procedures used for foraminiferal Mg/Ca paleothermometry. Geochemistry, Geophys. Geosystems 4, 8407. https://doi.org/10.1029/2003GC000559

Belt, S.T., 2018. Source-specific biomarkers as proxies for Arctic and Antarctic sea ice. Org. Geochem. 125, 277–298. https://doi.org/10.1016/J.ORGGEOCHEM.2018.10.002

Belt, S.T., Brown, T.A., Rodriguez, A.N., Sanz, P.C., Tonkin, A., Ingle, R., 2012. A reproducible method for the extraction, identification and quantification of the Arctic sea ice proxy IP25 from marine sediments. Anal. Methods 4, 705. https://doi.org/10.1039/c2ay05728j

Belt, S.T., Brown, T.A., Smik, L., Tatarek, A., Wiktor, J., Stowasser, G., Assmy, P., Allen, C.S., Husum, K., 2017. Identification of C25 highly branched isoprenoid (HBI) alkenes in diatoms of the genus Rhizosolenia in polar and sub-polar marine phytoplankton. Org. Geochem. 110, 65–72. https://doi.org/10.1016/J.ORGGEOCHEM.2017.05.007

Belt, S.T., Cabedo-Sanz, P., Smik, L., Navarro-Rodriguez, A., Berben, S.M.P., Knies, J., Husum, K., 2015. Identification of paleo Arctic winter sea ice limits and the marginal ice zone: Optimised biomarker-based reconstructions of late Quaternary Arctic sea ice. Earth Planet. Sci. Lett. 431, 127–139. https://doi.org/10.1016/J.EPSL.2015.09.020

Belt, S.T., Massé, G., Rowland, S.J., Poulin, M., Michel, C., LeBlanc, B., 2007. A novel chemical fossil of palaeo sea ice: IP25. Org. Geochem. 38, 16–27. https://doi.org/10.1016/J.ORGGEOCHEM.2006.09.013

Belt, S.T., Müller, J., 2013. The Arctic sea ice biomarker IP25: a review of current understanding, recommendations for future research and applications in palaeo sea ice reconstructions. Quat. Sci. Rev. 79, 9–25. https://doi.org/10.1016/j.quascirev.2012.12.001

Berben, S.M.P., Husum, K., Navarro-Rodriguez, A., Belt, S.T., Aagaard-Sørensen, S., 2017. Semi-quantitative reconstruction of early to late Holocene spring and summer sea ice conditions in the northern Barents Sea. J. Quat. Sci. 32, 587–603. https://doi.org/10.1002/jqs.2953

Bereiter, B., Eggleston, S., Schmitt, J., Nehrbass-Ahles, C., Stocker, T.F., Fischer, H., Kipfstuhl, S., Chappellaz, J., 2015. Revision of the EPICA Dome C CO_2 record from 800 to 600 kyr before present. Geophys. Res. Lett. 42, 542–549. https://doi.org/10.1002/2014GL061957

1163 Boiteau, R., Greaves, M., Elderfield, H., 2012. Authigenic uranium in foraminiferal coatings: A proxy
1164 for ocean redox chemistry. Paleoceanography 27, PA3227.
1165 https://doi.org/10.1029/2012PA002335

1166 Boyer, T.P., Antonov, J.I., Baranova, O.K., Coleman, C., Garcia, H.E., Grodsky, A., Johnson, D.R.,
1167 Locarnini, R., Mishonov, A. V, O’Brien, T.D., Paver, C.R., Reagan, J.R., Seidov, D., Smolyar, I.
1168 V, Zweng, M.M., Sullivan, K.D., 2013. WORLD OCEAN DATABASE 2013, NOAA Atlas
1169 NESDIS 72. Sydney Levitus, Ed.; Alexey Mishonoc, Tech. Ed. NOAA Atlas, 209 pp.
1170 https://doi.org/10.7289/V5NZ85MT

1171 Boyle, E.A., 1983. Manganese carbonate overgrowths on foraminifera tests. Geochim. Cosmochim.
1172 Acta 47, 1815–1819. https://doi.org/10.1016/0016-7037(83)90029-7

1173 Boyle, E.A., Keigwin, L.D., 1985. Comparison of Atlantic and Pacific paleochemical records for the
1174 last 215,000 years: changes in deep ocean circulation and chemical inventories. Earth Planet.
1175 Sci. Lett. 76, 135–150. https://doi.org/10.1016/0012-821X(85)90154-2

1176 Brady, H.B., 1884. Report on the Foraminifera dredged by H.M.S. Challenger during the Years 1873-
1177 1876. Rep. Sci. Results Voyag. H.M.S. Chall. Dur. years 1873–76. Zool. 9 (part 22, 1–814.

1178 Brady, H.B., 1881. Notes on some of the Reticularian Rhizopoda of the “Challenger” Expedition. Part
1179 III. Q. J. Microsc. Sci. 21, 31–71.

1180 Brennan, C.E., Meissner, K.J., Eby, M., Hillaire-Marcel, C., Weaver, A.J., 2013. Impact of sea ice
1181 variability on the oxygen isotope content of seawater under glacial and interglacial conditions.
1182 Paleoceanography 28, 388–400. https://doi.org/10.1002/palo.20036

1183 Brown, T.A., Belt, S.T., Tatarek, A., Mundy, C.J., 2014. Source identification of the Arctic sea ice
1184 proxy IP25. Nat. Commun. 5, 4197. https://doi.org/10.1038/ncomms5197

1185 Brown, Z.W., Arrigo, K.R., 2013. Sea ice impacts on spring bloom dynamics and net primary
1186 production in the Eastern Bering Sea. J. Geophys. Res. Ocean. 118, 43–62.
1187 https://doi.org/10.1029/2012JC008034

1188 Brown, Z.W., van Dijken, G.L., Arrigo, K.R., 2011. A reassessment of primary production and
1189 environmental change in the Bering Sea. J. Geophys. Res. 116, C08014.
1190 https://doi.org/10.1029/2010JC006766

1191 Brunelle, B.G., Sigman, D.M., Cook, M.S., Keigwin, L.D., Haug, G.H., Plessen, B., Schettler, G.,
1192 Jaccard, S.L., 2007. Evidence from diatom-bound nitrogen isotopes for subarctic Pacific
1193 stratification during the last ice age and a link to North Pacific denitrification changes.
1194 Paleoceanography 22, n/a-n/a. https://doi.org/10.1029/2005PA001205

1195 Brunelle, B.G., Sigman, D.M., Jaccard, S.L., Keigwin, L.D., Plessen, B., Schettler, G., Cook, M.S.,
1196 Haug, G.H., 2010. Glacial/interglacial changes in nutrient supply and stratification in the
1197 western subarctic North Pacific since the penultimate glacial maximum. Quat. Sci. Rev. 29,
1198 2579–2590. https://doi.org/10.1016/J.QUASCIREV.2010.03.010

1199 Buizert, C., Gkinis, V., Severinghaus, J.P., He, F., Lecavalier, B.S., Kindler, P., Leuenberger, M.,
1200 Carlson, A.E., Vinther, B., Masson-Delmotte, V., White, J.W.C., Liu, Z., Otto-Bliesner, B.,
1201 Brook, E.J., 2014. Greenland temperature response to climate forcing during the last
1202 deglaciation. Science (80-.). 345, 1177–1180. https://doi.org/10.1126/science.1254961

1203 Cabedo-Sanz, P., Belt, S.T., 2015. Identification and characterisation of a novel mono-unsaturated
1204 highly branched isoprenoid (HBI) alkene in ancient Arctic sediments. Org. Geochem. 81, 34–39.
1205 https://doi.org/10.1016/J.ORGGEOCHEM.2015.01.009

1206 Caissie, B.E., Brigham-Grette, J., Lawrence, K.T., Herbert, T.D., Cook, M.S., 2010. Last Glacial
1207 Maximum to Holocene sea surface conditions at Umnak Plateau, Bering Sea, as inferred from
1208 diatom, alkenone, and stable isotope records. Paleoceanography 25.

https://doi.org/10.1029/2008PA001671

Cannariato, K.G., Kennett, J.P., 1999. Climatically related millennial-scale fluctuations in strength of California margin oxygen-minimum zone during the past 60 k.y., Geology. GeoScienceWorld. https://doi.org/10.1130/0091-7613(1999)027<0975:CRMSFI>2.3.CO;2

Caralp, M.H., 1989. Abundance of Bulimina exilis and Melonis barleeanum: Relationship to the quality of marine organic matter. Geo-Marine Lett. 9, 37–43. https://doi.org/10.1007/BF02262816

Caulle, C., Koho, K.A., Mojtahid, M., Reichart, G.J., Jorissen, F.J., 2014. Live (Rose Bengal stained) foraminiferal faunas from the northern Arabian Sea: Faunal succession within and below the OMZ. Biogeosciences 11, 1155–1175. https://doi.org/10.5194/bg-11-1155-2014

Cavalieri, D.J., Martin, S., 1994. The contribution of Alaskan, Siberian, and Canadian coastal polynyas to the cold halocline layer of the Arctic Ocean. J. Geophys. Res. 99, 18343. https://doi.org/10.1029/94JC01169

Chen, P., Yu, J., Jin, Z., 2017. An evaluation of benthic foraminiferal U/Ca and U/Mn proxies for deep ocean carbonate chemistry and redox conditions. Geochemistry, Geophys. Geosystems 18, 617–630. https://doi.org/10.1002/2016GC006730

Chikamoto, M.O., Menviel, L., Abe-Ouchi, A., Ohgaito, R., Timmermann, A., Okazaki, Y., Oka, A., Mouchet, A., 2012. Variability in North Pacific intermediate and deep water ventilation during Heinrich events in two coupled climate models. Deep Sea Res. Part II Top. Stud. Oceanogr. 61–64, 114–126. https://doi.org/10.1016/J.DSR2.2011.12.002

Coachman, L.K., 1993. On the flow field in the Chirikov Basin. Cont. Shelf Res. 13, 481–508. https://doi.org/10.1016/0278-4343(93)90092-C

Coachman, L.K., Whitledge, T.E., Goering, J.J., 1999. Silica in Bering Sea Deep and Bottom Water, Dynamics o. ed. University of Alaska Sea Grant, Faribanks.

Cook, M.S., Keigwin, L.D., 2015. Radiocarbon profiles of the NW Pacific from the LGM and deglaciation: Evaluating ventilation metrics and the effect of uncertain surface reservoir ages. Paleoceanography 30, 174–195. https://doi.org/10.1002/2014PA002649

Cook, M.S., Keigwin, L.D., Sancetta, C.A., 2005. The deglacial history of surface and intermediate water of the Bering Sea. Deep Sea Res. Part II Top. Stud. Oceanogr. 52, 2163–2173. https://doi.org/10.1016/J.DSR2.2005.07.004

Cook, M.S., Ravelo, A.C., Mix, A., Nesbitt, I.M., Miller, N. V., 2016. Tracing subarctic Pacific water masses with benthic foraminiferal stable isotopes during the LGM and late Pleistocene. Deep Sea Res. Part II Top. Stud. Oceanogr. 125–126, 84–95. https://doi.org/10.1016/J.DSR2.2016.02.006

Crusius, J., Pedersen, T.F., Kienast, S., Keigwin, L., Labeyrie, L., 2004. Influence of northwest Pacific productivity on North Pacific Intermediate Water oxygen concentrations during the Bølling-Ållerød interval (14.7-12.9 ka). Geology 32, 633–636. https://doi.org/10.1130/G20508.1

Cushman, J.A., 1933. New Arctic Foraminifera collected by Capt. R. A. Bartlett from Fox Basin and off the northeast coast of Greenland (with two plates). Smithson. Misc. Collect. 89, 1–8.

Cushman, J.A., 1927. An outline of a re-classification of the Foraminifera. Contrib. from Cushman Lab. Foraminifer. Res. 3.

D’Orbigny, A., 1839. Foraminifères. Paris.

Dawson, J.W., 1860. Notice of Tertiary fossils from Labrador, Maine, etc., and remarks on the climate of Canada in the newer Pliocene or Pleistocene period. Can. Nat. Geol. Montr. 5, 188–200.

1254 Detlef, H., Belt, S.T., Sosdian, S.M., Smik, L., Lear, C.H., Hall, I.R., Cabedo-Sanz, P., Husum, K.,
1255 Kender, S., 2018. Sea ice dynamics across the Mid-Pleistocene transition in the Bering Sea. Nat.
1256 Commun. 9, 941. https://doi.org/10.1038/s41467-018-02845-5

1257 Detlef, H., Sosdian, S.M., Kender, S., Lear, C.H., Hall, I.R., 2020. Multi-elemental composition of
1258 authigenic carbonates in benthic foraminifera from the eastern Bering Sea continental margin
1259 (International Ocean Discovery Program Site U1343). Geochim. Cosmochim. Acta 268, 1–21.
1260 https://doi.org/10.1016/j.gca.2019.09.025

1261 Duplessy, J.-C., Arnold, M., Bard, E., Juillet-Leclerc, A., Kallel, N., Labeyrie, L., 1989. AMS 14C
1262 Study of Transient Events and of the Ventilation Rate of the Pacific Intermediate Water During
1263 the Last Deglaciation. Radiocarbon 31, 493–502.

1264 Elias, S.A., Short, S.K., Nelson, C.H., Birks, H.H., 1996. Life and times of the Bering land bridge.
1265 Nature 382, 60–63. https://doi.org/10.1038/382060a0

1266 Emile-Geay, J., Cane, M.A., Naik, N., Seager, R., Clement, A.C., Geen, A. van, 2003. Warren
1267 revisited: Atmospheric freshwater fluxes and “Why is no deep water formed in the North
1268 Pacific.” J. Geophys. Res. 108, 3178. https://doi.org/10.1029/2001JC001058

1269 Expedition 323 Scientists, 2010. Bering Sea pealeoceanography: Pliocene-Pleistocene
1270 paleoceanography and climate history of the Bering Sea. IODP Prelim. Rep. 323.
1271 https://doi.org/10.2204/iodp.pr.323.2010

1272 Fetterer, F.K., Meier, W.N., Savoie, M., Windnagel, A.K., 2017. Sea Ice Index, Version 3 | National
1273 Snow and Ice Data Center updated daily.

1274 Filipsson, H.L., Romero, O.E., Stuut, J.-B.W., Donner, B., 2011. Relationships between primary
1275 productivity and bottom-water oxygenation off northwest Africa during the last deglaciation. J.
1276 Quat. Sci. 26, 448–456. https://doi.org/10.1002/jqs.1473

1277 Frey, K.E., Perovich, D.K., Light, B., 2011. The spatial distribution of solar radiation under a melting
1278 Arctic sea ice cover. Geophys. Res. Lett. 38, n/a-n/a. https://doi.org/10.1029/2011GL049421

1279 Froelich, P.N., Klinkhammer, G.P., Bender, M.L., Luedtke, N.A., Heath, G.R., Cullen, D., Dauphin,
1280 P., Hammond, D., Hartman, B., Maynard, V., 1979. Early oxidation of organic matter in pelagic
1281 sediments of the eastern equatorial Atlantic: suboxic diagenesis. Geochim. Cosmochim. Acta 43,
1282 1075–1090. https://doi.org/10.1016/0016-7037(79)90095-4

1283 Fujii, Y., Nakano, T., Usui, N., Matsumoto, S., Tsujino, H., Kamachi, M., 2013. Pathways of the
1284 North Pacific Intermediate Water identified through the tangent linear and adjoint models of an
1285 ocean general circulation model. J. Geophys. Res. Ocean. 118, 2035–2051.
1286 https://doi.org/10.1002/jgrc.20094

1287 Galbraith, E.D., Jaccard, S.L., Pedersen, T.F., Sigman, D.M., Haug, G.H., Cook, M., Southon, J.R.,
1288 Francois, R., 2007. Carbon dioxide release from the North Pacific abyss during the last
1289 deglaciation. Nature 449, 890–893. https://doi.org/10.1038/nature06227

1290 Garcia, H.E., Locarnini, R.A., Boyer, T.P., Antonov, J.I., Baranova, O.K., Zweng, M.M., Reagan,
1291 J.R., Johnson, D.R., 2014. World Ocean Atlas 2013, Volume 3: Dissolved Oxygen, Apparent
1292 Oxygen Utilization, and Oxygen Saturation. NOAA Atlas NESDIS 75.

1293 Gargett, A.E., 1991. Physical processes and the maintenance of nutrient-rich euphotic zones. Limnol.
1294 Oceanogr. 36, 1527–1545. https://doi.org/10.4319/lo.1991.36.8.1527

1295 Gebhardt, H., Sarnthein, M., Grootes, P.M., Kiefer, T., Kuehn, H., Schmieder, F., Röhl, U., 2008.
1296 Paleonutrient and productivity records from the subarctic North Pacific for Pleistocene glacial
1297 terminations I to V. Paleoceanography 23, n/a-n/a. https://doi.org/10.1029/2007PA001513

1298 Gersonde, R., 2012. The expedition of the research vessel “Sonne” to the subpolar North Pacific and

1299 the Bering Sea in 2009 (SO202-INOPEX). Berichte zur Polar- und Meeresforsch. = Reports
1300 polar Mar. Res. 643, 323.

1301 Gong, X., Lembke-Jene, L., Lohmann, G., Knorr, G., Tiedemann, R., Zou, J.J., Shi, X.F., 2019.
1302 Enhanced North Pacific deep-ocean stratification by stronger intermediate water formation
1303 during Heinrich Stadial 1. Nat. Commun. 10, 656. https://doi.org/10.1038/s41467-019-08606-2

1304 Gorbarenko, S.A., Wang, P., Wang, R., Cheng, X., 2010. Orbital and suborbital environmental
1305 changes in the southern Bering Sea during the last 50 kyr. Palaeogeogr. Palaeoclimatol.
1306 Palaeoecol. 286, 97–106. https://doi.org/10.1016/j.palaeo.2009.12.014

1307 Gottschalk, J., Skinner, L.C., Lippold, J., Vogel, H., Frank, N., Jaccard, S.L., Waelbroeck, C., 2016.
1308 Biological and physical controls in the Southern Ocean on past millennial-scale atmospheric
1309 CO_2 changes. Nat. Commun. 7, 11539. https://doi.org/10.1038/ncomms11539

1310 Gray, W.R., Rae, J.W.B., Wills, R.C.J., Shevenell, A.E., Taylor, B., Burke, A., Foster, G.L., Lear,
1311 C.H., 2018. Deglacial upwelling, productivity and CO2 outgassing in the North Pacific Ocean.
1312 Nat. Geosci. 11, 340–344. https://doi.org/10.1038/s41561-018-0108-6

1313 Gray, W.R., Wills, R.C.J., Rae, J.W.B., Burke, A., Ivanovic, R.F., Roberts, W.H.G., Ferreira, D.,
1314 Valdes, P.J., 2020. Wind-Driven Evolution of the North Pacific Subpolar Gyre Over the Last
1315 Deglaciation. Geophys. Res. Lett. 47. https://doi.org/10.1029/2019GL086328

1316 Grebmeier, J.M., Overland, J.E., Moore, S.E., Farley, E. V, Carmack, E.C., Cooper, L.W., Frey, K.E.,
1317 Helle, J.H., McLaughlin, F.A., McNutt, S.L., 2006. A major ecosystem shift in the northern
1318 Bering Sea. Science 311, 1461–4. https://doi.org/10.1126/science.1121365

1319 Greenacre, M., 1983. Theory and Applications of Corresponding Analysis.

1320 Hammer, D.A.T., Ryan, P.D., Hammer, Ø., Harper, D.A.T., 2001. Past: Paleontological Statistics
1321 Software Package for Education and Data Analysis, Palaeontologia Electronica.

1322 Hammer, Ø., Harper, D.A.T., 2006. Paleontological data analysis. Blackwell Pub.

1323 Harada, N., Ahagon, N., Sakamoto, T., Uchida, M., Ikehara, M., Shibata, Y., 2006. Rapid fluctuation
1324 of alkenone temperature in the southwestern Okhotsk Sea during the past 120 ky. Glob. Planet.
1325 Change 53, 29–46. https://doi.org/10.1016/j.gloplacha.2006.01.010

1326 Harada, N., Ahagon, N., Uchida, M., Murayama, M., 2004. Northward and southward migrations of
1327 frontal zones during the past 40 kyr in the Kuroshio-Oyashio transition area. Geochemistry,
1328 Geophys. Geosystems 5, n/a-n/a. https://doi.org/10.1029/2004GC000740

1329 Harada, N., Sato, M., Sakamoto, T., 2008. Freshwater impacts recorded in tetraunsaturated alkenones
1330 and alkenone sea surface temperatures from the Okhotsk Sea across millennial-scale cycles.
1331 Paleoceanography 23, n/a-n/a. https://doi.org/10.1029/2006PA001410

1332 Hasenfratz, A.P., Martínez-García, A., Jaccard, S.L., Vance, D., Wälle, M., Greaves, M., Haug, G.H.,
1333 2017. Determination of the Mg/Mn ratio in foraminiferal coatings: An approach to correct
1334 Mg/Ca temperatures for Mn-rich contaminant phases. Earth Planet. Sci. Lett. 457, 335–347.
1335 https://doi.org/10.1016/J.EPSL.2016.10.004

1336 Hernández-Almeida, I., Boltovskoy, D., Kruglikova, S.B., Cortese, G., 2020. A new radiolarian
1337 transfer function for the Pacific Ocean and application to fossil records: Assessing potential and
1338 limitations for the last glacial-interglacial cycle. Glob. Planet. Change 190, 103186.
1339 https://doi.org/10.1016/j.gloplacha.2020.103186

1340 Horikawa, K., Asahara, Y., Yamamoto, K., Okazaki, Y., 2010. Intermediate water formation in the
1341 Bering Sea during glacial periods: Evidence from neodymium isotope ratios. Geology 38, 435–
1342 438. https://doi.org/10.1130/G30225.1

1343 Hunt, A.S., Corliss, B.H., 1993. Distribution and microhabitats of living (stained) benthic

foraminifera from the Canadian Arctic Archipelago. Mar. Micropaleontol. 20, 321–345. https://doi.org/10.1016/0377-8398(93)90041-U

Hurst, M.P., Aguilar-Islas, A.M., Bruland, K.W., 2010. Iron in the southeastern Bering Sea: Elevated leachable particulate Fe in shelf bottom waters as an important source for surface waters. Cont. Shelf Res. 30, 467–480. https://doi.org/10.1016/J.CSR.2010.01.001

Ikehara, K., Ohkushi, K., Shibahara, A., Hoshiba, M., 2006. Change of bottom water conditions at intermediate depths of the Oyashio region, NW Pacific over the past 20,000 yrs. Glob. Planet. Change 53, 78–91. https://doi.org/10.1016/j.gloplacha.2006.01.011

Ishimura, T., Tsunogai, U., Hasegawa, S., Nakagawa, F., Oi, T., Kitazato, H., Suga, H., Toyofuku, T., 2012. Variation in stable carbon and oxygen isotopes of individual benthic foraminifera: tracers for quantifying the vital effect. Biogeosciences Discuss. 9, 6191–6218. https://doi.org/10.5194/bgd-9-6191-2012

Itaki, T., Kim, S., Rella, S.F., Uchida, M., Tada, R., Khim, B.K., 2012. Millennial-scale variations of late Pleistocene radiolarian assemblages in the Bering Sea related to environments in shallow and deep waters. Deep. Res. Part II Top. Stud. Oceanogr. 61–64, 127–144. https://doi.org/10.1016/j.dsr2.2011.03.002

Ivanova, E. V., Ovsepyan, E.A., Risebrobakken, B., Vetrov, A.A., 2008. DOWNCORE DISTRIBUTION OF LIVING CALCAREOUS FORAMINIFERA AND STABLE ISOTOPES IN THE WESTERN BARENTS SEA. J. Foraminifer. Res. 38, 337–356. https://doi.org/10.2113/gsjfr.38.4.337

Jaccard, S.L., Galbraith, E.D., 2013. Direct ventilation of the North Pacific did not reach the deep ocean during the last deglaciation. Geophys. Res. Lett. 40, 199–203. https://doi.org/10.1029/2012GL054118

Jaccard, S.L., Galbraith, E.D., 2012. Large climate-driven changes of oceanic oxygen concentrations during the last deglaciation. Nat. Geosci. 5, 151–156. https://doi.org/10.1038/ngeo1352

Jaccard, S.L., Galbraith, E.D., Sigman, D.M., Haug, G.H., Francois, R., Pedersen, T.F., Dulski, P., Thierstein, H.R., 2009. Subarctic Pacific evidence for a glacial deepening of the oceanic respired carbon pool. Earth Planet. Sci. Lett. 277, 156–165. https://doi.org/10.1016/J.EPSL.2008.10.017

Jakobsson, M., Pearce, C., Cronin, T.M., Backman, J., Anderson, L.G., Barrientos, N., Björk, G., Coxall, H., de Boer, A., Mayer, L.A., Mörth, C.-M., Nilsson, J., Rattray, J.E., Stranne, C., Semiletov, I., O'Regan, M., 2017. Post-glacial flooding of the Bering Land Bridge dated to 11 cal ka BP based on new geophysical and sediment records. Clim. Past 13, 991–1005. https://doi.org/10.5194/cp-13-991-2017

Jang, K., Huh, Y., Han, Y., 2017. Authigenic Nd isotope record of North Pacific Intermediate Water formation and boundary exchange on the Bering Slope. Quat. Sci. Rev. 156, 150–163. https://doi.org/10.1016/J.QUASCIREV.2016.11.032

Jannink, N.T., Zachariasse, W.J., Van der Zwaan, G.J., 1998. Living (Rose Bengal stained) benthic foraminifera from the Pakistan continental margin (northern Arabian Sea). Deep Sea Res. Part I Oceanogr. Res. Pap. 45, 1483–1513. https://doi.org/10.1016/S0967-0637(98)00027-2

Katsuki, K., Takahashi, K., 2005. Diatoms as paleoenvironmental proxies for seasonal productivity, sea-ice and surface circulation in the Bering Sea during the late Quaternary. Deep Sea Res. Part II Top. Stud. Oceanogr. 52, 2110–2130. https://doi.org/10.1016/J.DSR2.2005.07.001

Kaufman, D.., Ager, T.., Anderson, N.., Anderson, P.., Andrews, J.., Bartlein, P.., Brubaker, L.., Coats, L.., Cwynar, L.., Duvall, M.., Dyke, A.., Edwards, M.., Eisner, W.., Gajewski, K., Geirsdóttir, A., Hu, F.., Jennings, A.., Kaplan, M.., Kerwin, M.., Lozhkin, A.., MacDonald, G.., Miller, G.., Mock, C.., Oswald, W.., Otto-Bliesner, B.., Porinchu, D.., Rühland, K., Smol, J..,

1390 Steig, E.., Wolfe, B.., 2004. Holocene thermal maximum in the western Arctic (0–180°W). Quat.
1391 Sci. Rev. 23, 529–560. https://doi.org/10.1016/J.QUASCIREV.2003.09.007

1392 Keigwin, L.D., 1998. Glacial-age hydrography of the far northwest Pacific Ocean. Paleoceanography
1393 13, 323–339. https://doi.org/10.1029/98PA00874

1394 Kender, S., Aturamu, A., Zalasiewicz, J., Kaminski, M.A., Williams, M., 2019. Benthic foraminifera
1395 indicate Glacial North Pacific Intermediate Water and reduced primary productivity over
1396 Bowers Ridge, Bering Sea, since the Mid-Brunhes Transition. J. Micropalaeontology 38, 177–
1397 187. https://doi.org/10.5194/jm-38-177-2019

1398 Kender, S., Kaminski, M.A., 2017. Modern deep-water agglutinated foraminifera from IODP
1399 Expedition 323, Bering Sea: ecological and taxonomic implications. J. Micropalaeontology
1400 jmpaleo2016-026. https://doi.org/10.1144/jmpaleo2016-026

1401 Kender, S., Ravelo, A.C., Worne, S., Swann, G.E.A., Leng, M.J., Asahi, H., Becker, J., Detlef, H.,
1402 Aiello, I.W., Andreasen, D., Hall, I.R., 2018. Closure of the Bering Strait caused Mid-
1403 Pleistocene Transition cooling. Nat. Commun. 9, 5386. https://doi.org/10.1038/s41467-018-
1404 07828-0

1405 Keul, N., Langer, G., de Nooijer, L.J., Nehrke, G., Reichart, G.-J., Bijma, J., 2013. Incorporation of
1406 uranium in benthic foraminiferal calcite reflects seawater carbonate ion concentration.
1407 Geochemistry, Geophys. Geosystems 14, 102–111. https://doi.org/10.1029/2012GC004330

1408 Khusid, T.A., Basov, I.A., Gorbarenko, S.A., Chekhovskaya, M.P., 2006. Benthic foraminifers in
1409 upper Quaternary sediments of the southern Bering Sea: Distribution and paleoceanographic
1410 interpretations. Stratigr. Geol. Correl. 14, 538–548. https://doi.org/10.1134/S0869593806050066

1411 Kiefer, T., Kienast, M., 2005. Patterns of deglacial warming in the Pacific Ocean: a review with
1412 emphasis on the time interval of Heinrich event 1. Quat. Sci. Rev. 24, 1063–1081.
1413 https://doi.org/10.1016/J.QUASCIREV.2004.02.021

1414 Kim, S., Takahashi, K., Khim, B.-K., Kanematsu, Y., Asahi, H., Ravelo, A.C., 2014. Biogenic opal
1415 production changes during the Mid-Pleistocene Transition in the Bering Sea (IODP Expedition
1416 323 Site U1343). Quat. Res. 81, 151–157. https://doi.org/10.1016/J.YQRES.2013.10.001

1417 Knox, F., McElroy, M.B., 1984. Changes in atmospheric CO_2: Influence of the marine biota at high
1418 latitude. J. Geophys. Res. 89, 4629. https://doi.org/10.1029/JD089iD03p04629

1419 Knudson, K.P., Ravelo, A.C., 2015. North Pacific Intermediate Water circulation enhanced by the
1420 closure of the Bering Strait. Paleoceanography 30, 1287–1304.
1421 https://doi.org/10.1002/2015PA002840

1422 Kohfeld, K.E., Chase, Z., 2011. Controls on deglacial changes in biogenic fluxes in the North Pacific
1423 Ocean. Quat. Sci. Rev. 30, 3350–3363. https://doi.org/10.1016/J.QUASCIREV.2011.08.007

1424 Koho, K.A., de Nooijer, L.J., Fontanier, C., Toyofuku, T., Kazumasa, O., Kitazato, H., Reichart, G.-
1425 J., 2017. Benthic foraminiferal Mn/Ca ratios reflect microhabitat preferences. Biogeosciences
1426 Discuss. 1–22. https://doi.org/10.5194/bg-2016-547

1427 Köseoğlu, D., Belt, S.T., Husum, K., Knies, J., 2018a. An assessment of biomarker-based multivariate
1428 classification methods versus the PIP25 index for paleo Arctic sea ice reconstruction. Org.
1429 Geochem. 125, 82–94. https://doi.org/10.1016/J.ORGGEOCHEM.2018.08.014

1430 Köseoğlu, D., Belt, S.T., Smik, L., Yao, H., Panieri, G., Knies, J., 2018b. Complementary biomarker-
1431 based methods for characterising Arctic sea ice conditions: A case study comparison between
1432 multivariate analysis and the PIP25 index. Geochim. Cosmochim. Acta 222, 406–420.
1433 https://doi.org/10.1016/J.GCA.2017.11.001

1434 Kuehn, H., Lembke-Jene, L., Gersonde, R., Esper, O., Lamy, F., Arz, H., Kuhn, G., Tiedemann, R.,

1435 2014. Laminated sediments in the Bering Sea reveal atmospheric teleconnections to Greenland
1436 climate on millennial to decadal timescales during the last deglaciation. Clim. Past 10, 2215–
1437 2236. https://doi.org/10.5194/cp-10-2215-2014

1438 Kurek, J., Cwynar, L.C., Ager, T.A., Abbott, M.B., Edwards, M.E., 2009. Late Quaternary
1439 paleoclimate of western Alaska inferred from fossil chironomids and its relation to vegetation
1440 histories. Quat. Sci. Rev. 28, 799–811. https://doi.org/10.1016/j.quascirev.2008.12.001

1441 Ladd, C., 2014. Seasonal and interannual variability of the Bering Slope Current. Deep Sea Res. Part
1442 II Top. Stud. Oceanogr. 109, 5–13. https://doi.org/10.1016/J.DSR2.2013.12.005

1443 Ladd, C., Stabeno, P.J., O’Hern, J.E., 2012. Observations of a Pribilof eddy. Deep Sea Res. Part I
1444 Oceanogr. Res. Pap. 66, 67–76. https://doi.org/10.1016/J.DSR.2012.04.003

1445 Lam, P.J., Bishop, J.K.B., 2008. The continental margin is a key source of iron to the HNLC North
1446 Pacific Ocean. Geophys. Res. Lett. 35, L07608. https://doi.org/10.1029/2008GL033294

1447 Lam, P.J., Robinson, L.F., Blusztajn, J., Li, C., Cook, M.S., McManus, J.F., Keigwin, L.D., 2013.
1448 Transient stratification as the cause of the North Pacific productivity spike during deglaciation.
1449 Nat. Geosci. 6, 622–626. https://doi.org/10.1038/ngeo1873

1450 Lea, D.W., Mashiotta, T.A., Spero, H.J., 1999. Controls on magnesium and strontium uptake in
1451 planktonic foraminifera determined by live culturing. Geochim. Cosmochim. Acta 63, 2369–
1452 2379. https://doi.org/10.1016/S0016-7037(99)00197-0

1453 Leblanc, K., Hare, C.E., Boyd, P.W., Bruland, K.W., Sohst, B., Pickmere, S., Lohan, M.C., Buck, K.,
1454 Ellwood, M., Hutchins, D.A., 2005. Fe and Zn effects on the Si cycle and diatom community
1455 structure in two contrasting high and low-silicate HNLC areas. Deep Sea Res. Part I Oceanogr.
1456 Res. Pap. 52, 1842–1864. https://doi.org/10.1016/J.DSR.2005.06.005

1457 Levitus, S., Conkright, M.E., Reid, J.L., Najjar, R.G., Mantyla, A., 1993. Distribution of nitrate,
1458 phosphate and silicate in the world oceans. Prog. Oceanogr. 31, 245–273.
1459 https://doi.org/10.1016/0079-6611(93)90003-V

1460 Lisiecki, L.E., Raymo, M.E., 2005. A Pliocene-Pleistocene stack of 57 globally distributed benthic δ
1461 ^{18}O records. Paleoceanography 20, n/a-n/a. https://doi.org/10.1029/2004PA001071

1462 Lo, L., Belt, S.T., Lattaud, J., Friedrich, T., Zeeden, C., Schouten, S., Smik, L., Timmermann, A.,
1463 Cabedo-Sanz, P., Huang, J.-J., Zhou, L., Ou, T.-H., Chang, Y.-P., Wang, L.-C., Chou, Y.-M.,
1464 Shen, C.-C., Chen, M.-T., Wei, K.-Y., Song, S.-R., Fang, T.-H., Gorbarenko, S.A., Wang, W.-
1465 L., Lee, T.-Q., Elderfield, H., Hodell, D.A., 2018. Precession and atmospheric CO2 modulated
1466 variability of sea ice in the central Okhotsk Sea since 130,000 years ago. Earth Planet. Sci. Lett.
1467 488, 36–45. https://doi.org/10.1016/J.EPSL.2018.02.005

1468 Locarnini, R.A., Mishonov, A.V., Antonov, J.I., Boyer, T.P., Garcia, H.E., Baranova, O.K., Zweng,
1469 M.M., Paver, C.R., Reagan, J.R., Johnson, D.R., Hamilton, M., Seidov, D., 2013. World Ocean
1470 Atlas 2013, Volume 1: Temperature. NOAA Atlas NESDIS 73.

1471 Lund, D.C., Mix, A.C., Southon, J., 2011. Increased ventilation age of the deep northeast Pacific
1472 Ocean during the last deglaciation. Nat. Geosci. 4, 771–774. https://doi.org/10.1038/ngeo1272

1473 Matsumoto, K., Oba, T., Lynch-Stieglitz, J., Yamamoto, H., 2002. Interior hydrography and
1474 circulation of the glacial Pacific Ocean. Quat. Sci. Rev. 21, 1693–1704.
1475 https://doi.org/10.1016/S0277-3791(01)00142-1

1476 Max, L., Lembke-Jene, L., Riethdorf, J.-R., Tiedemann, R., Nürnberg, D., Kühn, H., Mackensen, A.,
1477 2014. Pulses of enhanced North Pacific Intermediate Water ventilation from the Okhotsk Sea
1478 and Bering Sea during the last deglaciation. Clim. Past 10, 591–605. https://doi.org/10.5194/cp-
1479 10-591-2014

1480 Max, L., Riethdorf, J.-R., Tiedemann, R., Smirnova, M., Lembke-Jene, L., Fahl, K., Nürnberg, D.,
1481 Matul, A., Mollenhauer, G., 2012. Sea surface temperature variability and sea-ice extent in the
1482 subarctic northwest Pacific during the past 15,000 years. Paleoceanography 27, n/a-n/a.
1483 https://doi.org/10.1029/2012PA002292

1484 Max, L., Rippert, N., Lembke-Jene, L., Mackensen, A., Nürnberg, D., Tiedemann, R., 2017. Evidence
1485 for enhanced convection of North Pacific Intermediate Water to the low-latitude Pacific under
1486 glacial conditions. Paleoceanography 32, 41–55. https://doi.org/10.1002/2016PA002994

1487 McKay, C.L., Filipsson, H.L., Romero, O.E., Stuut, J.-B.W., Björck, S., 2016. The interplay between
1488 the surface and bottom water environment within the Benguela Upwelling System over the last
1489 70 ka. Paleoceanography 31, 266–285. https://doi.org/10.1002/2015PA002792

1490 McManus, J.F., Francois, R., Gherardi, J.-M., Keigwin, L.D., Brown-Leger, S., 2004. Collapse and
1491 rapid resumption of Atlantic meridional circulation linked to deglacial climate changes. Nature
1492 428, 834–837. https://doi.org/10.1038/nature02494

1493 Méheust, M., Fahl, K., Stein, R., 2013. Variability in modern sea surface temperature, sea ice and
1494 terrigenous input in the sub-polar North Pacific and Bering Sea: Reconstruction from biomarker
1495 data. Org. Geochem. 57, 54–64. https://doi.org/10.1016/J.ORGGEOCHEM.2013.01.008

1496 Méheust, M., Stein, R., Fahl, K., Gersonde, R., 2018. Sea-ice variability in the subarctic North Pacific
1497 and adjacent Bering Sea during the past 25 ka: new insights from IP25 and Uk′37 proxy records.
1498 arktos 4, 8. https://doi.org/10.1007/s41063-018-0043-1

1499 Méheust, M., Stein, R., Fahl, K., Max, L., Riethdorf, J.-R., 2016. High-resolution IP25-based
1500 reconstruction of sea-ice variability in the western North Pacific and Bering Sea during the past
1501 18,000 years. Geo-Marine Lett. 36, 101–111. https://doi.org/10.1007/s00367-015-0432-4

1502 Menviel, L., Timmermann, A., Elison Timm, O., Mouchet, A., Abe-Ouchi, A., Chikamoto, M.O.,
1503 Harada, N., Ohgaito, R., Okazaki, Y., 2012. Removing the North Pacific halocline: Effects on
1504 global climate, ocean circulation and the carbon cycle. Deep Sea Res. Part II Top. Stud.
1505 Oceanogr. 61–64, 106–113. https://doi.org/10.1016/J.DSR2.2011.03.005

1506 Meyer, V.D., Max, L., Hefter, J., Tiedemann, R., Mollenhauer, G., 2016. Glacial-to-Holocene
1507 evolution of sea surface temperature and surface circulation in the subarctic northwest Pacific
1508 and the Western Bering Sea. Paleoceanography 31, 916–927.
1509 https://doi.org/10.1002/2015PA002877

1510 Miura, T., Suga, T., Hanawa, K., 2002. Winter Mixed Layer and Formation of Dichothermal Water in
1511 the Bering Sea. J. Oceanogr. 58, 815–823. https://doi.org/10.1023/A:1022871112946

1512 Mizobata, K., Saitoh, S., 2004. Variability of Bering Sea eddies and primary productivity along the
1513 shelf edge during 1998–2000 using satellite multisensor remote sensing. J. Mar. Syst. 50, 101–
1514 111. https://doi.org/10.1016/J.JMARSYS.2003.09.014

1515 Mizobata, K., Saitoh, S., Wang, J., 2008. Interannual variability of summer biochemical enhancement
1516 in relation to mesoscale eddies at the shelf break in the vicinity of the Pribilof Islands, Bering
1517 Sea. Deep Sea Res. Part II Top. Stud. Oceanogr. 55, 1717–1728.
1518 https://doi.org/10.1016/J.DSR2.2008.03.002

1519 Mizobata, K., Saitoh, S.I., Shiomoto, A., Miyamura, T., Shiga, N., Imai, K., Toratani, M., Kajiwara,
1520 Y., Sasaoka, K., 2002. Bering Sea cyclonic and anticyclonic eddies observed during summer
1521 2000 and 2001. Prog. Oceanogr. 55, 65–75. https://doi.org/10.1016/S0079-6611(02)00070-8

1522 Moffitt, S.E., Moffitt, R.A., Sauthoff, W., Davis, C. V., Hewett, K., Hill, T.M., 2015.
1523 Paleoceanographic Insights on Recent Oxygen Minimum Zone Expansion: Lessons for Modern
1524 Oceanography. PLoS One 10, e0115246. https://doi.org/10.1371/journal.pone.0115246

1525 Moore, J.K., Doney, S.C., Glover, D.M., Fung, I.Y., 2001. Iron cycling and nutrient-limitation

patterns in surface waters of the World Ocean. Deep Sea Res. Part II Top. Stud. Oceanogr. 49, 463–507. https://doi.org/10.1016/S0967-0645(01)00109-6

Mudelsee, M., 2003. Estimating Pearson’s Correlation Coefficient with Bootstrap Confidence Interval from Serially Dependent Time Series. Math. Geol. 35, 651–665. https://doi.org/10.1023/B:MATG.0000002982.52104.02

Müller, J., Massé, G., Stein, R., Belt, S.T., 2009. Variability of sea-ice conditions in the Fram Strait over the past 30,000 years. Nat. Geosci. 2, 772–776. https://doi.org/10.1038/ngeo665

Müller, J., Wagner, A., Fahl, K., Stein, R., Prange, M., Lohmann, G., 2011. Towards quantitative sea ice reconstructions in the northern North Atlantic: A combined biomarker and numerical modelling approach. Earth Planet. Sci. Lett. 306, 137–148. https://doi.org/10.1016/J.EPSL.2011.04.011

Nagashima, K., Tada, R., Matsui, H., Irino, T., Tani, A., Toyoda, S., 2007. Orbital- and millennial-scale variations in Asian dust transport path to the Japan Sea. Palaeogeogr. Palaeoclimatol. Palaeoecol. 247, 144–161. https://doi.org/10.1016/j.palaeo.2006.11.027

Navarro-Rodriguez, A., Belt, S.T., Knies, J., Brown, T.A., 2013. Mapping recent sea ice conditions in the Barents Sea using the proxy biomarker IP25: implications for palaeo sea ice reconstructions. Quat. Sci. Rev. 79, 26–39. https://doi.org/10.1016/J.QUASCIREV.2012.11.025

Niebauer, H.J., Alexander, V., Henrichs, S., 1990. Physical and biological oceanographic interaction in the spring bloom at the Bering Sea marginal ice edge zone. J. Geophys. Res. 95, 22229. https://doi.org/10.1029/JC095iC12p22229

Niebauer, H.J., Alexander, V., Henrichs, S.M., 1995. A time-series study of the spring bloom at the Bering Sea ice edge I. Physical processes, chlorophyll and nutrient chemistry. Cont. Shelf Res. 15, 1859–1877. https://doi.org/10.1016/0278-4343(94)00097-7

Niebauer, H.J., Bond, N.A., Yakunin, L.P., Plotnikov, V.V., 1999. An Update on the Climatology and Sea Ice of the Bering Sea, Dynamics o. ed. Alaskan Sea Grant College Report No. AK-SG-99-03.

Nürnberg, D., Bijma, J., Hemleben, C., 1996. Assessing the reliability of magnesium in foraminiferal calcite as a proxy for water mass temperatures. Geochim. Cosmochim. Acta 60, 803–814. https://doi.org/10.1016/0016-7037(95)00446-7

Ohkouchi, N., Kawahata, H., Murayama, M., Okada, M., Nakamura, T., Taira, A., 1994. Was deep water formed in the North Pacific during the Late Quaternary? Cadmium evidence from the Northwest Pacific. Earth Planet. Sci. Lett. 124, 185–194. https://doi.org/10.1016/0012-821X(94)00082-4

Ohkushi, K., Kennett, J.P., Zeleski, C.M., Moffitt, S.E., Hill, T.M., Robert, C., Beaufort, L., Behl, R.J., 2013. Quantified intermediate water oxygenation history of the NE Pacific: A new benthic foraminiferal record from Santa Barbara basin. Paleoceanography 28, 453–467. https://doi.org/10.1002/palo.20043

Okazaki, Y., Sagawa, T., Asahi, H., Horikawa, K., Onodera, J., 2012. Ventilation changes in the western North Pacific since the last glacial period. Clim. Past 8, 17–24. https://doi.org/10.5194/cp-8-17-2012

Okazaki, Y., Takahashi, K., Asahi, H., Katsuki, K., Hori, J., Yasuda, H., Sagawa, Y., Tokuyama, H., 2005. Productivity changes in the Bering Sea during the late Quaternary. Deep Sea Res. Part II Top. Stud. Oceanogr. 52, 2150–2162. https://doi.org/10.1016/J.DSR2.2005.07.003

Okazaki, Y., Timmermann, A., Menviel, L., Harada, N., Abe-Ouchi, A., Chikamoto, M.O., Mouchet, A., Asahi, H., 2010. Deepwater formation in the North Pacific during the Last Glacial Termination. Science 329, 200–4. https://doi.org/10.1126/science.1190612

1572 Oksman, M., Juggins, S., Miettinen, A., Witkowski, A., Weckström, K., 2019. The biogeography and
1573 ecology of common diatom species in the northern North Atlantic, and their implications for
1574 paleoceanographic reconstructions. Mar. Micropaleontol. 148, 1–28.
1575 https://doi.org/10.1016/J.MARMICRO.2019.02.002

1576 Okumura, Y.M., Deser, C., Hu, A., Timmermann, A., Xie, S.-P., Okumura, Y.M., Deser, C., Hu, A.,
1577 Timmermann, A., Xie, S.-P., 2009. North Pacific Climate Response to Freshwater Forcing in the
1578 Subarctic North Atlantic: Oceanic and Atmospheric Pathways. J. Clim. 22, 1424–1445.
1579 https://doi.org/10.1175/2008JCLI2511.1

1580 Ovsepyan, E.A., Ivanova, E.V., Lembke-Jene, L., Max, L., Tiedemann, R., Nürnberg, D., 2017.
1581 Penultimate and last glacial oceanographic variations in the Bering Sea on millennial timescales:
1582 Links to North Atlantic climate. Quat. Sci. Rev. 163, 135–151.
1583 https://doi.org/10.1016/J.QUASCIREV.2017.03.012

1584 Pedersen, T.F., Price, N.B., 1982. The geochemistry of manganese carbonate in Panama Basin
1585 sediments. Geochim. Cosmochim. Acta 46, 59–68. https://doi.org/10.1016/0016-
1586 7037(82)90290-3

1587 Pelto, B.M., Caissie, B.E., Petsch, S.T., Brigham-Grette, J., 2018. Oceanographic and Climatic
1588 Change in the Bering Sea, Last Glacial Maximum to Holocene. Paleoceanogr. Paleoclimatology
1589 33, 93–111. https://doi.org/10.1002/2017PA003265

1590 Pena, L.D., Calvo, E., Cacho, I., Eggins, S., Pelejero, C., 2005. Identification and removal of Mn-Mg-
1591 rich contaminant phases on foraminiferal tests: Implications for Mg/Ca past temperature
1592 reconstructions. Geochemistry, Geophys. Geosystems 6, Q09P02.
1593 https://doi.org/10.1029/2005GC000930

1594 Perovich, D.K., 2016. Sea ice and sunlight, in: Sea Ice. John Wiley & Sons, Ltd, Chichester, UK, pp.
1595 110–137. https://doi.org/10.1002/9781118778371.ch4

1596 Piña-Ochoa, E., Høgslund, S., Geslin, E., Cedhagen, T., Revsbech, N.P., Nielsen, L.P., Schweizer,
1597 M., Jorissen, F., Rysgaard, S., Risgaard-Petersen, N., 2010. Widespread occurrence of nitrate
1598 storage and denitrification among Foraminifera and Gromiida. Proc. Natl. Acad. Sci. U. S. A.
1599 107, 1148–1153. https://doi.org/10.1073/pnas.0908440107

1600 Praetorius, S.K., Condron, A., Mix, A.C., Walczak, M.H., McKay, J.L., Du, J., 2020. The role of
1601 Northeast Pacific meltwater events in deglacial climate change. Sci. Adv. 6, eaay2915.
1602 https://doi.org/10.1126/sciadv.aay2915

1603 Praetorius, S.K., Mix, A.C., Walczak, M.H., Wolhowe, M.D., Addison, J.A., Prahl, F.G., 2015. North
1604 Pacific deglacial hypoxic events linked to abrupt ocean warming. Nature 527, 362–366.
1605 https://doi.org/10.1038/nature15753

1606 R Studio Team, 2015. R Studio: Integrated Development for R.

1607 Rae, J.W.B., Sarnthein, M., Foster, G.L., Ridgwell, A., Grootes, P.M., Elliott, T., 2014. Deep water
1608 formation in the North Pacific and deglacial CO2 rise. Paleoceanography 29, 645–667.
1609 https://doi.org/10.1002/2013PA002570

1610 Raitzsch, M., Kuhnert, H., Hathorne, E.C., Groeneveld, J., Bickert, T., 2011. U/Ca in benthic
1611 foraminifers: A proxy for the deep-sea carbonate saturation. Geochemistry, Geophys.
1612 Geosystems 12, Q06019. https://doi.org/10.1029/2010GC003344

1613 Rasmussen, S.O., Andersen, K.K., Svensson, A.M., Steffensen, J.P., Vinther, B.M., Clausen, H.B.,
1614 Siggaard-Andersen, M.-L., Johnsen, S.J., Larsen, L.B., Dahl-Jensen, D., Bigler, M.,
1615 Röthlisberger, R., Fischer, H., Goto-Azuma, K., Hansson, M.E., Ruth, U., 2006. A new
1616 Greenland ice core chronology for the last glacial termination. J. Geophys. Res. 111, D06102.
1617 https://doi.org/10.1029/2005JD006079

Rella, S.F., Tada, R., Nagashima, K., Ikehara, M., Itaki, T., Ohkushi, K., Sakamoto, T., Harada, N., Uchida, M., 2012. Abrupt changes of intermediate water properties on the northeastern slope of the Bering Sea during the last glacial and deglacial period. Paleoceanography 27, n/a-n/a. https://doi.org/10.1029/2011PA002205

Ren, H., Studer, A.S., Serno, S., Sigman, D.M., Winckler, G., Anderson, R.F., Oleynik, S., Gersonde, R., Haug, G.H., 2015. Glacial-to-interglacial changes in nitrate supply and consumption in the subarctic North Pacific from microfossil-bound N isotopes at two trophic levels. Paleoceanography 30, 1217–1232. https://doi.org/10.1002/2014PA002765

Riethdorf, J.-R., Max, L., Nürnberg, D., Lembke-Jene, L., Tiedemann, R., 2013. Deglacial development of (sub) sea surface temperature and salinity in the subarctic northwest Pacific: Implications for upper-ocean stratification. Paleoceanography 28, 91–104. https://doi.org/10.1002/palo.20014

Riethdorf, J.-R., Thibodeau, B., Ikehara, M., Nürnberg, D., Max, L., Tiedemann, R., Yokoyama, Y., 2016. Surface nitrate utilization in the Bering sea since 180 kA BP: Insight from sedimentary nitrogen isotopes. Deep Sea Res. Part II Top. Stud. Oceanogr. 125–126, 163–176. https://doi.org/10.1016/J.DSR2.2015.03.007

Rodionov, S.N., Bond, N.A., Overland, J.E., 2007. The Aleutian Low, storm tracks, and winter climate variability in the Bering Sea. Deep Sea Res. Part II Top. Stud. Oceanogr. 54, 2560–2577. https://doi.org/10.1016/J.DSR2.2007.08.002

Rosenthal, Y., Boyle, E.A., Slowey, N., 1997. Temperature control on the incorporation of magnesium, strontium, fluorine, and cadmium into benthic foraminiferal shells from Little Bahama Bank: Prospects for thermocline paleoceanography. Geochim. Cosmochim. Acta 61, 3633–3643. https://doi.org/10.1016/S0016-7037(97)00181-6

Russell, A.D., Hönisch, B., Spero, H.J., Lea, D.W., 2004. Effects of seawater carbonate ion concentration and temperature on shell U, Mg, and Sr in cultured planktonic foraminifera. Geochim. Cosmochim. Acta 68, 4347–4361. https://doi.org/10.1016/J.GCA.2004.03.013

Saenko, O.A., Schmittner, A., Weaver, A.J., Saenko, O.A., Schmittner, A., Weaver, A.J., 2004. The Atlantic–Pacific Seesaw. J. Clim. 17, 2033–2038. https://doi.org/10.1175/1520-0442(2004)017<2033:TAS>2.0.CO;2

Sagawa, T., Ikehara, K., 2008. Intermediate water ventilation change in the subarctic northwest Pacific during the last deglaciation. Geophys. Res. Lett. 35, L24702. https://doi.org/10.1029/2008GL035133

Saidova, K.M., 1961. Ecology of foraminifera and paleogeography of the USSR FAr Eastern seas and the Northwestern Pacific: Ekologiya foraminifer i paleogeographyia dalnevostochnih morei SSSR i severo-zapadnoi chasti Tihogo okeana. Nauka 221.

Sarmiento, J.L., Gruber, N., Brzezinski, M.A., Dunne, J.P., 2004. High-latitude controls of thermocline nutrients and low latitude biological productivity. Nature 427, 56–60. https://doi.org/10.1038/nature02127

Sarmiento, J.L., Toggweiler, J.R., Najjar, R., Webb, D.J., Jenkins, W.J., Wunsch, C., Elderfield, H., Whitfield, M., Minster, J.-F., 1988. Ocean Carbon-Cycle Dynamics and Atmospheric pFormula [and Discussion]. Philos. Trans. R. Soc. A Math. Phys. Eng. Sci. 325, 3–21. https://doi.org/10.1098/rsta.1988.0039

Schlitzer, R., 2016. Ocean Data View.

Schlung, S.A., Christina Ravelo, A., Aiello, I.W., Andreasen, D.H., Cook, M.S., Drake, M., Dyez, K.A., Guilderson, T.P., Lariviere, J.P., Stroynowski, Z., Takahashi, K., 2013. Millennial-scale climate change and intermediate water circulation in the Bering Sea from 90 ka: A high-

resolution record from IODP Site U1340. Paleoceanography 28, 54–67. https://doi.org/10.1029/2012PA002365

Schumacher, S., Jorissen, F.J., Dissard, D., Larkin, K.E., Gooday, A.J., 2007. Live (Rose Bengal stained) and dead benthic foraminifera from the oxygen minimum zone of the Pakistan continental margin (Arabian Sea). Mar. Micropaleontol. 62, 45–73. https://doi.org/10.1016/j.marmicro.2006.07.004

Sen Gupta, B.K., Machain-Castillo, M.L., 1993. Benthic foraminifera in oxygen-poor habitats. Mar. Micropaleontol. 20, 183–201. https://doi.org/10.1016/0377-8398(93)90032-S

Setoyama, E., Kaminski, M., 2015. Neogene Benthic Foraminifera from the southern Bering Sea (IODP Expedition 323). Palaeontol. Electron. https://doi.org/10.26879/462

Shakun, J.D., Clark, P.U., He, F., Marcott, S.A., Mix, A.C., Liu, Z., Otto-Bliesner, B., Schmittner, A., Bard, E., 2012. Global warming preceded by increasing carbon dioxide concentrations during the last deglaciation. Nature 484, 49–54. https://doi.org/10.1038/nature10915

Shcherbina, A.Y., Talley, L.D., Rudnick, D.L., 2003. Direct observations of North Pacific ventilation: brine rejection in the Okhotsk Sea. Science 302, 1952–5. https://doi.org/10.1126/science.1088692

Shibahara, A., Ohkushi, K., Kennett, J.P., Ikehara, K., 2007. Late Quaternary changes in intermediate water oxygenation and oxygen minimum zone, northern Japan: A benthic foraminiferal perspective. Paleoceanography 22, n/a-n/a. https://doi.org/10.1029/2005PA001234

Sigman, D.M., Hain, M.P., Haug, G.H., 2010. The polar ocean and glacial cycles in atmospheric CO2 concentration. Nature 466, 47–55. https://doi.org/10.1038/nature09149

Skinner, L.C., Sadekov, A., Brandon, M., Greaves, M., Plancherel, Y., de la Fuente, M., Gottschalk, J., Souanef-Ureta, S., Sevilgen, D.S., Scrivner, A.E., 2019. Rare Earth Elements in early-diagenetic foraminifer ‘coatings’: Pore-water controls and potential palaeoceanographic applications. Geochim. Cosmochim. Acta 245, 118–132. https://doi.org/10.1016/J.GCA.2018.10.027

Smik, L., Cabedo-Sanz, P., Belt, S.T., 2016. Semi-quantitative estimates of paleo Arctic sea ice concentration based on source-specific highly branched isoprenoid alkenes: A further development of the PIP25 index. Org. Geochem. 92, 63–69. https://doi.org/10.1016/J.ORGGEOCHEM.2015.12.007

Smith, W.O., 1987. Phytoplankton dynamics in marginal ice zones, in: Barnes, H., Barnes, M. (Eds.), Oceanography and Marine Biology: An Annual Review Vol. 25. Aberdeen University Press.

Spratt, R.M., Lisiecki, L.E., 2016. A Late Pleistocene sea level stack. Clim. Past 12, 1079–1092. https://doi.org/10.5194/cp-12-1079-2016

Springer, A.M., McRoy, P.C., Flint, M. V., 1996. The Bering Sea Green Belt: shelf-edge processes and ecosystem production. Fish. Oceanogr. 5, 205–223. https://doi.org/10.1111/j.1365-2419.1996.tb00118.x

Stabeno, P.J., Schumacher, J.D., Ohtani, K., 1999. The physical oceanography of the Bering Sea, in: Dynamics of the Bering Sea: A Summary of Physical, Chemical, and Biological Characteristics, and a Synopsis of Research on the Bering Sea. Alaskan Sea Grant College Report No. AK-SG-99-03, pp. 1–28.

Sturchio, N.C., Antonio, M.R., Soderholm, L., Sutton, S.R., Brannon, J.C., 1998. Tetravalent uranium in calcite. Science 281, 971–3. https://doi.org/10.1126/SCIENCE.281.5379.971

Svensson, A., Andersen, K.K., Bigler, M., Clausen, H.B., Dahl-Jensen, D., Davies, S.M., Johnsen, S.J., Muscheler, R., Parrenin, F., Rasmussen, S.O., Röthlisberger, R., Seierstad, I., Steffensen,

J.P., Vinther, B.M., 2008. A 60 000 year Greenland stratigraphic ice core chronology. Clim. Past 4, 47–57. https://doi.org/10.5194/cp-4-47-2008

Tachikawa, K., Elderfield, H., 2002. Microhabitat effects on Cd/Ca and δ13C of benthic foraminifera. Earth Planet. Sci. Lett. 202, 607–624. https://doi.org/10.1016/S0012-821X(02)00796-3

Takahashi, T., Feely, R.A., Weiss, R.F., Wanninkhof, R.H., Chipman, D.W., Sutherland, S.C., Takahashi, T.T., 1997. Global air-sea flux of CO2: An estimate based on measurements of sea-air pCO2 difference. Proc. Natl. Acad. Sci. 94, 8292–8299.

Takahashi, T., Sutherland, S.C., Wanninkhof, R., Sweeney, C., Feely, R.A., Chipman, D.W., Hales, B., Friederich, G., Chavez, F., Sabine, C., Watson, A., Bakker, D.C.E., Schuster, U., Yoshikawa-Inoue, H., Ishii, M., Midorikawa, T., Nojiri, Y., Körtzinger, A., Steinhoff, T., Hoppema, M., Olafsson, J., Arnarson, T.S., Johannessen, T., Olsen, A., Bellerby, R., Wong, C.S., Delille, B., Bates, N.R., de Baar, H.J.W., 2009. Climatological mean and decadal change in surface ocean pCO2, and net sea–air CO2 flux over the global oceans. Deep Sea Res. Part II Top. Stud. Oceanogr. 56, 554–577. https://doi.org/10.1016/J.DSR2.2008.12.009

Talley, L.D., 1993. Distribution and Formation of North Pacific Intermediate Water. J. Phys. Oceanogr. 23, 517–537. https://doi.org/10.1175/1520-0485(1993)023<0517:DAFONP>2.0.CO;2

Talley, L.D., Talley, L.D., 1985. Ventilation of the Subtropical North Pacific: The Shallow Salinity Minimum. J. Phys. Oceanogr. 15, 633–649. https://doi.org/10.1175/1520-0485(1985)015<0633:VOTSNP>2.0.CO;2

Tanaka, S., Takahashi, K., 2005. Late Quaternary paleoceanographic changes in the Bering Sea and the western subarctic Pacific based on radiolarian assemblages. Deep Sea Res. Part II Top. Stud. Oceanogr. 52, 2131–2149. https://doi.org/10.1016/J.DSR2.2005.07.002

Tanaka, T., Yasuda, I., Kuma, K., Nishioka, J., 2012. Vertical turbulent iron flux sustains the Green Belt along the shelf break in the southeastern Bering Sea. Geophys. Res. Lett. 39, L08603. https://doi.org/10.1029/2012GL051164

Taylor, M.A., Hendy, I.L., Pak, D.K., 2014. Deglacial ocean warming and marine margin retreat of the Cordilleran Ice Sheet in the North Pacific Ocean. Earth Planet. Sci. Lett. 403, 89–98. https://doi.org/10.1016/j.epsl.2014.06.026

Tetard, M., Licari, L., Beaufort, L., 2017. Oxygen history off Baja California over the last 80 kyr: A new foraminiferal-based record. Paleoceanography 32, 246–264. https://doi.org/10.1002/2016PA003034

The PALE Beringian Working Group, 1999. Paleoenvironmental Atlas of Beringia Presented in Electronic Form. Quat. Res. 52, 270–271. https://doi.org/10.1006/qres.1999.2073

Toggweiler, J.R., 1999. Variation of atmospheric CO_2 by ventilation of the ocean’s deepest water. Paleoceanography 14, 571–588. https://doi.org/10.1029/1999PA900033

Vare, L.L., Massé, G., Gregory, T.R., Smart, C.W., Belt, S.T., 2009. Sea ice variations in the central Canadian Arctic Archipelago during the Holocene. Quat. Sci. Rev. 28, 1354–1366. https://doi.org/10.1016/j.quascirev.2009.01.013

Viau, A.E., Gajewski, K., Sawada, M.C., Bunbury, J., 2008. Low- and high-frequency climate variability in eastern Beringia during the past 25 000 years. Can. J. Earth Sci. 45, 1435–1453. https://doi.org/10.1139/E08-036

Vinther, B.M., Clausen, H.B., Johnsen, S.J., Rasmussen, S.O., Andersen, K.K., Buchardt, S.L., Dahl-Jensen, D., Seierstad, I.K., Siggaard-Andersen, M.-L., Steffensen, J.P., Svensson, A., Olsen, J., Heinemeier, J., 2006. A synchronized dating of three Greenland ice cores throughout the Holocene. J. Geophys. Res. 111, D13102. https://doi.org/10.1029/2005JD006921

1755 Volkman, J.K., 1986. A review of sterol markers for marine and terrigenous organic matter. Org.
1756 Geochem. 9, 83–99. https://doi.org/10.1016/0146-6380(86)90089-6

1757 Volkman, J.K., Barrett, S.M., Blackburn, S.I., Mansour, M.P., Sikes, E.L., Gelin, F., 1998. Microalgal
1758 biomarkers: A review of recent research developments. Org. Geochem. 29, 1163–1179.
1759 https://doi.org/10.1016/S0146-6380(98)00062-X

1760 Volkmanm, J.K., 2006. Lipid Markers for Marine Organic Matter, in: Volkman, J.K. (Ed.), Marine
1761 Organic Matter: Biomarkers, Isotopes and DNA. Springer Berlin Heidelberg, Berlin,
1762 Heidelberg.

1763 Wang, S., Bailey, D., Lindsay, K., Moore, J.K., Holland, M., 2014. Impact of sea ice on the marine
1764 iron cycle and phytoplankton productivity. Biogeosciences 11, 4713–4731.
1765 https://doi.org/10.5194/bg-11-4713-2014

1766 Warner, M.J., Roden, G.I., 1995. Chlorofluorocarbon evidence for recent ventilation of the deep
1767 Bering Sea. Nature 373, 409–412. https://doi.org/10.1038/373409a0

1768 Warren, B.A., 1983. Why is no deep water formed in the North Pacific? J. Mar. Res. 41, 327–347.
1769 https://doi.org/10.1357/002224083788520207

1770 Weber, T., Cram, J.A., Leung, S.W., DeVries, T., Deutsch, C., 2016. Deep ocean nutrients imply
1771 large latitudinal variation in particle transfer efficiency. Proc. Natl. Acad. Sci. U. S. A. 113,
1772 8606–11. https://doi.org/10.1073/pnas.1604414113

1773 Whitledge, T.E., Luchin, V.A., 1999. Summary of Chemical Distributions and Dynamics in the
1774 Bering Sea, in: Loughlin, T.R., Othani, K. (Eds.), Dynamics of the Bering Sea. University of
1775 Alaska Sea Grant.

1776 Worne, S., Kender, S., Swann, G.E.A., Leng, M.J., Ravelo, A.C., 2019. Coupled climate and subarctic
1777 Pacific nutrient upwelling over the last 850,000 years. Earth Planet. Sci. Lett. 522, 87–97.
1778 https://doi.org/10.1016/j.epsl.2019.06.028

1779 Wu, L., Li, C., Yang, C., Xie, S.P., 2008. Global teleconnections in response to a shutdown of the
1780 Atlantic meridional overturning circulation. J. Clim. 21, 3002–3019.
1781 https://doi.org/10.1175/2007JCLI1858.1

1782 Xiao, X., Zhao, M., Knudsen, K.L., Sha, L., Eiríksson, J., Gudmundsdóttir, E., Jiang, H., Guo, Z.,
1783 2017. Deglacial and Holocene sea–ice variability north of Iceland and response to ocean
1784 circulation changes. Earth Planet. Sci. Lett. 472, 14–24.
1785 https://doi.org/10.1016/J.EPSL.2017.05.006

1786 Zhang, J., Woodgate, R., Moritz, R., 2010. Sea ice response to atmospheric and oceanic forcing in the
1787 bering sea. J. Phys. Oceanogr. 40, 1729–1747. https://doi.org/10.1175/2010JPO4323.1

1788 Zhao, M.-Y., Zheng, Y.-F., Zhao, Y.-Y., 2016. Seeking a geochemical identifier for authigenic
1789 carbonate. Nat. Commun. 7, 10885. https://doi.org/10.1038/ncomms10885

1790 Zheng, Y., van Geen, A., Anderson, R.F., Gardner, J. V., Dean, W.E., 2000. Intensification of the
1791 Northeast Pacific oxygen minimum zone during the Bölling-Alleröd Warm Period.
1792 Paleoceanography 15, 528–536. https://doi.org/10.1029/1999PA000473

1793 Zou, J., Shi, X., Zhu, A., Kandasamy, S., Gong, X., Lembke-Jene, L., Chen, M.-T., Wu, Y., Ge, S.,
1794 Liu, Y., Xue, X., Lohmann, G., Tiedemann, R., 2020. Millennial-scale variations in sedimentary
1795 oxygenation in the western subtropical North Pacific and its links to North Atlantic climate.
1796 Clim. Past 16, 387–407. https://doi.org/10.5194/cp-16-387-2020

1797 Zweng, M.M., Reagan, J.R., Antonov, J.I., Locarnini, R.A., Mishonov, A.V., Boyer, T.P., Garcia,
1798 H.E., Baranova, O.K., Johnson, D.R., Seidov, D., Biddle, M.M., 2013. World Ocean Atlas 2013,
1799 Volume 2: Salinity. NOAA Atlas NESDIS 74.

1800

Table captions

Table 1. Age-depth tie points for the late Quaternary chronology of IODP Site U1343.

Figure captions

Figure 1. Map of the Bering Sea (top) and annual mean oxygen concentrations (Boyer et al., 2013) along a north (A) south (B) transect in the central Bering Sea (bottom) drawn with Ocean Data View (Schlitzer, 2016) (Bathymetry from ‘The GEBCO_2014 Grid, version 20141103, http://www.gebco.net’). IODP Site U1343 is indicated with a red dot, additional core locations discussed in the text are marked with yellow dots. The map shows the surface ocean circulation (dark blue), including the Alaskan Stream, the Aleutian North Slope Current (ANSC), the Bering Slope Current (BSC), and the East Kamchatka Current (EKC). The maximum winter sea ice extent between 1981 and 2010 is indicated as an orange dashed line (Fetterer et al., 2017) and the last glacial maximum (LGM) coastline is shown in purple (The PALE Beringian Working Group, 1999).

Figure 2. Biomarker results from IODP Site U1343. (**A**) MAR_{opal} at Site U1343 (light grey) (Kim et al., 2014); (**B**) Marine sterol biomarkers cholesterol (red) and brassicasterol (orange); (**C**) terrestrial sterol biomarker campesterol (purple) and β-sitosterol (yellow); (**D**) HBI III (green); and (**E**) IP_{25} (dark blue) together with HBI II (light blue circles). Note the break in the HBI III axis. The grey shaded vertical bars indicate the YD, HS1, and HS2.

Figure 3. Semi-quantitative sea ice results. (**A**) Classification tree results (pink) indicating marginal (0-10%), intermediate (10-50%), and extensive (>50%) sea-ice conditions. (**B**) $P_{III}IP_{25}$ (orange) and P_BIP_{25} (yellow), with PIP_{25} values of zero indicating no sea ice and values of one being characteristic of perennial sea-ice conditions. The grey shaded vertical bars indicate the YD, HS1, and HS2.

Figure 4. Results of sedimentary redox chemistry proxies. (**A**) Scores of the benthic foraminiferal assemblage correspondence analysis axis 1 (blue) and 2 (yellow); (**B**) Relative abundance of the benthic foraminifera *Bulimina exilis* (red); (**C**) U/Ca (open circles) of *N. pachyderm*a (orange), *I. norcrossi* (red), and *Uvigerina* spp. (purple). The shaded areas indicate the 2σ envelope. (**D**) U/Mn (open diamonds) of *I. norcrossi* (red) and *Uvigerina* spp. (purple). The shaded areas indicate the 2σ envelope. The grey shaded vertical bars indicate the YD, HS1, and HS2.

Figure 5. A compilation of sea-ice reconstructions discussed in this manuscript. (**A**) IP_{25} concentrations at SO202-18-6 (Méheust et al., 2018); (**B**) The abundance of *A. boreale* plus *A. leptodermum* at PC-23A (Itaki et al., 2012); (**C**) IP_{25} concentrations at SO201-2-114 (Méheust et al., 2016); (**D**) IP_{25} concentrations at U1343 (blue) (this study); (**E**) IP_{25} concentrations at SO201-2-77 (Méheust et al., 2016); (**F**) IP_{25} concentrations at SO201-2-12 (Méheust et al., 2016); (**G**) IP_{25} concentrations at SO202-27-6 (Méheust et al., 2018); (**H**) IP_{25} concentrations at SO202-07-06 (Méheust et al., 2018); (**I**) Northern Hemisphere temperature stack (black) including a 1σ error envelope (Shakun et al., 2012) and Eastern

Beringia (150-180°W) atmospheric temperature stacks from 60-65°N and 65-70°N (light grey) based on pollen records (Viau et al., 2008); (**J**) July insolation at 65°N (black) and NGRIP (light grey) and NEEM (medium grey) $\delta^{18}O$ on the GICC05 time scale (Buizert et al., 2014; Rasmussen et al., 2006; Svensson et al., 2008; Vinther et al., 2006).

Figure 6. A compilation of ventilation and carbon cycle records discussed in this manuscript in combination with regional and global climate records. (**A**) HBI III (green) at Site U1343 (this study); (**B**) IP_{25} (dark blue) together with HBI II (light blue circles) (this study); (**C**) North Pacific pCO_2 at MD01-2416 (Gray et al., 2018); (**D**) Diatom-bound $\delta^{15}N$ at JPC17 (Brunelle et al., 2007); (**E**) Benthic foraminiferal $\delta^{13}C$ at MR06-04-PC23A (medium grey) (Rella et al., 2012), SO201-2-85KL (dark grey), and SO201-2-101KL (light grey) (Max et al., 2014); (**F**) Intermediate water ventilation ages in the Bering Sea and the Sea of Okhotsk (Max et al., 2014); (**G**) Scores of the benthic foraminiferal assemblage correspondence analysis axis 1 (blue) and 2 (yellow) and the relative abundance of the benthic foraminifera *Bulimina exilis* (red) at Site U1343; (**H**) U/Ca of *N. pachyderm*a (orange), *I. norcrossi* (red), and *Uvigerina* spp. (purple) at Site U1343; (**I**) MAR_{opal} at Site U1343 (Kim et al., 2014); (**J**) Benthic foraminiferal $\delta^{18}O$ at IODP Site U1342 (light grey) (Knudson and Ravelo, 2015), Site U1343 (black) (Asahi et al., 2016), and the LR04 stack (grey) (Lisiecki and Raymo, 2005); (**K**) NGRIP $\delta^{18}O$ on the GICC05 time scale (Rasmussen et al., 2006; Svensson et al., 2008; Vinther et al., 2006), and the Northern Hemisphere temperature stack including a 1σ error envelope (Shakun et al., 2012).

Figure 7. Simplified schematic of the deglacial sea-ice dynamics, intermediate water ventilation, and biogeochemical cycling in the eastern Bering Sea. The schematic was produced using features from the IAN symbol library (Courtesy of the Integration and Application Network, University of Maryland Center for Environmental Science (ian.umces.edu/symbols/)). (**A**) The LGM (17.5-24 ka) was characterized by a seasonal sea-cover, reduced upwelling of NPDW, and an expanded GNPIW resulting from enhanced brine rejection. GNPIW, however, did not reach to depth of 2000 m. (**B**) Early HS1 (16.5-17.5 ka) was characterized by an enhanced seasonal sea-ice cover, in response to atmospheric cooling. Increased sea-ice formation lead to enhanced brine rejection and increased GNPIW formation and ventilation compared to the LGM, which in turn caused modest up-mixing of nutrients, as well as a deepening of the mixed layer resulting in light limitation of primary producers. (**C**) The BA (12.8-14.7 ka) is marked by a reduced sea-ice cover due to atmospheric warming, enhanced NPDW upwelling, increased primary productivity, and pronounced mid-depth hypoxia causing the preservation of laminations along the eastern Bering Sea slope.

Table 1.

Depth (m CCSF-A)	Age (ka)	Reference
0.01	7.6	Asahi et al. (2016)
1.07	11.7	Correlation to SO202-18-6/3 and HLY02-02-3JPC (Cook et al., 2005; Kuehn et al., 2014)
2.69	14.5	Correlation to SO202-18-6/3 and HLY02-02-3JPC (Cook et al., 2005; Kuehn et al., 2014)
3.86	17.8	Asahi et al. (2016)
7.71	33.02	Asahi et al. (2016)
11.56	48.2	Asahi et al. (2016)

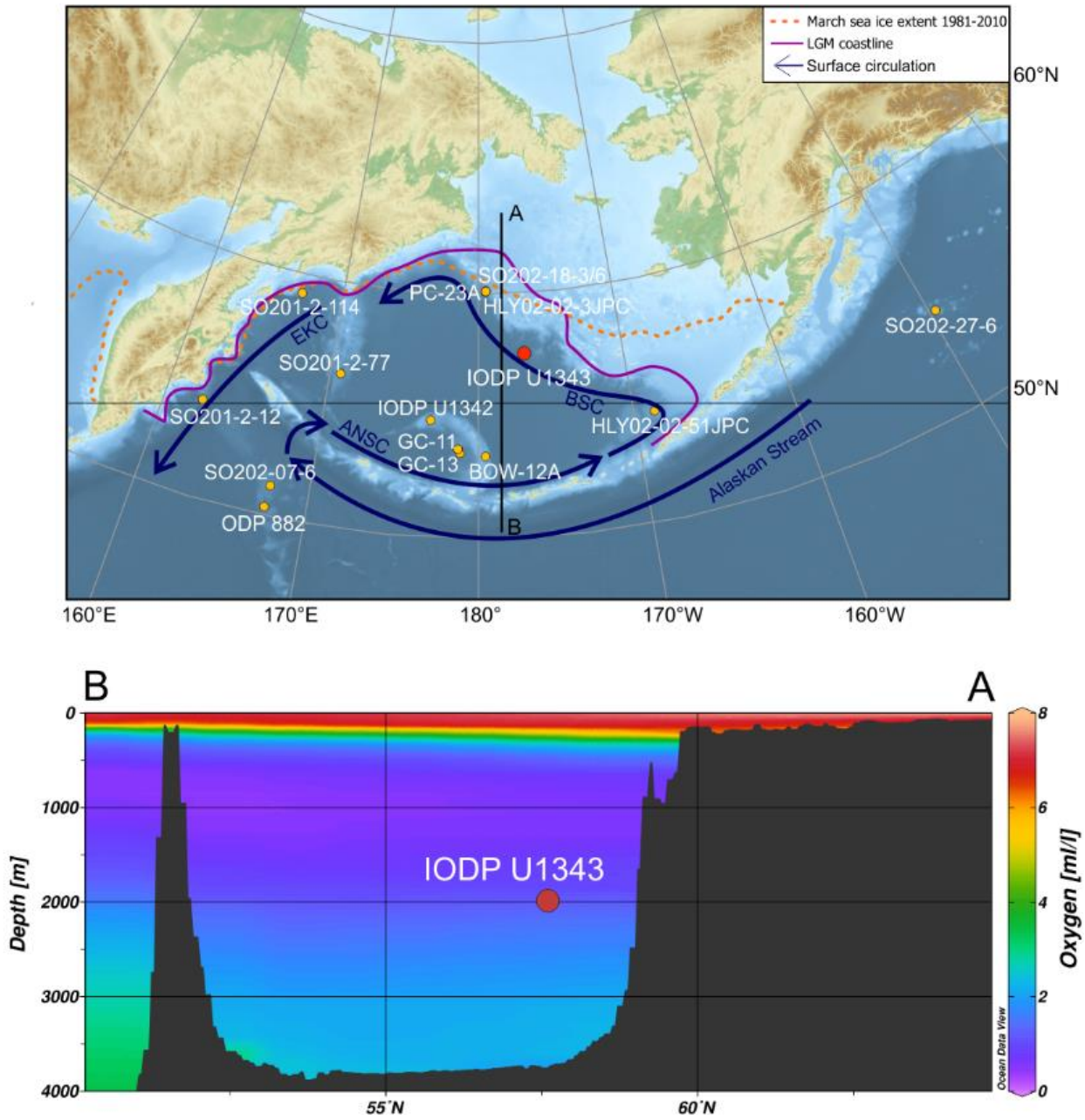

Figure 1.

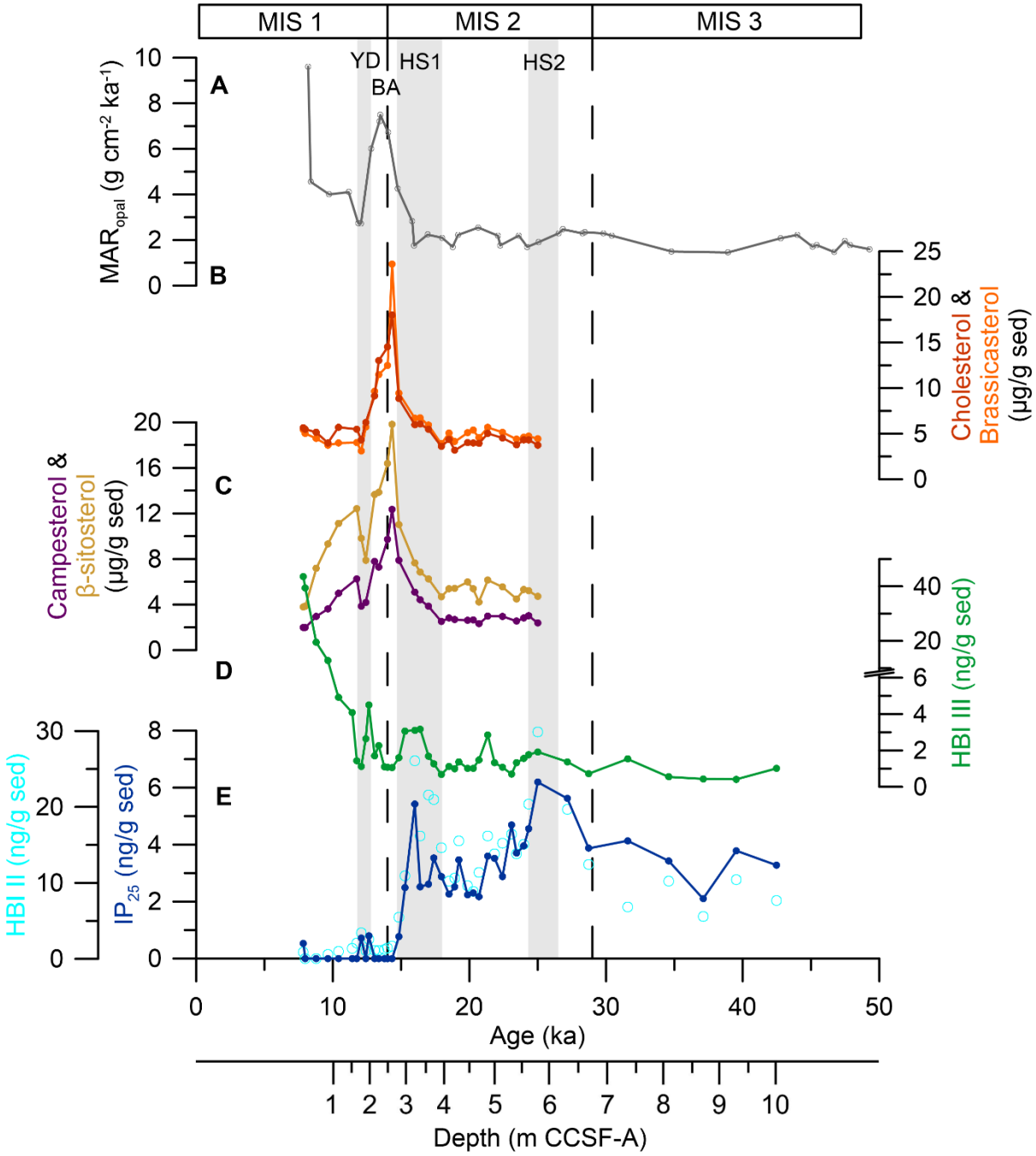

Figure 2.

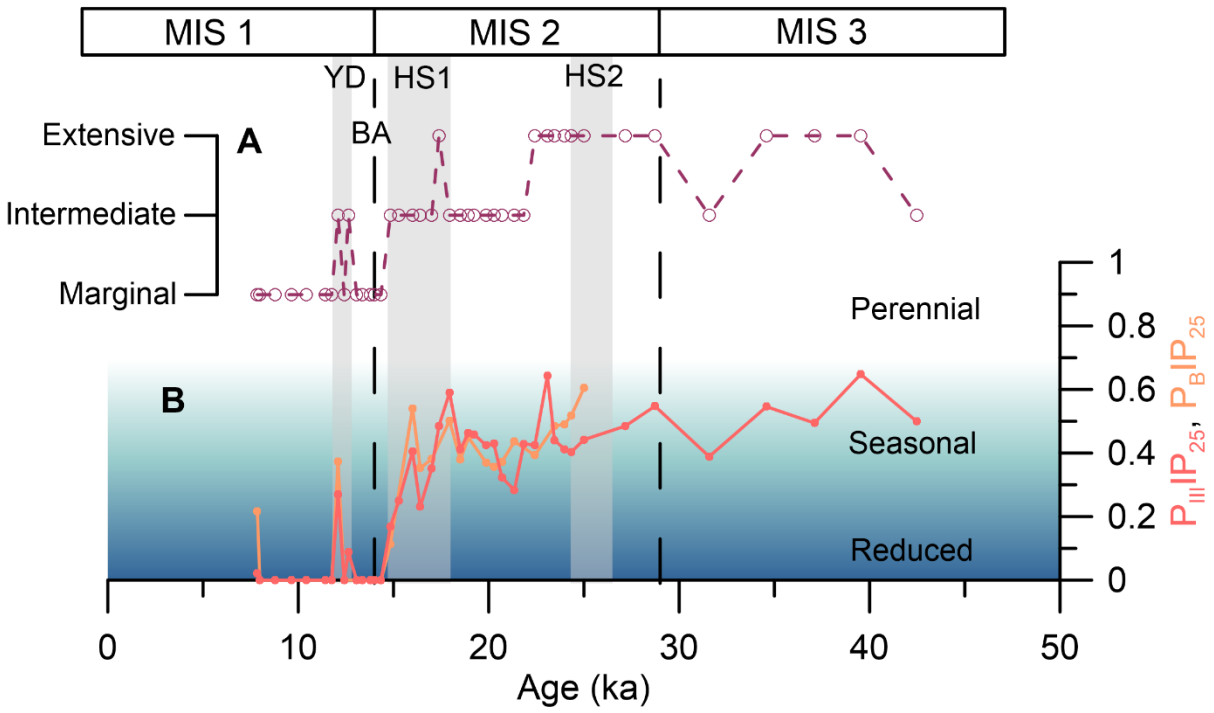

Figure 3.

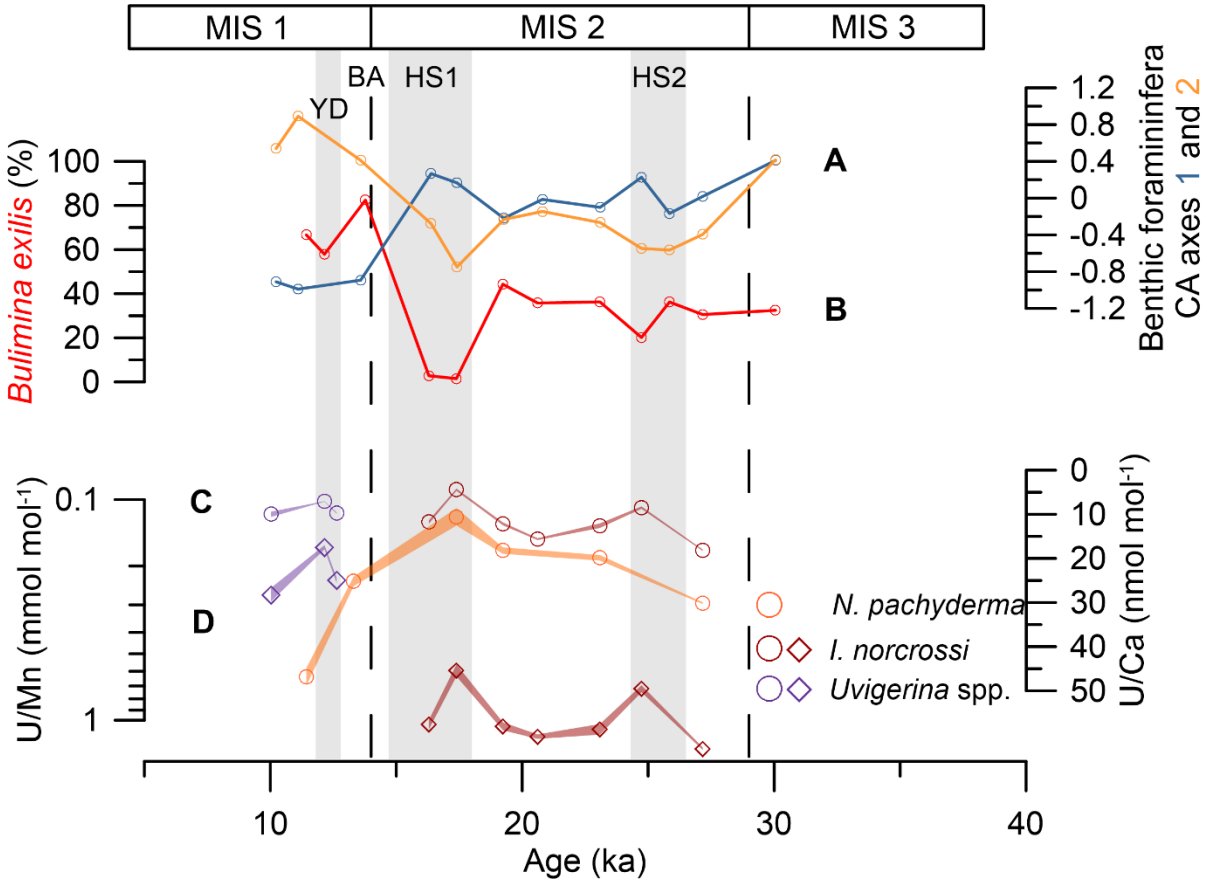

Figure 4.

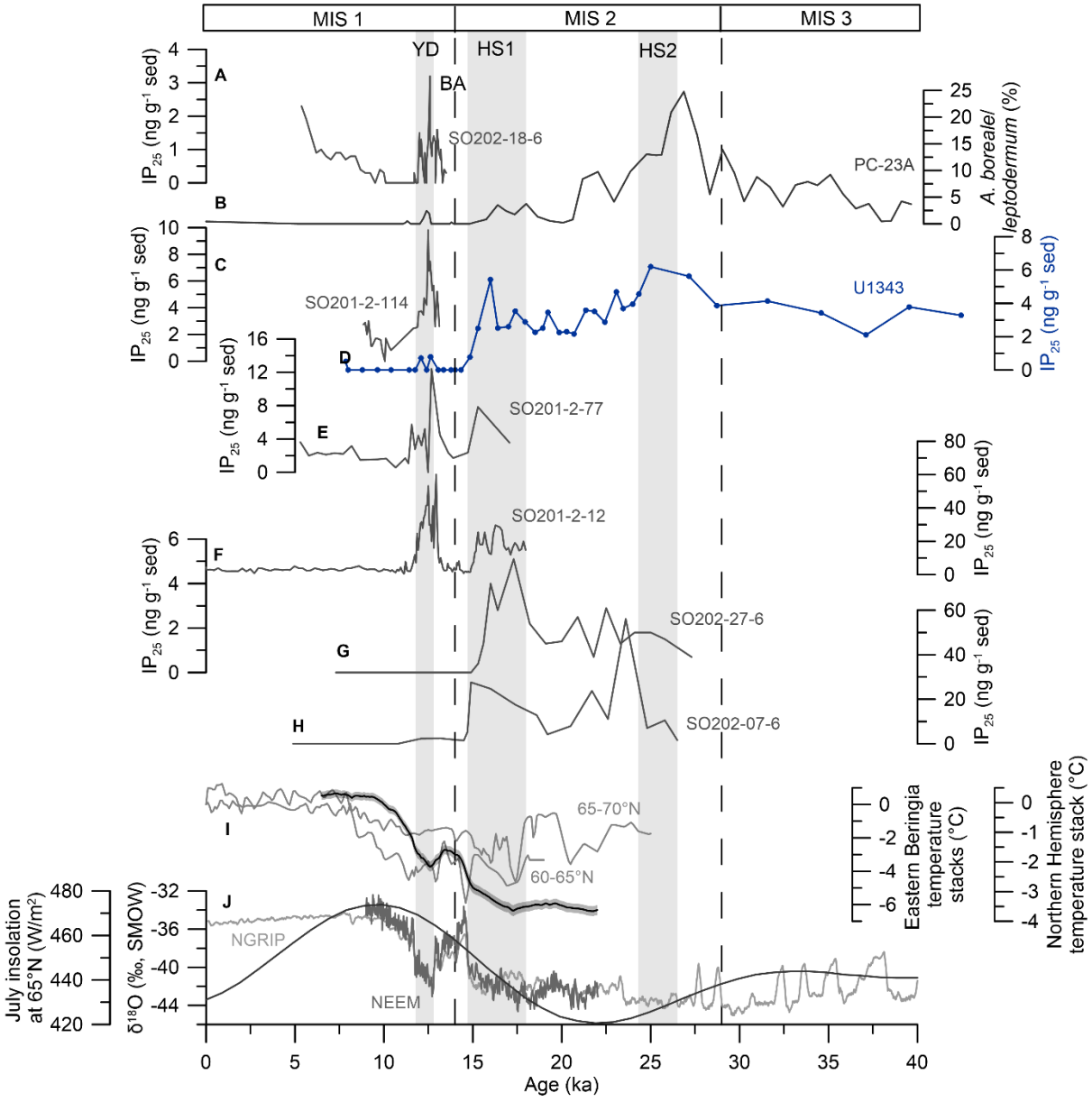

Figure 5.

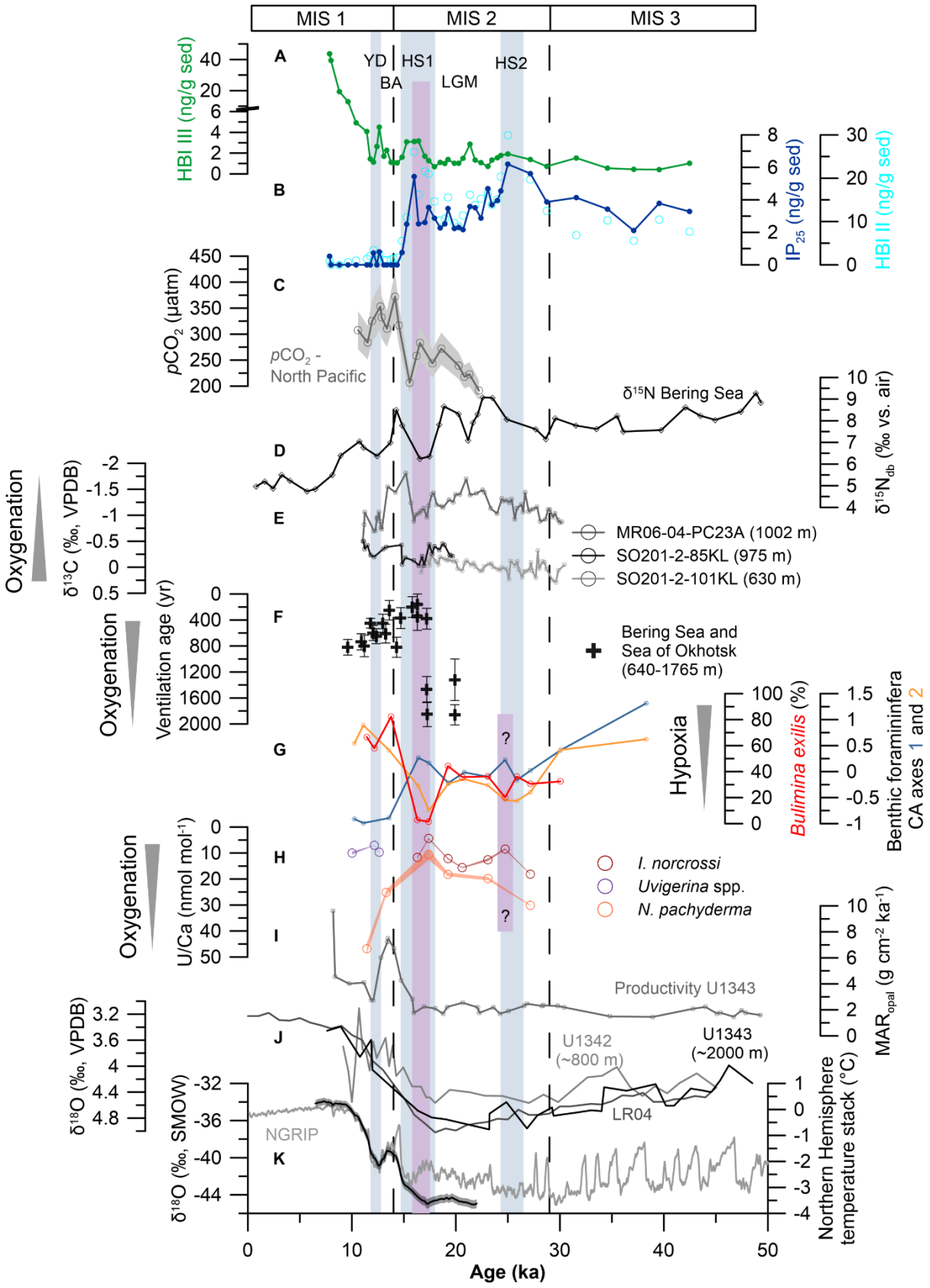

Figure 6.

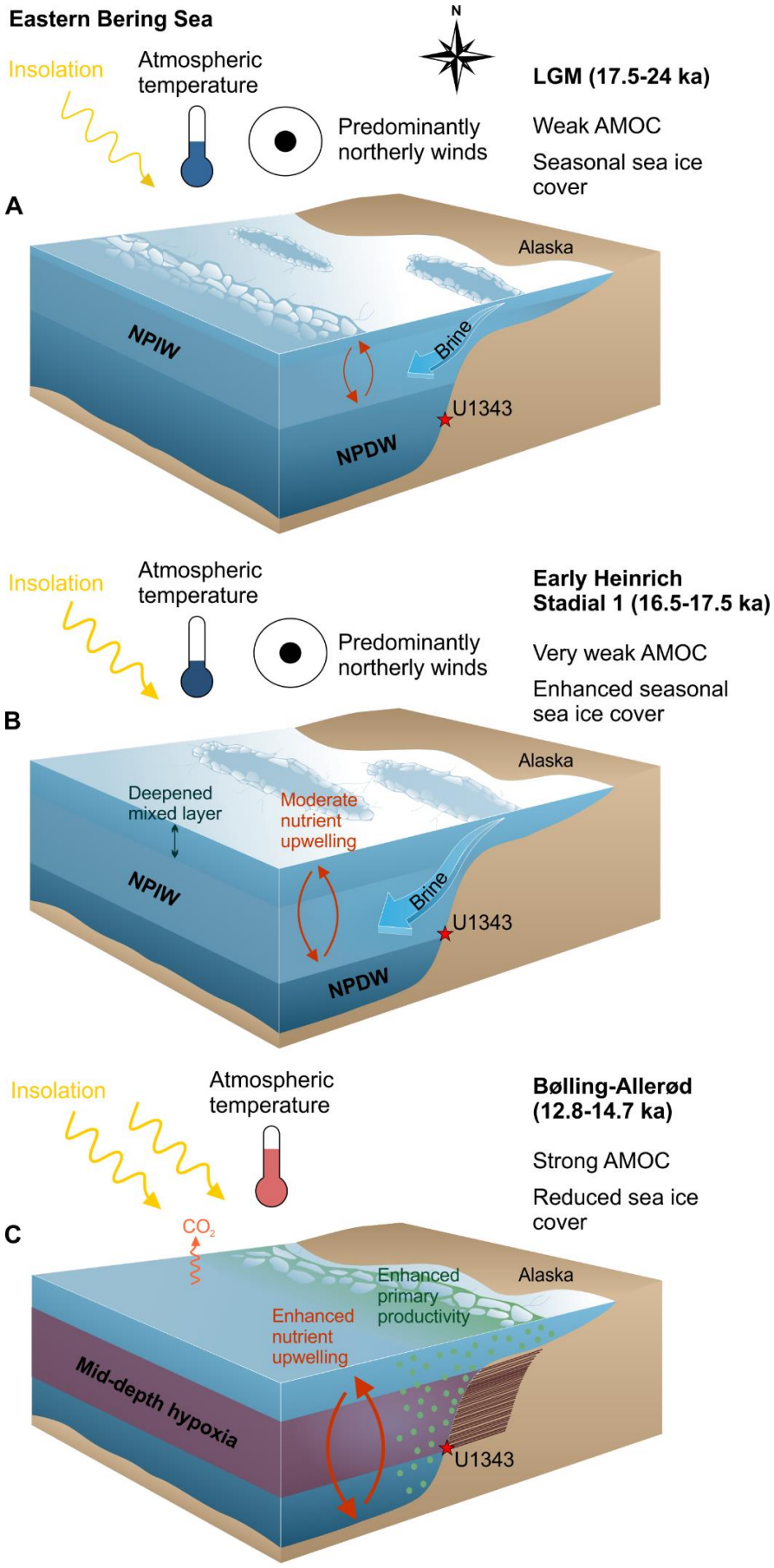

Figure 7.

Supplementary Material: ‘Late Quaternary sea-ice and sedimentary redox conditions in the eastern Bering Sea – implications for ventilation of the mid-depth North Pacific and an Atlantic-Pacific seesaw mechanism’

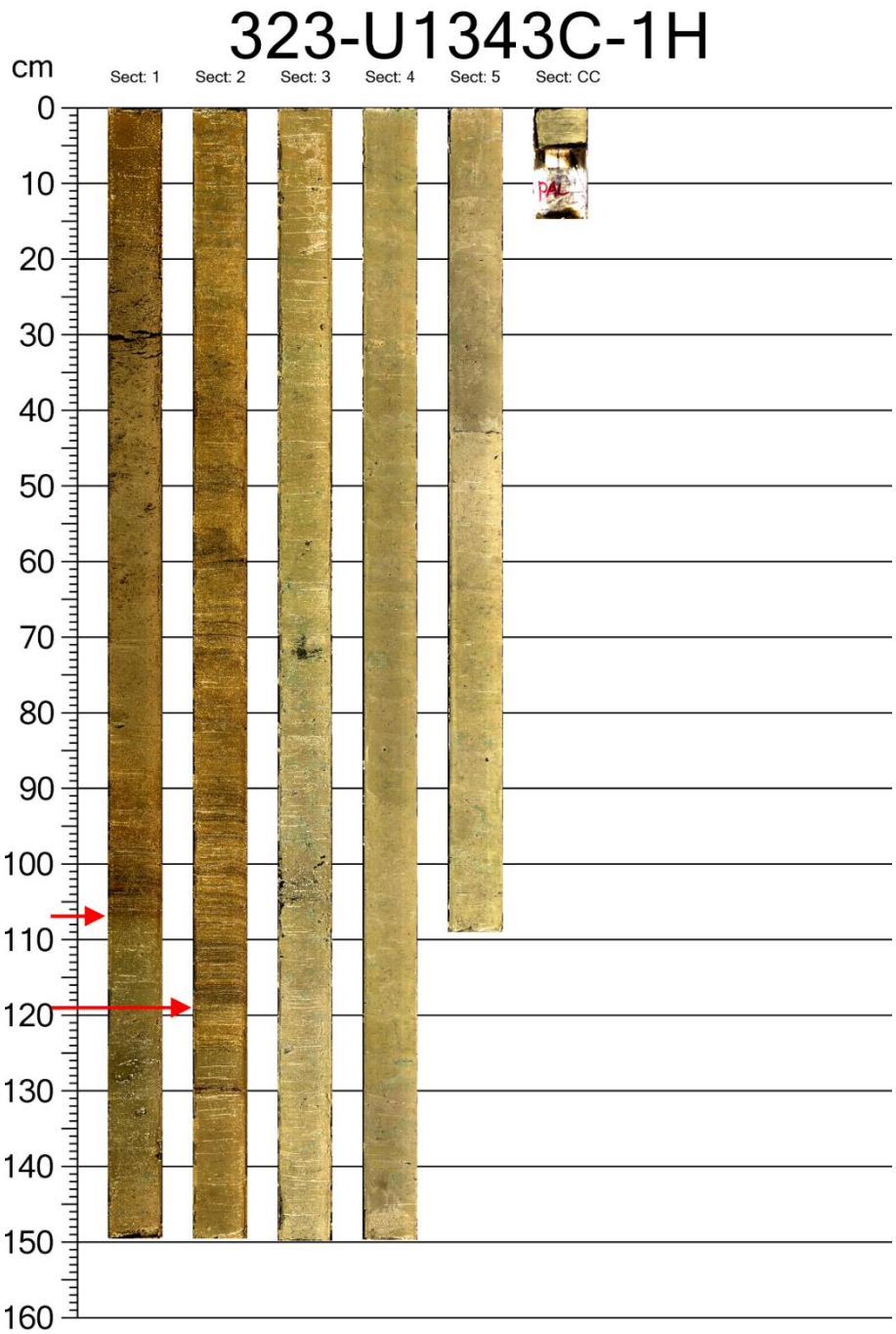

Supplementary Figure 1. Core photo of U1343C-1H from web.iodp.tamu.edu/LORE/, tonal range adjusted to enhance the brightness and contrast. The red arrows indiacte the base of the laminated sediment sections (Expedition 323 Scientists, 2010).

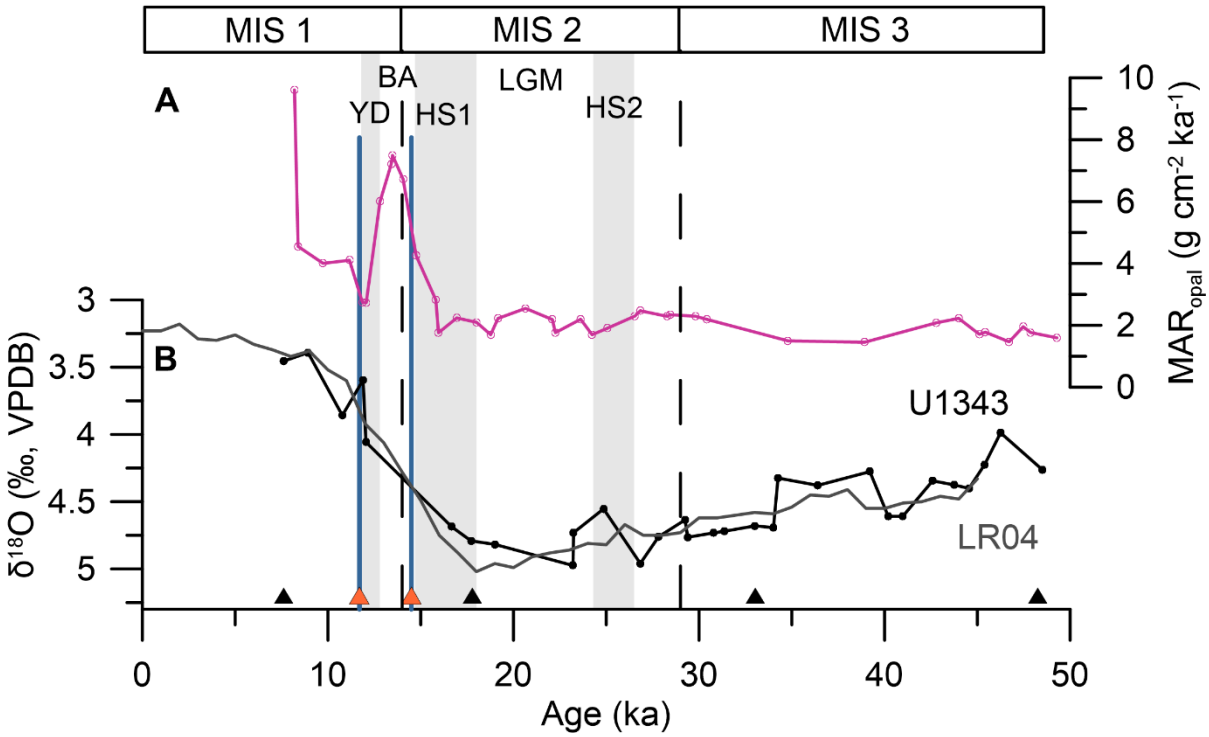

Supplementary Figure 2. (**A**) MAR_{opal} (Kim et al., 2014) (pink) at Site U1343. (**B**) $\delta^{18}O_b$ (black) at Site U1343 (Asahi et al., 2016) together with the LR04 stack (grey) (Lisiecki and Raymo, 2005). The bases of the laminated intervals are marked by blue vertical lines (Expedition 323 Scientists, 2010). The triangles at the bottom represent the age-depth tie points: The black triangles are tie points based on $\delta^{18}O_b$ stratigraphy (Asahi et al., 2016) and the orange triangles represent the age-depth tie point based on the correlation of the onset of the BA and early Holocene sediment laminations at Site U1343 with sites HLY02-02-3JPC (60°07.67’N, 180°33.49’E, 1132 m water depth) and SO202-18-3/6 (60°07.60’N, 179°26.64’W, 1109 m water depth) (Cook et al., 2005; Kuehn et al., 2014).

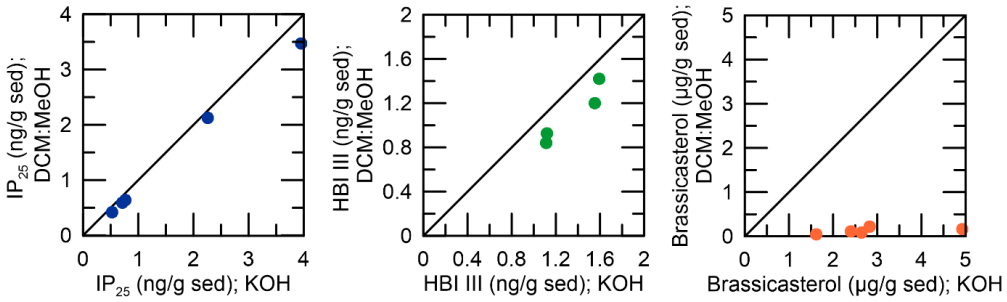

Supplementary Figure 3. Comparison of biomarker results from samples extracted with DCM:Methanol (x-axis) and KOH (y-axis), respectively. Both IP_{25} (blue) and HBI III (green) show only a minor offset between the two methods, while brassicasterol (orange) is significantly higher in samples extracted with KOH.

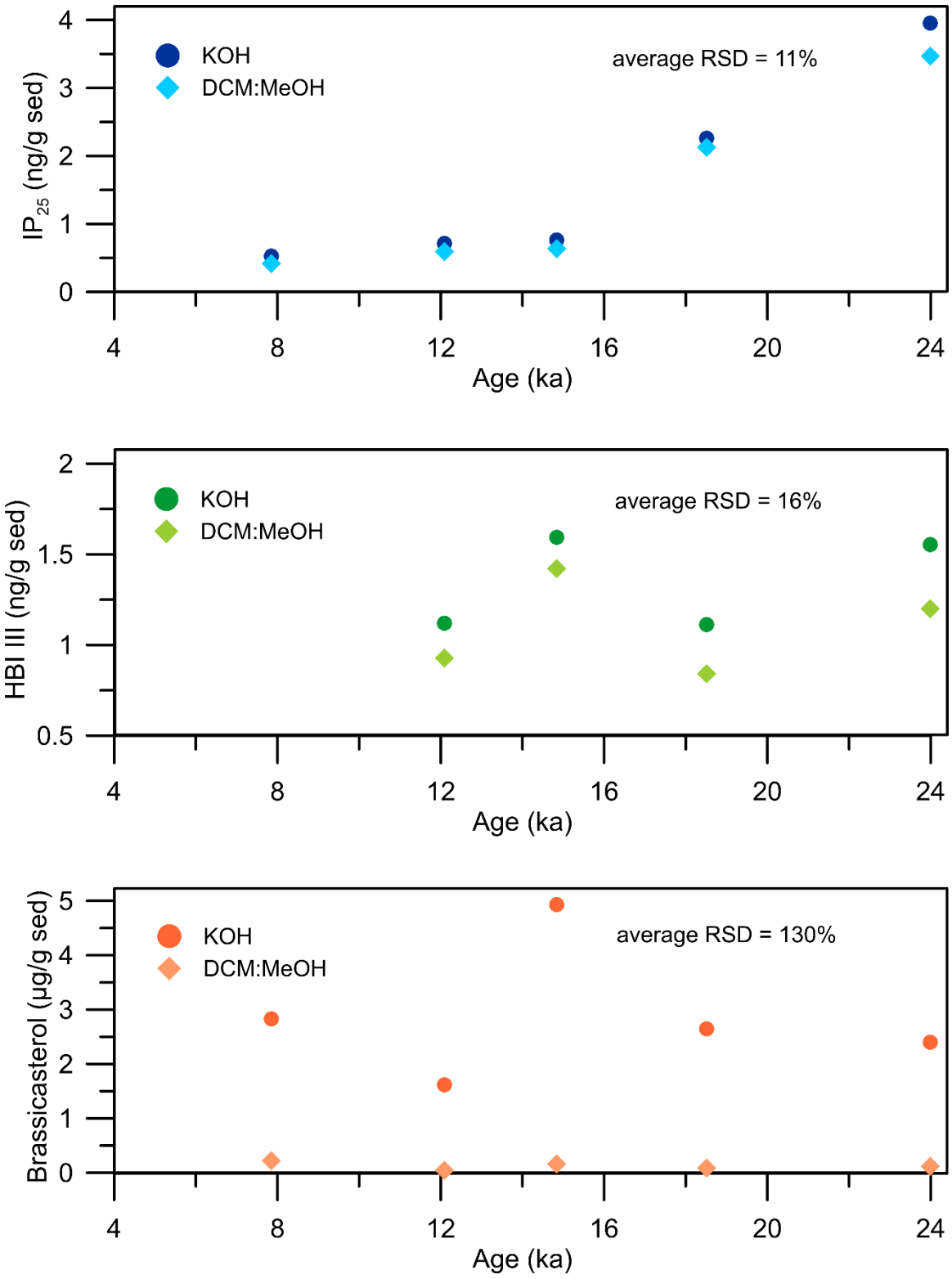

Supplementary Figure 4. Comparison of sea ice biomarkers extracted using DCM:Methanol and KOH against age. The biomarker trends are the same, while there are small offsets between the methods for HBIs (IP_{25} in blue, HBI III in green) and a large offset for brassicasterol (orange).

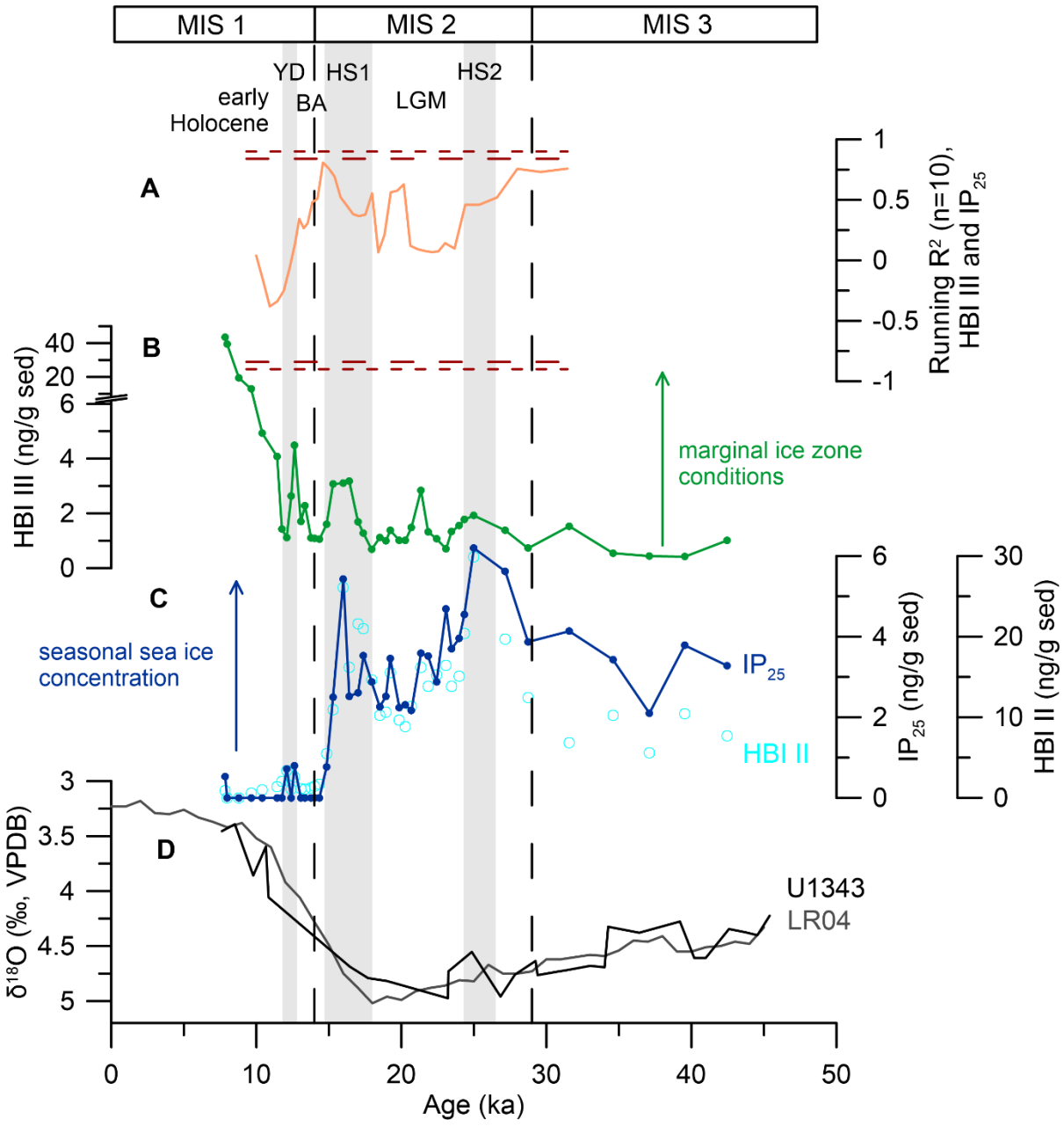

Supplementary Figure 5. (**A**) 10-pt moving window correlation of IP_{25} and HBI III (orange) including the 95% (long red dashed line) and 99% (short red dashed line) confidence interval; (**B**) HBI III (green) at Site U1343; (**C**) IP_{25} (dark blue) and HBI II (light blue circles) at Site U1343; (**D**) $\delta^{18}O_b$ at Site U1343 (black) together with the LR04 stack (grey). The grey shaded areas indicate HS2, HS1, and the YD.

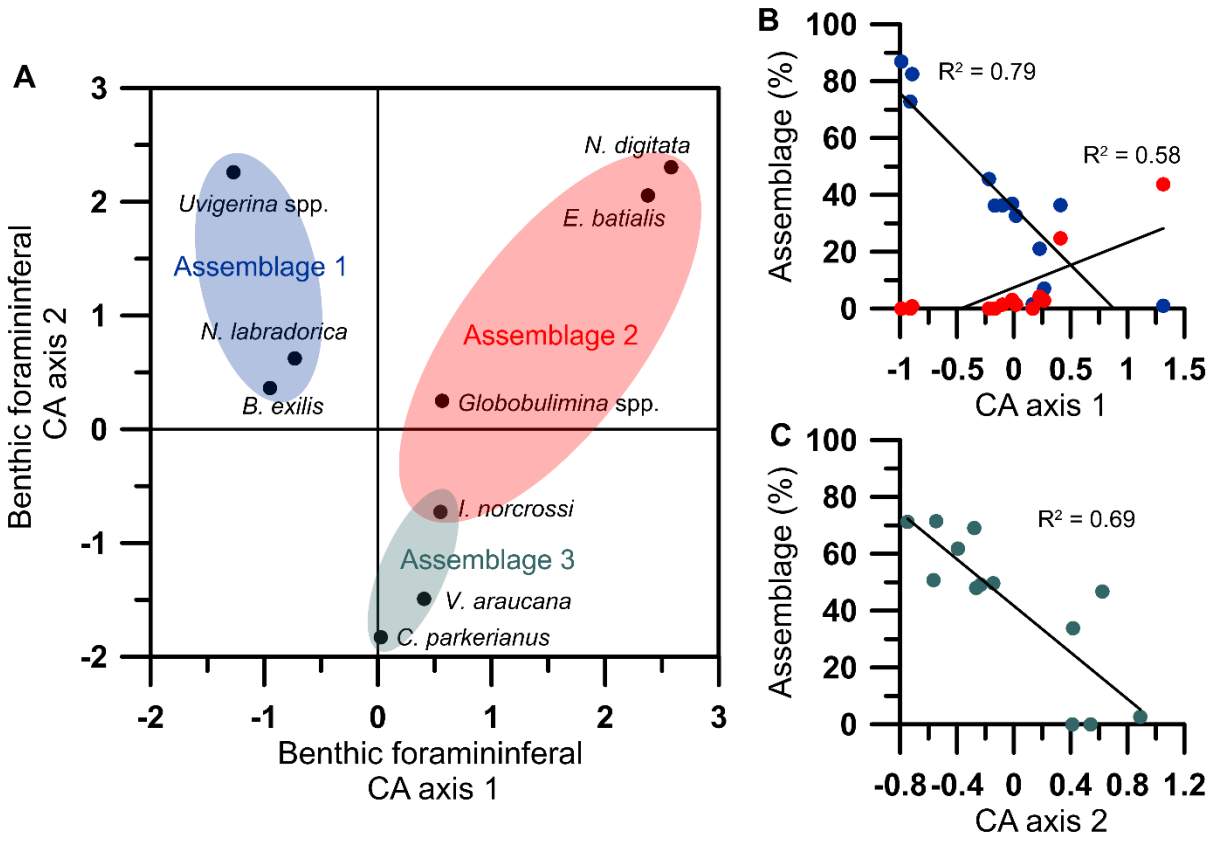

Supplementary Figure 6. (**A**) Correspondence analysis (CA) of the benthic foraminiferal assemblage data from Site U1343 with samples >50 specimens and for species with >10 individuals in total. The ovals indicate the foraminifera species included in Assemblage 1 (blue), 2 (red) and 3 (green). (**B**) CA axis 1 scores against the percentage counts of Assemblage 1 (blue) and assemblage 2 (red). (**C**) CA axis 2 scores against the percentage counts of Assemblage 3 (green).

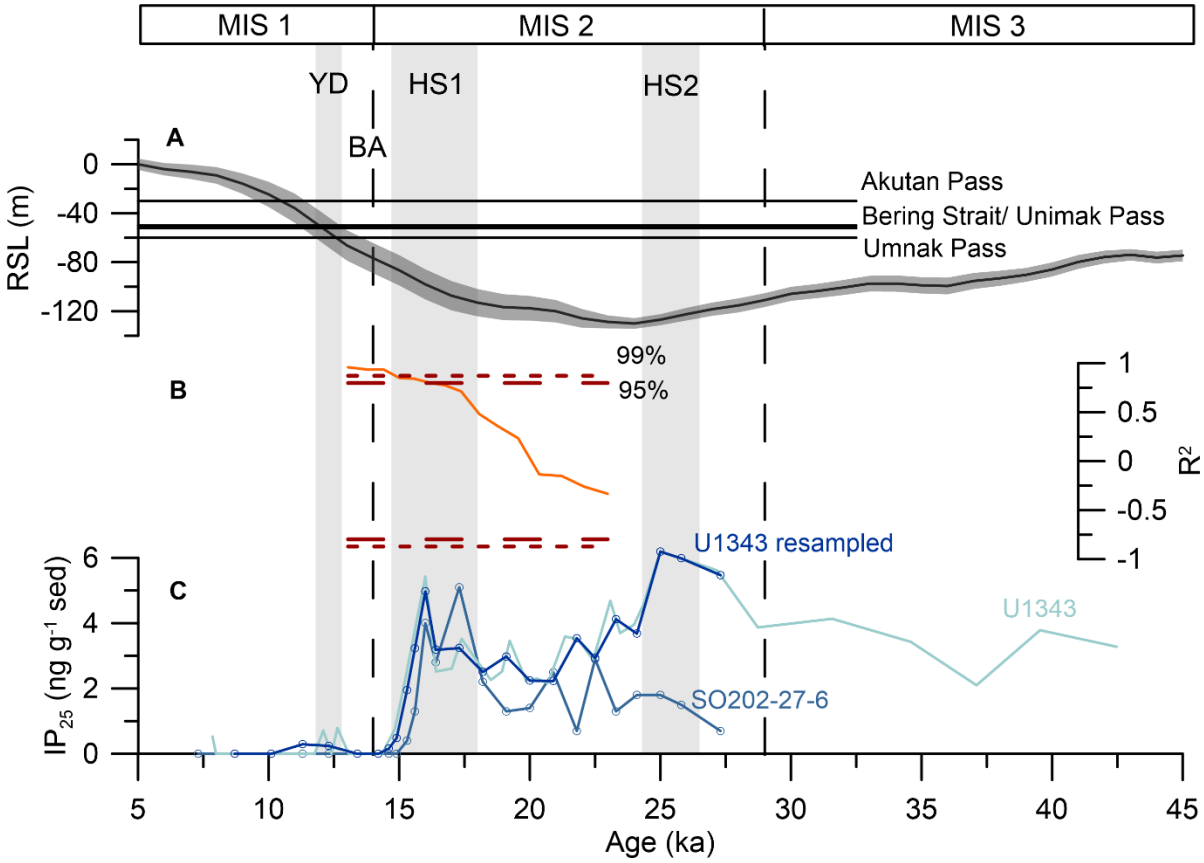

Supplementary Figure 7. (**A**) Relative sea level stack including a 2σ error envelope (Spratt and Lisiecki, 2016) and the depth of several eastern Aleutian Passes and the Bering Strait; (**B**) 10-pt moving window correlation of IP_{25} at SO202-27-6 and re-sampled IP_{25} at Site U1343 including the 95% (long red dashed line) and 99% (short red dashed line) confidence interval; (C) IP_{25} at SO202-27-6 (medium blue), Site U1343 (light blue) and re-sampled IP_{25} at Site U1343 (navy blue).

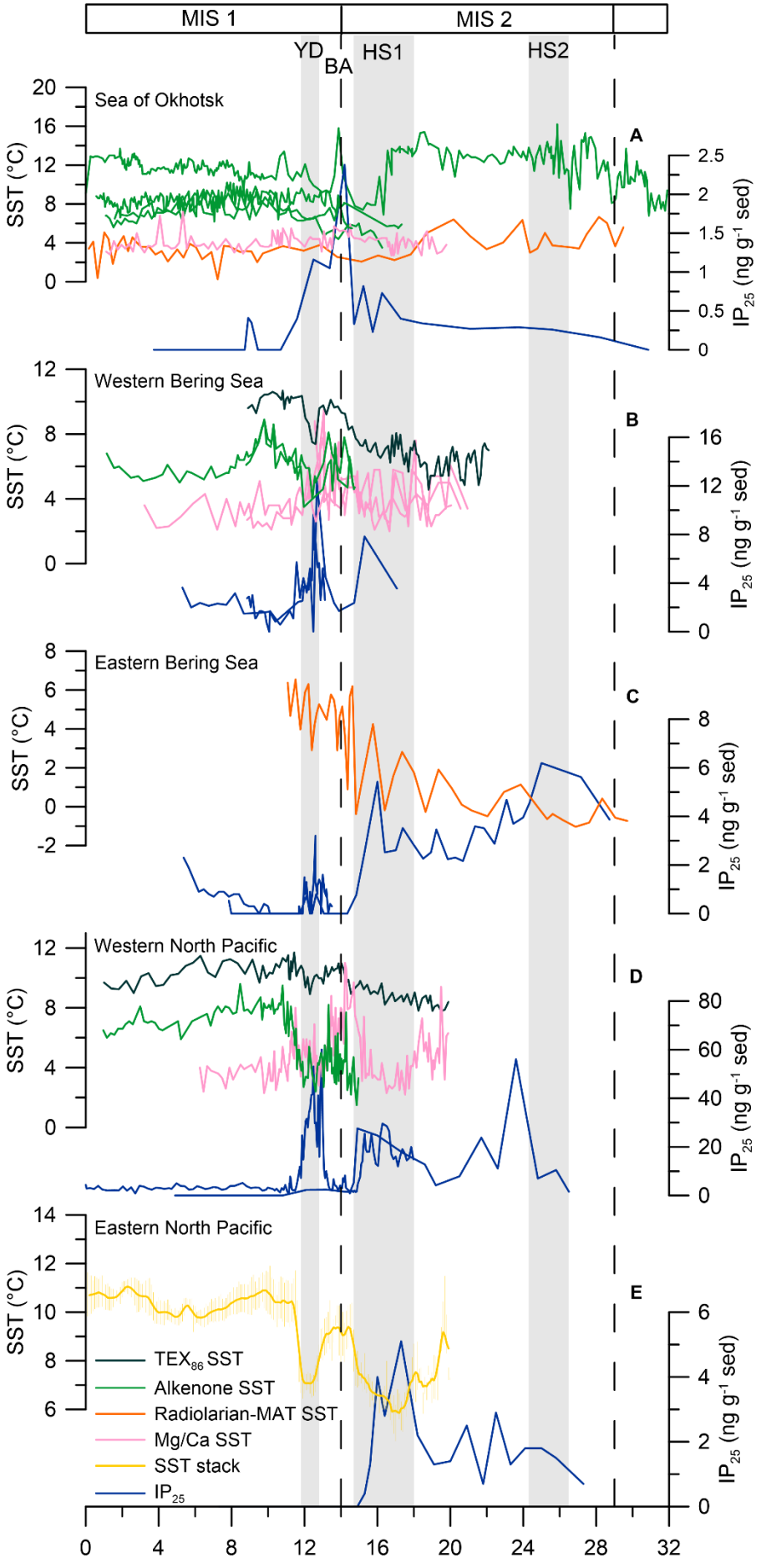

Supplementary Figure 8. Compilation of SST and IP_{25} records from the North Pacific. SST reconstructions are based on planktonic foraminiferal Mg/Ca (pink), TEX_{86} (dark green), alkenones (green), and radiolarian modern analogue technique (MAT) (orange). (**A**) SST records (Harada et al., 2006, 2004; Hernández-Almeida et al., 2020; Max et al., 2012; Riethdorf et al., 2013) and IP_{25} (Lo et al., 2018) from the Sea of Okhotsk; (**B**) SST records (Max et al., 2012; Meyer et al., 2016; Riethdorf et al., 2013) and IP_{25} (Méheust et al., 2016) from the western Bering Sea; (**C**) SST records (Hernández-Almeida et al., 2020) and IP_{25} (this study, Méheust et al., 2018) from the eastern Bering Sea; (**D**) SST records (Max et al., 2012; Meyer et al., 2016; Riethdorf et al., 2013) and IP_{25} (Méheust et al., 2018) from the western North Pacific; (**E**) SST stack including the standard error of the mean (Praetorius et al., 2020) and IP_{25} (Méheust et al., 2018) from the eastern North Pacific.

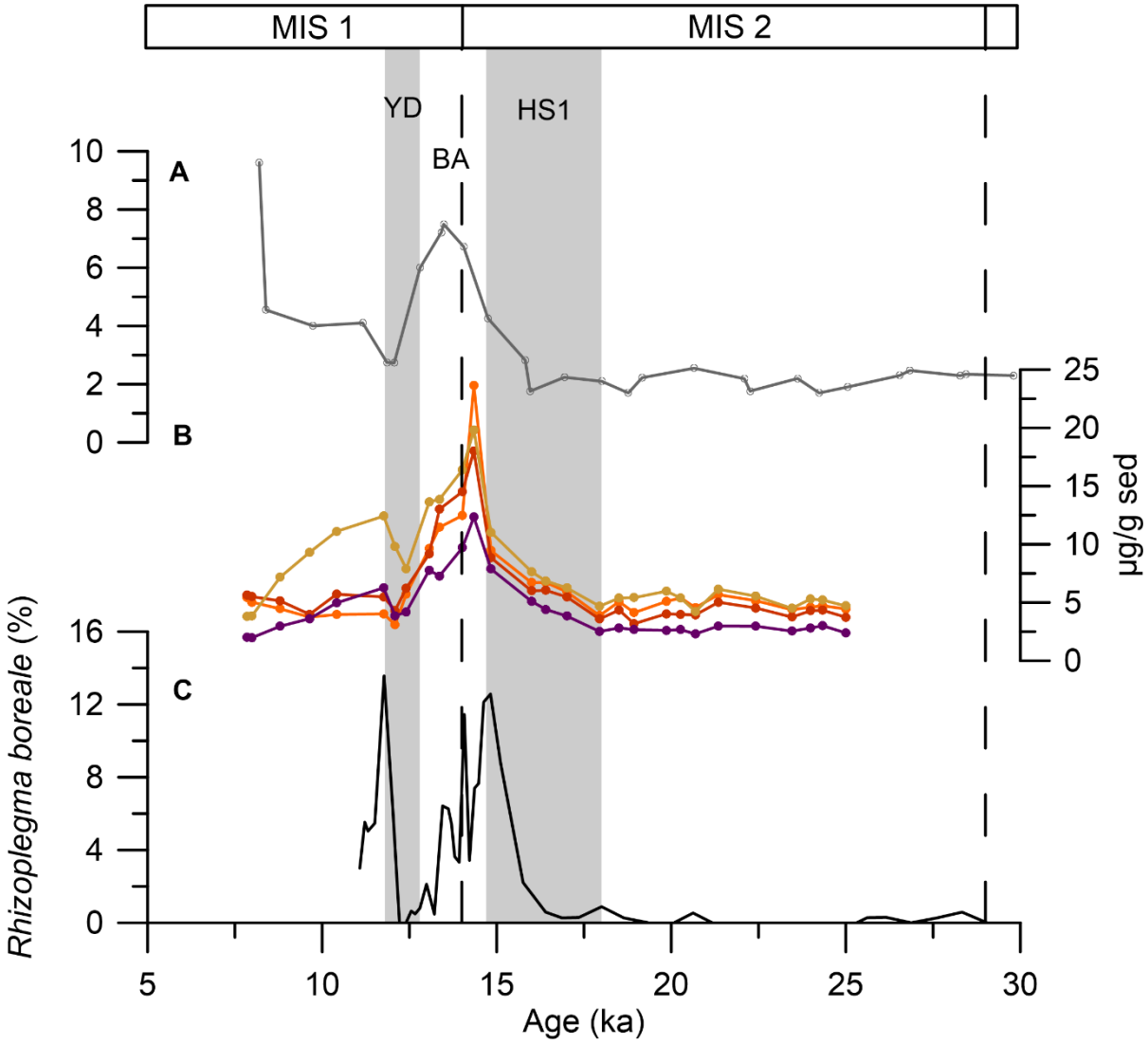

Supplementary Figure 9. (**A**) MARopal at Site U1343 (Kim et al., 2014); (**B**) Concentrations of brassicasterol (orange), cholesterol (red), campesterol (purple), and β-sitosterol (yellow) at Site U1343; (**C**) Relative concentration of the radiolarian species *Rhizoplegma boreale* at site PC-23A in the northern Bering Sea, indicative of meltwater runoff (Itaki et al., 2012).

Supplementary Table 1. Synthesis of sea ice, SST, oceanic circulation, ventilation, primary productivity, atmospheric temperature and atmospheric circulation dynamics in the Bering Sea and the North Pacific during the LGM, HS1, the BA, the YD, and the early Holocene.

Climate Parameter	Region		Early Holocene (~8-11.8 ka)	YD (11.8-12.8 ka)	BA (12.8-14.7 ka)	HS1 (14.7-18 ka)	LGM (19-26.5 ka)	References
Sea ice	Bering Sea	Western	Ice free to marginal sea-ice conditions	Marginal to extended seasonal sea-ice cover, sharp decline in sea-ice extent at the YD/Holocene boundary	Ice free to marginal sea-ice conditions during the early BA, followed by an increase in sea-ice extent prior to the BA/YD boundary	Extended seasonal sea-ice cover, decline of the sea-ice cover from 15 ka onward	No records	Caissie et al., 2010; Itaki et al., 2012; Méheust et al., 2018, 2016, this study
		Eastern				Extended seasonal sea-ice cover during early HS1, followed by a transition to MIZ conditions (16.5 ka) and a northward retreat of the sea-ice margin from 16 ka	Intermediate seasonal sea-ice cover	
	Subarctic North Pacific	Western	Ice free conditions	Reduced to extended seasonal sea-ice cover	Ice free conditions	Marginal to extended sea-ice cover, decline of the sea-ice cover from 15 ka	Reduced to marginal seasonal sea-ice cover	
		Eastern		Ice free conditions	Ice free to reduced seasonal sea-ice conditions	Marginal to extended sea-ice cover, decline of the sea-ice cover from 16 ka	Extended seasonal sea-ice cover	

Sea surface (SST) and subsurface temperatures	Bering Sea	Western	Reconstruction based on alkenones and TEX_{86} suggest early Holocene SST warming, planktonic foraminiferal Mg/Ca suggests subsurface cooling	Planktonic foraminiferal Mg/Ca suggest relatively constant subsurface temperatures with minimal cooling, alkenone and TEX_{86} records indicate SST cooling	Substantial region-wide SST warming recorded at the HS1/BA boundary, independent of the applied temperature proxy. SST and subsurface cooling into the YD interval.	Planktonic foraminiferal Mg/Ca suggest constant subsurface temperatures with minimal cooling, TEX_{86} indicates transient SST cooling during early HS1 followed by warming	Planktonic foraminiferal Mg/Ca suggest relatively mild LGM subsurface temperatures, TEX_{86} records indicate substantial SST warming since the LGM and warming summer SSTs from ~19 ka	Caissie et al., 2010; Gray et al., 2018; Hernández-Almeida et al., 2020; Meyer et al., 2016; Praetorius et al., 2020 and references therein; Riethdorf et al., 2013; Harada et al., 2012; Kiefer and Kienast, 2005; Kienast and McKay, 2001; Sarnthein et al., 2006
		Eastern	No records	Relatively constant SSTs based on radiolarian assemblages with potential early YD cooling and warming at the YD/Holocene boundary		Radiolarian assemblages suggest variable SSTs with overall warming trend	Radiolarian assemblages suggest colder LGM SSTs compared to the early Holocene, early deglacial warming spikes in SST from ~20 ka	
	Subarctic North Pacific	Western	Reconstruction based on alkenones and TEX_{86} suggest early Holocene SST warming, planktonic foraminiferal Mg/Ca suggests subsurface cooling	Planktonic foraminiferal Mg/Ca suggest early YD subsurface cooling, TEX86 and alkenone records indicate SST cooling		Planktonic foraminiferal Mg/Ca indicate cooling subsurface temperatures, while TEX_{86} SSTs remain stable	TEX_{86}, alkenone SSTs, and planktonic foraminiferal Mg/Ca suggest relatively mild LGM SST and subsurface temperatures	
		Eastern	SST stack indicates rapid warming until ~11 ka, followed by relatively stable Holocene SSTs	SST stack suggests substantial cooling		SST stack suggests cooling during early HS1, followed by warming from ~16.5 ka	Planktonic foraminiferal Mg/Ca suggest relatively mild LGM subsurface temperatures	

Oceanic Surface circulation	Bering Sea	Western	Complete flooding of the Bering Sea shelf and Bering Strait, enhanced Alaskan Stream inflow into the Bering Sea, strengthening of the Bering Sea surface circulation	Marine transgression, onset of flooding of eastern Aleutian passes and Bering Sea shelf	Reduced inflow of Alaskan Stream waters through eastern Aleutian Passes, closed Bering Strait	Reduced inflow of Alaskan Stream waters through eastern Aleutian Passes and a closed Bering Strait. The strength of the Bering Slope Current (BSC) depends on the Alaskan Stream inflow to the Bering Sea, thus the BSC was likely weaker. A weaker BSC would also result in less eddy upwelling activity along the eastern slope.		Caissie et al., 2010; Jakobsson et al., 2017; Mann and Hamilton, 1995; Meyer et al., 2016; Pico et al., 2020; Tanaka and Takahashi, 2005; Pelto et al., 2018
		Eastern						
	Subarctic North Pacific	Western	Modern subpolar gyre (SPG) boundaries, reduced influence of the Alaskan Stream in the western subarctic Pacific	Northward migration of the western SPG boundary from 12.5 ka	Less zonal SPG extending further south in the west	Northward migration of the eastern SPG boundary from 16.5 ka	Wind-driven strengthening and southward expansion of the SPG, enhanced Alaskan Stream influence in the west	Gray et al., 2020; Meyer et al., 2016; Riethdorf et al., 2013
		Eastern						
Primary productivity, nutrients, and pCO_2	Bering Sea	Western	Increased primary productivity and enhanced input of terrestrial organic carbon (eastern Bering Sea) during the Preboreal (10.7-11.7 ka), followed by reduction in productivity	Renewed decrease in primary productivity, albeit of lower extent compared to the LGM	High primary and export productivity and enhanced input of terrestrial organic carbon	Initial deglacial weakening of nutrient utilization from 17.5 ka, increase in primary productivity from ~16 ka	Overall low primary productivity and enhanced nutrient utilization	Brunelle et al., 2010, 2007; Caissie et al., 2010; Cook et al., 2005; Crusius et al., 2004; Gebhardt et al., 2008; Gorbarenko et al., 2005; Gray et al., 2018; Kim et al., 2014; Kohfeld and Chase, 2011; Lam et al., 2013; Max et al., 2012; Okazaki et al., 2005; Pelto et al., 2018; Riethdorf et al., 2016
		Eastern						
	Subarctic North Pacific	Western	Increased primary productivity compared to the LGM, but reduced compared to the BA		High primary and export productivity, rapid increase in surface ocean pCO_2 and CO_2 outgassing	Early HS1 increase in surface ocean pCO_2, initial decrease in nutrient utilization, increase in primary productivity from ~16-15 ka		
		Eastern						

Ventilation, (G)NPIW formation, and OMZ dynamics	Bering Sea	Western	Expansion and strengthening of the mid-depth OMZ and preservation of laminated sediments during the Preboreal period (10.7-11.7 ka) followed by a decrease in mid-depth hypoxia and cessation of laminated sediments	Improved ventilation to depth of at least ~1500 m	Break-down of GNPIW formation, expansion and strengthening of the mid-depth OMZ and preservation of laminated sediments due to enhanced respiration of organic carbon	Improved ventilation to depth of at least 2000 m during early HS1 and to 1000 m during remaining HS1	Improved ventilation to depth of 1000 m	Ahagon, 2003; Aiello and Ravelo, 2012; Cannariato and Kennett, 1999; Chikamoto et al., 2012; Cook et al., 2016, 2005; Cook and Keigwin, 2015; Crusius et al., 2004; Duplessy et al., 1989; Expedition 323 Scientists, 2010; Gong et al., 2019; Gorbarenko et al., 2010; Gray et al., 2018; Ikehara et al., 2006; Jaccard and Galbraith, 2013; Jang et al., 2017; Keigwin, 1998; Knudson and Ravelo, 2015; Kuehn et al., 2014; Matsumoto et al., 2002; Max et al., 2014; Menviel et al., 2012; Ohkouchi et al., 1994; Ohkushi et al., 2013; Okazaki et al., 2012, 2010; Okumura et al., 2009; Ovsepyan et al., 2017; Pelto et al., 2018; Praetorius et al., 2015; Rae et al., 2014; Rella et al., 2012; Saenko et al., 2004; Sagawa and Ikehara, 2008; Schlung et al., 2013; Shibahara et al., 2007; Tetard et al., 2017; Worne et al., 2019; Wu et al., 2008; Zheng et al., 2000; Zou et al., 2020
		Eastern						
	Subarctic North Pacific	Western	Decrease in the ventilation of the mid-depth North Pacific	Improved ventilation to depth of ~1500 m	Break-down of GNPIW formation and improved ventilation of NPDW, enhanced upwelling of nutrient-, CO_2-rich NPDW, widespread mid-depth hypoxia and preservation of laminated sediments	Enhanced GNPIW formation and improved ventilation to depth of 2000 m	GNPIW formation and improved ventilation to depth of 2000 m, reduced oxygenation of NPDW	
		Eastern		Potentially enhanced overturning but of lower extent compared to HS1		Enhanced GNPIW formation and improved ventilation to depth of 3600 m		

Atmospheric temperatures	Bering Sea	Western	Northern hemisphere-wide warming	Northern hemisphere cooling during the early YD, followed by consistent warming into the early Holocene	Enhanced rate of northern hemisphere warming, peak BA northern hemisphere warmth at ~13.5 ka followed by cooling into the YD interval	Early HS1 cooling in Beringia and the northern hemisphere, overall warming during the second half of HS1	Northern hemisphere temperatures were colder by 3-3.5 °C during the LGM compared to the early Holocene	Buizert et al., 2014; Kurek et al., 2009; Rasmussen et al., 2006; Shakun et al., 2012; Svensson et al., 2008; Viau et al., 2008; Vinther et al., 2006
		Eastern						
	Subarctic North Pacific	Western						
		Eastern						
Atmospheric circulation	Bering Sea	Western	Establishment of modern positions of polar easterlies and mid-latitude westerlies	Northward shift of the westerlies in the western North Pacific from 12.5 ka	Less zonal jet stream, weakened atmospheric circulation compared to HS1, but enhanced compared to the Holocene due to the remnant Laurentide Ice Sheet	Strengthened Aleutian Low bringing cold air masses to the western Bering Sea and western North Pacific, northward migration of the westerlies in the eastern North Pacific from 16.5 ka	Southward shift of the mid-latitude westerlies and polar easterlies, enhanced wind stress curl over the subarctic North Pacific	Gong et al., 2019; Gray et al., 2020, 2018; Nagashima et al., 2007; Yanase and Abe-Ouchi, 2007
		Eastern						
	Subarctic North Pacific	Western						
		Eastern						

Supplementary References

Ahagon, N., Ohkushi, K., Uchida, M., Mishima, T., 2003. Mid-depth circulation in the northwest Pacific during the last deglaciation: Evidence from foraminiferal radiocarbon ages. Geophys. Res. Lett. 30, 2097. https://doi.org/10.1029/2003GL018287

Aiello, I.W., Ravelo, A.C., 2012. Evolution of marine sedimentation in the Bering Sea since the Pliocene. Geosphere 8, 1231–1253. https://doi.org/10.1130/GES00710.1

Asahi, H., Kender, S., Ikehara, M., Sakamoto, T., Takahashi, K., Ravelo, A.C., Alvarez Zarikian, C.A., Khim, B.K., Leng, M.J., 2016. Orbital-scale benthic foraminiferal oxygen isotope stratigraphy at the northern Bering Sea Slope Site U1343 (IODP Expedition 323) and its Pleistocene paleoceanographic significance. Deep Sea Res. Part II Top. Stud. Oceanogr. 125–126, 66–83. https://doi.org/10.1016/J.DSR2.2014.01.004

Brunelle, B.G., Sigman, D.M., Cook, M.S., Keigwin, L.D., Haug, G.H., Plessen, B., Schettler, G., Jaccard, S.L., 2007. Evidence from diatom-bound nitrogen isotopes for subarctic Pacific stratification during the last ice age and a link to North Pacific denitrification changes. Paleoceanography 22, n/a-n/a. https://doi.org/10.1029/2005PA001205

Brunelle, B.G., Sigman, D.M., Jaccard, S.L., Keigwin, L.D., Plessen, B., Schettler, G., Cook, M.S., Haug, G.H., 2010. Glacial/interglacial changes in nutrient supply and stratification in the western subarctic North Pacific since the penultimate glacial maximum. Quat. Sci. Rev. 29, 2579–2590. https://doi.org/10.1016/J.QUASCIREV.2010.03.010

Buizert, C., Gkinis, V., Severinghaus, J.P., He, F., Lecavalier, B.S., Kindler, P., Leuenberger, M., Carlson, A.E., Vinther, B., Masson-Delmotte, V., White, J.W.C., Liu, Z., Otto-Bliesner, B., Brook, E.J., 2014. Greenland temperature response to climate forcing during the last deglaciation. Science (80-.). 345, 1177–1180. https://doi.org/10.1126/science.1254961

Caissie, B.E., Brigham-Grette, J., Lawrence, K.T., Herbert, T.D., Cook, M.S., 2010. Last Glacial Maximum to Holocene sea surface conditions at Umnak Plateau, Bering Sea, as inferred from diatom, alkenone, and stable isotope records. Paleoceanography 25. https://doi.org/10.1029/2008PA001671

Cannariato, K.G., Kennett, J.P., 1999. Climatically related millennial-scale fluctuations in strength of California margin oxygen-minimum zone during the past 60 k.y., Geology. GeoScienceWorld. https://doi.org/10.1130/0091-7613(1999)027<0975:CRMSFI>2.3.CO;2

Chikamoto, M.O., Menviel, L., Abe-Ouchi, A., Ohgaito, R., Timmermann, A., Okazaki, Y., Oka, A., Mouchet, A., 2012. Variability in North Pacific intermediate and deep water ventilation during Heinrich events in two coupled climate models. Deep Sea Res. Part II Top. Stud. Oceanogr. 61–64, 114–126. https://doi.org/10.1016/J.DSR2.2011.12.002

Cook, M.S., Keigwin, L.D., 2015. Radiocarbon profiles of the NW Pacific from the LGM and deglaciation: Evaluating ventilation metrics and the effect of uncertain surface reservoir ages. Paleoceanography 30, 174–195. https://doi.org/10.1002/2014PA002649

Cook, M.S., Keigwin, L.D., Sancetta, C.A., 2005. The deglacial history of surface and intermediate water of the Bering Sea. Deep Sea Res. Part II Top. Stud. Oceanogr. 52, 2163–2173. https://doi.org/10.1016/J.DSR2.2005.07.004

Cook, M.S., Ravelo, A.C., Mix, A., Nesbitt, I.M., Miller, N. V., 2016. Tracing subarctic Pacific water masses with benthic foraminiferal stable isotopes during the LGM and late Pleistocene. Deep Sea Res. Part II Top. Stud. Oceanogr. 125–126, 84–95. https://doi.org/10.1016/J.DSR2.2016.02.006

Crusius, J., Pedersen, T.F., Kienast, S., Keigwin, L., Labeyrie, L., 2004. Influence of northwest Pacific productivity on North Pacific Intermediate Water oxygen concentrations during the Bølling-Ållerød interval (14.7-12.9 ka). Geology 32, 633–636. https://doi.org/10.1130/G20508.1

Duplessy, J.-C., Arnold, M., Bard, E., Juillet-Leclerc, A., Kallel, N., Labeyrie, L., 1989. AMS 14C Study of Transient Events and of the Ventilation Rate of the Pacific Intermediate Water During the Last Deglaciation. Radiocarbon 31, 493–502.

Expedition 323 Scientists, 2010. Bering Sea pealeoceanography: Pliocene-Pleistocene paleoceanography and climate history of the Bering Sea. IODP Prelim. Rep. 323. https://doi.org/10.2204/iodp.pr.323.2010

Gebhardt, H., Sarnthein, M., Grootes, P.M., Kiefer, T., Kuehn, H., Schmieder, F., Röhl, U., 2008. Paleonutrient and productivity records from the subarctic North Pacific for Pleistocene glacial terminations I to V. Paleoceanography 23, n/a-n/a. https://doi.org/10.1029/2007PA001513

Gong, X., Lembke-Jene, L., Lohmann, G., Knorr, G., Tiedemann, R., Zou, J.J., Shi, X.F., 2019. Enhanced North Pacific deep-ocean stratification by stronger intermediate water formation during Heinrich Stadial 1. Nat. Commun. 10, 656. https://doi.org/10.1038/s41467-019-08606-2

Gorbarenko, S.A., Basov, I.A., Chekhovskaya, M.P., Southon, J., Khusid, T.A., Artemova, A. V., 2005. Orbital and millennium scale environmental changes in the southern Bering Sea during the last glacial-Holocene: Geochemical and paleontological evidence. Deep. Res. Part II Top. Stud. Oceanogr. 52, 2174–2185. https://doi.org/10.1016/j.dsr2.2005.08.005

Gorbarenko, S.A., Wang, P., Wang, R., Cheng, X., 2010. Orbital and suborbital environmental changes in the southern Bering Sea during the last 50 kyr. Palaeogeogr. Palaeoclimatol. Palaeoecol. 286, 97–106. https://doi.org/10.1016/j.palaeo.2009.12.014

Gray, W.R., Rae, J.W.B., Wills, R.C.J., Shevenell, A.E., Taylor, B., Burke, A., Foster, G.L., Lear, C.H., 2018. Deglacial upwelling, productivity and CO2 outgassing in the North Pacific Ocean. Nat. Geosci. 11, 340–344. https://doi.org/10.1038/s41561-018-0108-6

Gray, W.R., Wills, R.C.J., Rae, J.W.B., Burke, A., Ivanovic, R.F., Roberts, W.H.G., Ferreira, D., Valdes, P.J., 2020. Wind-Driven Evolution of the North Pacific Subpolar Gyre Over the Last Deglaciation. Geophys. Res. Lett. 47. https://doi.org/10.1029/2019GL086328

Harada, N., Ahagon, N., Sakamoto, T., Uchida, M., Ikehara, M., Shibata, Y., 2006. Rapid fluctuation of alkenone temperature in the southwestern Okhotsk Sea during the past 120 ky. Glob. Planet. Change 53, 29–46. https://doi.org/10.1016/j.gloplacha.2006.01.010

Harada, N., Ahagon, N., Uchida, M., Murayama, M., 2004. Northward and southward migrations of frontal zones during the past 40 kyr in the Kuroshio-Oyashio transition area. Geochemistry, Geophys. Geosystems 5, n/a-n/a. https://doi.org/10.1029/2004GC000740

Harada, N., Sato, M., Seki, O., Timmermann, A., Moossen, H., Bendle, J., Nakamura, Y., Kimoto, K., Okazaki, Y., Nagashima, K., Gorbarenko, S.A., Ijiri, A., Nakatsuka, T., Menviel, L., Chikamoto, M.O., Abe-Ouchi, A., Schouten, S., 2012. Sea surface temperature changes in the Okhotsk Sea and adjacent North Pacific during the last glacial maximum and deglaciation. Deep. Res. Part II Top. Stud. Oceanogr. 61–64, 93–105. https://doi.org/10.1016/j.dsr2.2011.12.007

Hernández-Almeida, I., Boltovskoy, D., Kruglikova, S.B., Cortese, G., 2020. A new radiolarian transfer function for the Pacific Ocean and application to fossil records: Assessing potential and limitations for the last glacial-interglacial cycle. Glob. Planet. Change 190, 103186. https://doi.org/10.1016/j.gloplacha.2020.103186

Ikehara, K., Ohkushi, K., Shibahara, A., Hoshiba, M., 2006. Change of bottom water conditions at intermediate depths of the Oyashio region, NW Pacific over the past 20,000 yrs. Glob. Planet. Change 53, 78–91. https://doi.org/10.1016/j.gloplacha.2006.01.011

Itaki, T., Kim, S., Rella, S.F., Uchida, M., Tada, R., Khim, B.K., 2012. Millennial-scale variations of late Pleistocene radiolarian assemblages in the Bering Sea related to environments in shallow and deep waters. Deep. Res. Part II Top. Stud. Oceanogr. 61–64, 127–144. https://doi.org/10.1016/j.dsr2.2011.03.002

Jaccard, S.L., Galbraith, E.D., 2013. Direct ventilation of the North Pacific did not reach the deep ocean during the last deglaciation. Geophys. Res. Lett. 40, 199–203. https://doi.org/10.1029/2012GL054118

Jakobsson, M., Pearce, C., Cronin, T.M., Backman, J., Anderson, L.G., Barrientos, N., Björk, G., Coxall, H., de Boer, A., Mayer, L.A., Mörth, C.-M., Nilsson, J., Rattray, J.E., Stranne, C., Semiletov, I., O'Regan, M., 2017. Post-glacial flooding of the Bering Land Bridge dated to 11 cal ka BP based on new geophysical and sediment records. Clim. Past 13, 991–1005. https://doi.org/10.5194/cp-13-991-2017

Jang, K., Huh, Y., Han, Y., 2017. Authigenic Nd isotope record of North Pacific Intermediate Water formation and boundary exchange on the Bering Slope. Quat. Sci. Rev. 156, 150–163. https://doi.org/10.1016/j.quascirev.2016.11.032

Keigwin, L.D., 1998. Glacial-age hydrography of the far northwest Pacific Ocean. Paleoceanography 13, 323–339. https://doi.org/10.1029/98PA00874

Kiefer, T., Kienast, M., 2005. Patterns of deglacial warming in the Pacific Ocean: a review with emphasis on the time interval of Heinrich event 1. Quat. Sci. Rev. 24, 1063–1081. https://doi.org/10.1016/J.QUASCIREV.2004.02.021

Kienast, S.S., McKay, J.L., 2001. Sea surface temperatures in the subarctic northeast Pacific reflect millennial-scale climate oscillations during the last 16 kyrs. Geophys. Res. Lett. 28, 1563–1566. https://doi.org/10.1029/2000GL012543

Kim, S., Takahashi, K., Khim, B.-K., Kanematsu, Y., Asahi, H., Ravelo, A.C., 2014. Biogenic opal production changes during the Mid-Pleistocene Transition in the Bering Sea (IODP Expedition 323 Site U1343). Quat. Res. 81, 151–157. https://doi.org/10.1016/J.YQRES.2013.10.001

Knudson, K.P., Ravelo, A.C., 2015. North Pacific Intermediate Water circulation enhanced by the closure of the Bering Strait. Paleoceanography 30, 1287–1304. https://doi.org/10.1002/2015PA002840

Kohfeld, K.E., Chase, Z., 2011. Controls on deglacial changes in biogenic fluxes in the North Pacific Ocean. Quat. Sci. Rev. 30, 3350–3363. https://doi.org/10.1016/J.QUASCIREV.2011.08.007

Kuehn, H., Lembke-Jene, L., Gersonde, R., Esper, O., Lamy, F., Arz, H., Kuhn, G., Tiedemann, R., 2014. Laminated sediments in the Bering Sea reveal atmospheric teleconnections to Greenland climate on millennial to decadal timescales during the last deglaciation. Clim. Past 10, 2215–2236. https://doi.org/10.5194/cp-10-2215-2014

Kurek, J., Cwynar, L.C., Ager, T.A., Abbott, M.B., Edwards, M.E., 2009. Late Quaternary paleoclimate of western Alaska inferred from fossil chironomids and its relation to vegetation histories. Quat. Sci. Rev. 28, 799–811. https://doi.org/10.1016/j.quascirev.2008.12.001

Lam, P.J., Robinson, L.F., Blusztajn, J., Li, C., Cook, M.S., McManus, J.F., Keigwin, L.D., 2013. Transient stratification as the cause of the North Pacific productivity spike during deglaciation. Nat. Geosci. 6, 622–626. https://doi.org/10.1038/ngeo1873

Lisiecki, L.E., Raymo, M.E., 2005. A Pliocene-Pleistocene stack of 57 globally distributed benthic δ^{18}O records. Paleoceanography 20, n/a-n/a. https://doi.org/10.1029/2004PA001071

Lo, L., Belt, S.T., Lattaud, J., Friedrich, T., Zeeden, C., Schouten, S., Smik, L., Timmermann, A., Cabedo-Sanz, P., Huang, J.-J., Zhou, L., Ou, T.-H., Chang, Y.-P., Wang, L.-C., Chou, Y.-M., Shen, C.-C., Chen, M.-T., Wei, K.-Y., Song, S.-R., Fang, T.-H., Gorbarenko, S.A., Wang, W.-L., Lee, T.-Q., Elderfield, H., Hodell, D.A., 2018. Precession and atmospheric CO2 modulated variability of sea ice in the central Okhotsk Sea since 130,000 years ago. Earth Planet. Sci. Lett. 488, 36–45. https://doi.org/10.1016/J.EPSL.2018.02.005

Mann, D.H., Hamilton, T.D., 1995. Late Pleistocene and Holocene paleoenvironments of the North Pacific coast. Quat. Sci. Rev. 14, 449–471. https://doi.org/10.1016/0277-3791(95)00016-I

Matsumoto, K., Oba, T., Lynch-Stieglitz, J., Yamamoto, H., 2002. Interior hydrography and circulation of the glacial Pacific Ocean. Quat. Sci. Rev. 21, 1693–1704. https://doi.org/10.1016/S0277-3791(01)00142-1

Max, L., Lembke-Jene, L., Riethdorf, J.-R., Tiedemann, R., Nürnberg, D., Kühn, H., Mackensen, A., 2014. Pulses of enhanced North Pacific Intermediate Water ventilation from the Okhotsk Sea and Bering Sea during the last deglaciation. Clim. Past 10, 591–605. https://doi.org/10.5194/cp-10-591-2014

Max, L., Riethdorf, J.-R., Tiedemann, R., Smirnova, M., Lembke-Jene, L., Fahl, K., Nürnberg, D., Matul, A., Mollenhauer, G., 2012. Sea surface temperature variability and sea-ice extent in the subarctic northwest Pacific during the past 15,000 years. Paleoceanography 27, n/a-n/a. https://doi.org/10.1029/2012PA002292

Méheust, M., Stein, R., Fahl, K., Gersonde, R., 2018. Sea-ice variability in the subarctic North Pacific and adjacent Bering Sea during the past 25 ka: new insights from IP25 and Uk′37 proxy records. arktos 4, 8. https://doi.org/10.1007/s41063-018-0043-1

Méheust, M., Stein, R., Fahl, K., Max, L., Riethdorf, J.-R., 2016. High-resolution IP25-based reconstruction of sea-ice variability in the western North Pacific and Bering Sea during the past 18,000 years. Geo-Marine Lett. 36, 101–111. https://doi.org/10.1007/s00367-

015-0432-4

Menviel, L., Timmermann, A., Elison Timm, O., Mouchet, A., Abe-Ouchi, A., Chikamoto, M.O., Harada, N., Ohgaito, R., Okazaki, Y., 2012. Removing the North Pacific halocline: Effects on global climate, ocean circulation and the carbon cycle. Deep. Res. Part II Top. Stud. Oceanogr. 61–64, 106–113. https://doi.org/10.1016/j.dsr2.2011.03.005

Meyer, V.D., Max, L., Hefter, J., Tiedemann, R., Mollenhauer, G., 2016. Glacial-to-Holocene evolution of sea surface temperature and surface circulation in the subarctic northwest Pacific and the Western Bering Sea. Paleoceanography 31, 916–927. https://doi.org/10.1002/2015PA002877

Nagashima, K., Tada, R., Matsui, H., Irino, T., Tani, A., Toyoda, S., 2007. Orbital- and millennial-scale variations in Asian dust transport path to the Japan Sea. Palaeogeogr. Palaeoclimatol. Palaeoecol. 247, 144–161. https://doi.org/10.1016/j.palaeo.2006.11.027

Ohkouchi, N., Kawahata, H., Murayama, M., Okada, M., Nakamura, T., Taira, A., 1994. Was deep water formed in the North Pacific during the Late Quaternary? Cadmium evidence from the Northwest Pacific. Earth Planet. Sci. Lett. 124, 185–194. https://doi.org/10.1016/0012-821X(94)00082-4

Ohkushi, K., Kennett, J.P., Zeleski, C.M., Moffitt, S.E., Hill, T.M., Robert, C., Beaufort, L., Behl, R.J., 2013. Quantified intermediate water oxygenation history of the NE Pacific: A new benthic foraminiferal record from Santa Barbara basin. Paleoceanography 28, 453–467. https://doi.org/10.1002/palo.20043

Okazaki, Y., Sagawa, T., Asahi, H., Horikawa, K., Onodera, J., 2012. Ventilation changes in the western North Pacific since the last glacial period. Clim. Past 8, 17–24. https://doi.org/10.5194/cp-8-17-2012

Okazaki, Y., Takahashi, K., Asahi, H., Katsuki, K., Hori, J., Yasuda, H., Sagawa, Y., Tokuyama, H., 2005. Productivity changes in the Bering Sea during the late Quaternary. Deep Sea Res. Part II Top. Stud. Oceanogr. 52, 2150–2162. https://doi.org/10.1016/J.DSR2.2005.07.003

Okazaki, Y., Timmermann, A., Menviel, L., Harada, N., Abe-Ouchi, A., Chikamoto, M.O., Mouchet, A., Asahi, H., 2010. Deepwater formation in the North Pacific during the Last Glacial Termination. Science 329, 200–4. https://doi.org/10.1126/science.1190612

Okumura, Y.M., Deser, C., Hu, A., Timmermann, A., Xie, S.-P., Okumura, Y.M., Deser, C., Hu, A., Timmermann, A., Xie, S.-P., 2009. North Pacific Climate Response to Freshwater Forcing in the Subarctic North Atlantic: Oceanic and Atmospheric Pathways. J. Clim. 22, 1424–1445. https://doi.org/10.1175/2008JCLI2511.1

Ovsepyan, E.A., Ivanova, E.V., Lembke-Jene, L., Max, L., Tiedemann, R., Nürnberg, D., 2017. Penultimate and last glacial oceanographic variations in the Bering Sea on millennial timescales: Links to North Atlantic climate. Quat. Sci. Rev. 163, 135–151. https://doi.org/10.1016/J.QUASCIREV.2017.03.012

Pelto, B.M., Caissie, B.E., Petsch, S.T., Brigham-Grette, J., 2018. Oceanographic and Climatic Change in the Bering Sea, Last Glacial Maximum to Holocene. Paleoceanogr. Paleoclimatology 33, 93–111. https://doi.org/10.1002/2017PA003265

Pico, T., Mitrovica, J.X., Mix, A.C., 2020. Sea level fingerprinting of the Bering Strait flooding history detects the source of the Younger Dryas climate event. Sci. Adv. 6,

eaay2935. https://doi.org/10.1126/sciadv.aay2935

Praetorius, S.K., Condron, A., Mix, A.C., Walczak, M.H., McKay, J.L., Du, J., 2020. The role of Northeast Pacific meltwater events in deglacial climate change. Sci. Adv. 6, eaay2915. https://doi.org/10.1126/sciadv.aay2915

Praetorius, S.K., Mix, A.C., Walczak, M.H., Wolhowe, M.D., Addison, J.A., Prahl, F.G., 2015. North Pacific deglacial hypoxic events linked to abrupt ocean warming. Nature 527, 362–366. https://doi.org/10.1038/nature15753

Rae, J.W.B., Sarnthein, M., Foster, G.L., Ridgwell, A., Grootes, P.M., Elliott, T., 2014. Deep water formation in the North Pacific and deglacial CO2 rise. Paleoceanography 29, 645–667. https://doi.org/10.1002/2013PA002570

Rasmussen, S.O., Andersen, K.K., Svensson, A.M., Steffensen, J.P., Vinther, B.M., Clausen, H.B., Siggaard-Andersen, M.-L., Johnsen, S.J., Larsen, L.B., Dahl-Jensen, D., Bigler, M., Röthlisberger, R., Fischer, H., Goto-Azuma, K., Hansson, M.E., Ruth, U., 2006. A new Greenland ice core chronology for the last glacial termination. J. Geophys. Res. 111, D06102. https://doi.org/10.1029/2005JD006079

Rella, S.F., Tada, R., Nagashima, K., Ikehara, M., Itaki, T., Ohkushi, K., Sakamoto, T., Harada, N., Uchida, M., 2012. Abrupt changes of intermediate water properties on the northeastern slope of the Bering Sea during the last glacial and deglacial period. Paleoceanography 27, n/a-n/a. https://doi.org/10.1029/2011PA002205

Riethdorf, J.-R., Max, L., Nürnberg, D., Lembke-Jene, L., Tiedemann, R., 2013. Deglacial development of (sub) sea surface temperature and salinity in the subarctic northwest Pacific: Implications for upper-ocean stratification. Paleoceanography 28, 91–104. https://doi.org/10.1002/palo.20014

Riethdorf, J.-R., Thibodeau, B., Ikehara, M., Nürnberg, D., Max, L., Tiedemann, R., Yokoyama, Y., 2016. Surface nitrate utilization in the Bering sea since 180 kA BP: Insight from sedimentary nitrogen isotopes. Deep Sea Res. Part II Top. Stud. Oceanogr. 125–126, 163–176. https://doi.org/10.1016/J.DSR2.2015.03.007

Saenko, O.A., Schmittner, A., Weaver, A.J., Saenko, O.A., Schmittner, A., Weaver, A.J., 2004. The Atlantic–Pacific Seesaw. J. Clim. 17, 2033–2038. https://doi.org/10.1175/1520-0442(2004)017<2033:TAS>2.0.CO;2

Sagawa, T., Ikehara, K., 2008. Intermediate water ventilation change in the subarctic northwest Pacific during the last deglaciation. Geophys. Res. Lett. 35, L24702. https://doi.org/10.1029/2008GL035133

Sarnthein, M., Kiefer, T., Grootes, P.M., Elderfield, H., Erlenkeuser, H., 2006. Warmings in the far northwestern Pacific promoted pre-Clovis immigration to America during Heinrich event 1. Geology 34, 141. https://doi.org/10.1130/G22200.1

Schlung, S.A., Christina Ravelo, A., Aiello, I.W., Andreasen, D.H., Cook, M.S., Drake, M., Dyez, K.A., Guilderson, T.P., Lariviere, J.P., Stroynowski, Z., Takahashi, K., 2013. Millennial-scale climate change and intermediate water circulation in the Bering Sea from 90 ka: A high-resolution record from IODP Site U1340. Paleoceanography 28, 54–67. https://doi.org/10.1029/2012PA002365

Shakun, J.D., Clark, P.U., He, F., Marcott, S.A., Mix, A.C., Liu, Z., Otto-Bliesner, B., Schmittner, A., Bard, E., 2012. Global warming preceded by increasing carbon dioxide

concentrations during the last deglaciation. Nature 484, 49–54. https://doi.org/10.1038/nature10915

Shibahara, A., Ohkushi, K., Kennett, J.P., Ikehara, K., 2007. Late Quaternary changes in intermediate water oxygenation and oxygen minimum zone, northern Japan: A benthic foraminiferal perspective. Paleoceanography 22, n/a-n/a. https://doi.org/10.1029/2005PA001234

Spratt, R.M., Lisiecki, L.E., 2016. A Late Pleistocene sea level stack. Clim. Past 12, 1079–1092. https://doi.org/10.5194/cp-12-1079-2016

Svensson, A., Andersen, K.K., Bigler, M., Clausen, H.B., Dahl-Jensen, D., Davies, S.M., Johnsen, S.J., Muscheler, R., Parrenin, F., Rasmussen, S.O., Röthlisberger, R., Seierstad, I., Steffensen, J.P., Vinther, B.M., 2008. A 60 000 year Greenland stratigraphic ice core chronology. Clim. Past 4, 47–57. https://doi.org/10.5194/cp-4-47-2008

Tanaka, S., Takahashi, K., 2005. Late Quaternary paleoceanographic changes in the Bering Sea and the western subarctic Pacific based on radiolarian assemblages. Deep Sea Res. Part II Top. Stud. Oceanogr. 52, 2131–2149. https://doi.org/10.1016/J.DSR2.2005.07.002

Tetard, M., Licari, L., Beaufort, L., 2017. Oxygen history off Baja California over the last 80 kyr: A new foraminiferal-based record. Paleoceanography 32, 246–264. https://doi.org/10.1002/2016PA003034

Viau, A.E., Gajewski, K., Sawada, M.C., Bunbury, J., 2008. Low- and high-frequency climate variability in eastern Beringia during the past 25 000 years. Can. J. Earth Sci. 45, 1435–1453. https://doi.org/10.1139/E08-036

Vinther, B.M., Clausen, H.B., Johnsen, S.J., Rasmussen, S.O., Andersen, K.K., Buchardt, S.L., Dahl-Jensen, D., Seierstad, I.K., Siggaard-Andersen, M.-L., Steffensen, J.P., Svensson, A., Olsen, J., Heinemeier, J., 2006. A synchronized dating of three Greenland ice cores throughout the Holocene. J. Geophys. Res. 111, D13102. https://doi.org/10.1029/2005JD006921

Worne, S., Kender, S., Swann, G.E.A., Leng, M.J., Ravelo, A.C., 2019. Coupled climate and subarctic Pacific nutrient upwelling over the last 850,000 years. Earth Planet. Sci. Lett. 522, 87–97. https://doi.org/10.1016/j.epsl.2019.06.028

Wu, L., Li, C., Yang, C., Xie, S.P., 2008. Global teleconnections in response to a shutdown of the Atlantic meridional overturning circulation. J. Clim. 21, 3002–3019. https://doi.org/10.1175/2007JCLI1858.1

Yanase, W., Abe-Ouchi, A., 2007. The LGM surface climate and atmospheric circulation over East Asia and the North Pacific in the PMIP2 coupled model simulations. Clim. Past 3, 439–451. https://doi.org/10.5194/cp-3-439-2007

Zheng, Y., van Geen, A., Anderson, R.F., Gardner, J. V., Dean, W.E., 2000. Intensification of the Northeast Pacific oxygen minimum zone during the Bölling-Alleröd Warm Period. Paleoceanography 15, 528–536. https://doi.org/10.1029/1999PA000473

Zou, J., Shi, X., Zhu, A., Kandasamy, S., Gong, X., Lembke-Jene, L., Chen, M.-T., Wu, Y., Ge, S., Liu, Y., Xue, X., Lohmann, G., Tiedemann, R., 2020. Millennial-scale variations in sedimentary oxygenation in the western subtropical North Pacific and its links to North Atlantic climate. Clim. Past 16, 387–407. https://doi.org/10.5194/cp-16-387-2020